PIV flow measurements for heat transfer characterization in upscaled AM surface roughness.

Ambrosio Pedreño Marin

TUDelft

PIV flow measurements for heat transfer characterization in upscaled AM surface roughness.

by

Ambrosio Pedreño Marin

to obtain the degree of Master of Science

at the Delft University of Technology,

to be defended publicly on Thursday November 7, 2024 at 9:00 AM.

An electronic version of this thesis is available at `http://repository.tudelft.nl/`.

TUDelft

Summary

This thesis investigates the impact of additive manufacturing induced surface roughness on the heat transfer mechanisms within gas turbine cooling channels. The study involves the design and utilization of a Particle Image Velocimetry (PIV) experimental rig. The research focuses on understanding how the AM roughness affects the flow behavior and heat transfer in micro-channels. Results demonstrate that flow stagnation points significantly contribute to the heat transfer enhancement. High turbulence regions, especially following large roughness elements show an increased heat transfer. Secondary flow features were identified close to the wall, like high-speed streaks. However, the findings show the necessity to further develop the PIV system for closer wall measurements to capture localized effects due to the roughness.

Contents

List of Figures

List of Tables

Nomenclature

Abbreviations

Abbreviation	Definition
AM	Additive Manufacturing
BL	Boundary Layer
CAD	Computer Aided Design
CC	Cross-Correlation
CCS	Cross-Correlation Strength
CFD	Computer Fluid Dynamics
DB	Dittus-Boelter Equation
DMLS	Direct Metal Laser Sintering
DNS	Direct Numerical Simulation
FOV	Field of View
FPS	Frames Per Second
FFT	Fast Fourier Transform
HT	Heat Transfer
ISO	International Organization for Standardization
L-PBF	Laser Powder Bed Fusion
LES	Large Eddie Simulation
RANS	Reynolds Averaged Navier-Stokes
SEM	Scanning Electron Microscope
SR	Surface Roughness
SRHT	Surface Roughness Heat Transfer
TIT	Turbine Inlet Temperature

Symbols

Symbol	Definition	Unit
a_{air}	Velocity of sound	$[\text{m s}^{-1}]$
c_p	Specific heat capacity at constant pressure	$[\text{m}^2\,\text{s}^{-2}\,\text{K}^{-1}]$
$c_{p_{air}}$	Air specific heat capacity at constant pressure	$[\text{m}^2\,\text{s}^{-2}\,\text{K}^{-1}]$
D	Diameter	$[\text{mm}]$
D_h	Hydraulic Diameter	$[\text{mm}]$
d_p	Particle Diameter	$[\text{m}]$
d_{diff}	Particle Diameter due to diffraction	$[\text{m}]$
d_{eff}	Effective Particle Diameter	$[\text{m}]$
DVR	Dynamic Velocity Range	$[\text{-}]$
DSR	Dynamic Spatial Range	$[\text{-}]$
Ec	Eckert Number	$[\text{-}]$
ES	Effective Slope	$[°]$
f_D	Darcy Friction Factor	$[\text{-}]$
$f_{\#}$	f-stop	$[\text{-}]$
h	Heat transfer coefficient	$[\text{kg m}^{-1}\,\text{s}^{-3}\,\text{K}^{-1}]$
k_{air}	Thermal Conductivity of Air	$[\text{kg m}^{-1}\,\text{s}^{-1}\,\text{K}^{-1}]$
k_s	Equivalent Sand Grain Diameter	$[\text{mm}]$
L	Characteristic Length	$[\text{mm}]$

Symbol	Definition	Unit
L_h	Hydrodynamic Entrance Length	[mm]
M	Magnification	[-]
Nu	Nusselt Number	[-]
Nu_0	Maximum Nusselt Number	[-]
Nu_{DB}	Nusselt Number for Smooth Surface (Dittus-Boelter)	[-]
p	Absolute Pressure	[kg m s^{-2}]
Pr	Prandtl Number	[-]
PPR	Primary Peak Ratio	[-]
$\dot{q}$	Heat flux	[kg m^{-2} s^{-1} K^{-1}]
R_a	Arithmetic Mean Deviation	[μ m]
R_q	Root-Mean-Square Roughness	[μ m]
R_p	Maximum Peak Height	[μ m]
R_v	Maximum Valley Depth	[μ m]
R_z	Maximum Peak to Valley Height	[μ m]
R_{sk}	Skewness	[-]
R_{ku}	Kurtosis	[-]
Re	Reynolds Number	[-]
SNR	Signal to Noise Ratio	[-]
T	Temperature	[K]
T_w	Wall Temperature	[K]
$T_{f,\infty}$	Fluid Temperature	[K]
$\Delta T_{w,f}$	Temperature difference between fluid and solid	[K]
TKE	Turbulent Kinetic Energy	[m^2 s^{-2}]
TI	Turbulence Intensity	[%]
U	Velocity Magnitude	[m s^{-1}]
U_0	Average maximum velocity measured	[m s^{-1}]
u	Stream-wise velocity component	[m s^{-1}]
u_τ	Wall friction velocity	[m s^{-1}]
u_m	Bulk flow velocity	[m s^{-1}]
v	Wall normal velocity component	[m s^{-1}]
w	Specific work done	[m^2 s^{-2}]
x	Stream-wise direction	[-]
y	Wall normal direction	[-]
z	Span-wise direction	[-]
δ	Channel Half-height	[mm]
δ_{99}	Boundary Layer Thickness	[mm]
Δ_{pmax}	Maximum particle displacement	[m]
κ	Von Karman Constant	[-]
μ	Dynamic Viscosity	[kg m^{-1} s^{-1}]
μ_{air}	Air Dynamic Viscosity	[kg m^{-1} s^{-1}]
ϕ	Example Variable	[-]
ρ	Density	[kg m^{-3}]
ρ_p	Particle Density	[kg m^{-3}]
σ	Standard Deviation of a Statistical Distribution	[-]
τ_p	Particle Response Time	[s]
τ_t	Total Wall Shear Stress	[kg m s^{-2}]
τ_w	Wall Shear Stress	[kg m s^{-2}]
$\|\phi\|$	Variable Magnitude	[-]
$<\phi>$	Time averaged	[-]
$<\phi>_{x,y,z}$	Spatial average	[-]
$\overline{\phi}$	Reynolds Averaged	[-]
ϕ^+	Non-dimensionalisation using u_τ	[-]
ϕ'	Fluctuating component of variable	[-]

<div align="right">

1

</div>

<div align="right">

Introduction

</div>

This chapter acts as an introduction to the present thesis, starting with the motivation for this project. Subsequently, the main goals and research questions are presented. Finally, the outline of the thesis is described.

1.1. Motivation

Climate change is one of the mayor issues that humanity is facing nowadays. Energy consumption is steadily rising every year and given that most of the world's energy production comes from non-renewable means like coal, greenhouse gases emissions also increase. As can be seen in Fig. 1.1, even though much effort is being placed into promoting and developing renewable energy sources, fossil fuels still hold the biggest stake in global energy production. This opens up a big opportunity for companies that are able to implement new renewable production methods or that can increase the efficiency of current systems.
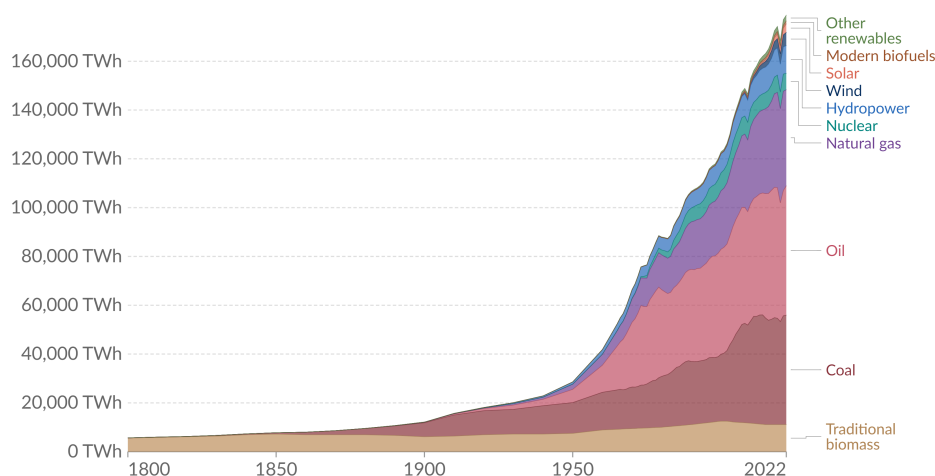
Figure 1.1: Global primary energy consumption by source. [1]

Gas turbines play a big role in the energy generation industry. They are the main workhorse in gas-steam plants as well as in combined heat and power-plants. Their widespread use is due to the numerous advantages they have with respect to other production means. First, they can use a wide range of fuels, while maintaining a clean combustion process. Furthermore, they are compact, reliable and do not require high manpower for their continuous operation [2]. Consequently, their place in the near future is assured. Thus, Siemens Energy AB is dedicated to improve their turbines, enhancing their efficiency while implementing alternative renewable fuels.

The ideal cycle offers the highest fuel efficiency and lowest emissions, however, it is not achievable in practice. Nonetheless, improvements can be made so as to approach the limit. One strategy is to increase the Turbine Inlet Temperature (TIT), which increases both the net power output and the energy efficiency [3]. In fact, current gas turbines can reach an operating TIT that far exceeds the melting point of the blade materials, necessitating the use of a cooling system [4].

Traditional manufacturing methods only allowed for simple cooling channels as those in Fig. 1.2a. However, with the use of Additive Manufacturing (AM) in the production of some static components from the turbine section, like the stator vanes, more complex cooling channels and internal geometries can be implemented [5]. This is because the component is manufactured by joining together very thin layers of material on top of each other, like in L-PBF. An example of these channels can be observed in Fig. 1.2b. These complex cooling channels can significantly cool down the blade, which will allow for a higher TIT and thus higher efficiency.
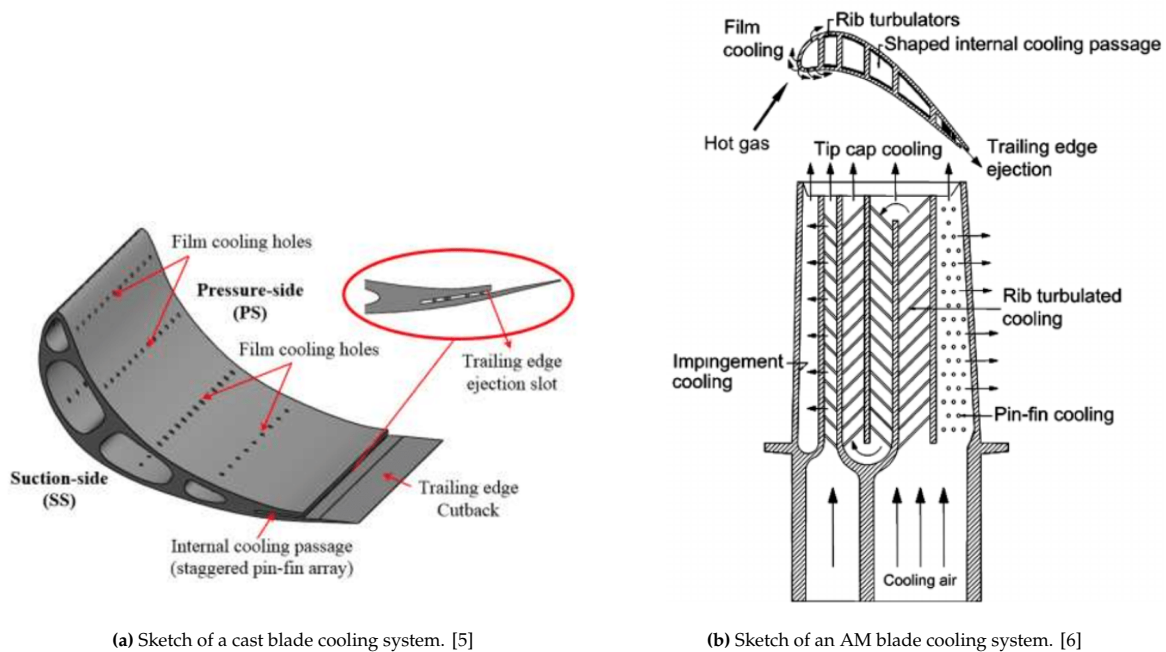
(a) Sketch of a cast blade cooling system. [5] **(b)** Sketch of an AM blade cooling system. [6]

Figure 1.2: Comparison of traditional cast blade cooling system vs AM.

Although this technology brings a lot of benefits, the AM of metal components via L-PBF generates an inherently highly rough surface finish [7]. This does not present a problem for easily accessible external surfaces that can be machined; however, it is a problem for the small internal cooling channels that can not be post-processed [8]. On one hand, the surface roughness (SR) will have a big influence on the boundary layer development inside the channel that could be detrimental to the flow behavior, but on the other hand this could be beneficial to the heat transfer properties [9]. Numerous experimental and CFD studies have been made in this field, but the turbulent structure of the flow is still not fully understood [9].

1.2. Objective and research question.

The flow dynamic study, presented in this report, will focus on understanding the heat transfer enhancement mechanisms that dominate such a rough surface as those from AM micro-channels. Therefore, the main research objective of this work is to bring new knowledge on the heat transfer mechanisms. For this purpose we will try to answer the following questions:

- *How does the surface roughness produced by AM affect the overall flow behaviour and mean flow properties in the channel?*
- *How does this altered flow behaviour enhance the heat transfer in the channel, how are they correlated?*

- *What are the main characteristic flow mechanism or structures that have a major influence on the heat transfer?*

For this research, the installation and development of a new functioning PIV experimental rig at the Siemens Energy Flow Lab in Finspaang was necessary, being this also one of the main objectives of the project. Therefore, the first goals of this project are:

- *Design and set-up an operating PIV rig, establishing the fundamental testing methodology of the rig.*
- *Design and set-up the wind-tunnel test section to replicate that of the Surface Roughness Heat Transfer (SRHT) rig.*

1.2.1. Type and context of research

The research carried out is practice related, more specifically it is practice-led. This is because the objective of the research is to gain knowledge about the practical mechanism that are behind a certain component's behavior. A creative outcome, like new component design, is not the objective of this project. [10].

This research project has been conducted for the Aerodynamics and Wind Energy Thesis (course code AE5122) so as to obtain the master's degree of Aerospace Engineering at the faculty of Aerospace Engineering of the Delft University of Technology, The Netherlands. The research has been carried out in Siemens Energy AB at their site in Finspång, Sweden.

$$2$$

Theoretical Background

This chapter gives an overview of the underlying physical concepts that are necessary to understand the work conducted in this thesis. Nonetheless, first it is necessary to understand the basic functioning of gas turbines and the State-Of-Art cooling in them so as to comprehend what are the advantages of using AM in them. Consequently, AM techniques will be explained, together with the Surface Roughness characterization method.

Next, we will delve into the fluid dynamics of wall bounded flows for both smooth and rough walls. Investigating what is the effect of high surface roughness on the heat transfer. Afterwards, some basic concepts of Particle Image Velocimetry are described to understand how the velocity field is measured. Finally, some basic notions on the CFD method used will be given.

2.1. Gas Turbines

As mentioned in Sec. 1.1, industrial gas turbines are a very attractive means of electricity production, delivering a very high power output. Even though these machines are very complex and require a lot of man-hours for their development, their structure and working principle is quite simple.

Turbines generate power by converting stored internal chemical energy from a fuel into mechanical energy via a combustion process. This is done by using a thermodynamic cycle. The best known examples are the Otto and Diesel cycle, which are employed inside of vehicle engines. These cycles are called alternative because they provide power at certain time intervals. However, the Gas Turbine is based of the Brayton cycle. This is an open cycle that produces power constantly. A comparison of both cycles on a Pressure vs Volume diagram can be observed in Fig. 2.1. Upon closer observation of these diagrams it can be observed that in the Brayton cycle combustion happens at a constant pressure while for the Otto it occurs at a constant volume.

These diagrams represent ideal cycles, there are no pressure losses and all adiabatic processes happen isentropically. Furthermore, it is assumed that the gas is ideal, so we can apply the equation of state, that the gas is calorically perfect, so it has a constant value of specific heat capacity at constant pressure and constant specific heat ratio, $c_p \neq f(T)$ & $\gamma \neq f(T)$. Moreover, it is assumed that the flow is homogeneous and frozen, so it's composition does not change in any stage.

The final objective is to find the work done, and thus the thermal efficiency of the cycle. To do this we would have to apply the first law of thermodynamics, energy conservation, to the complete cycle presented in Fig. 2.2. This results in Eq. 2.1, where the unit mass change in specific internal energy has to be zero as the cycle returns the system to it's original state.

$$\Delta u = q_A + w_{comp} - w_{turb} - q_R \tag{2.1}$$

Note that the energy extracted by the turbine can be divided into net energy and energy used to drive the compressor. This means that the net work done can be obtained by simply finding the difference

(a) Otto cycle. [11]
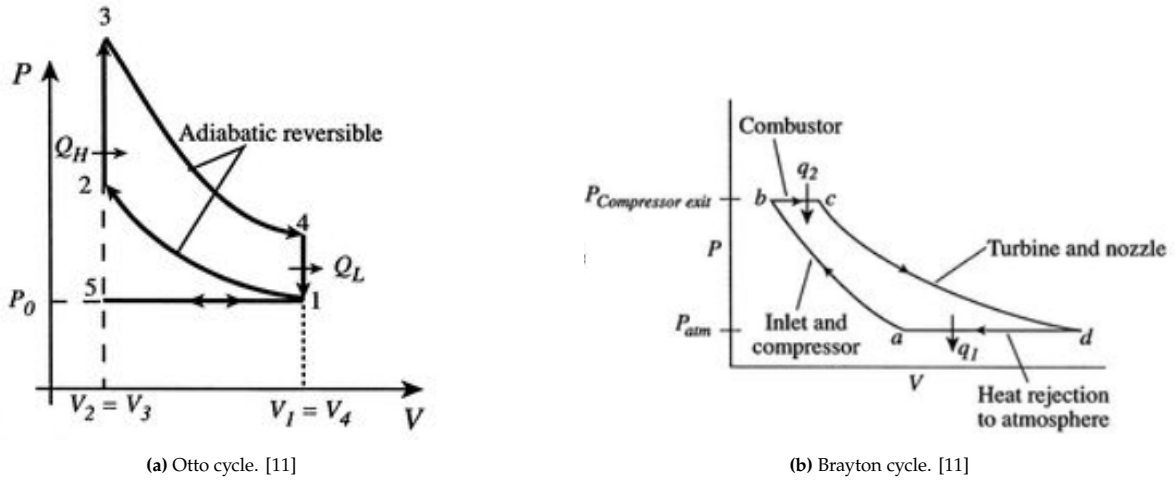
(b) Brayton cycle. [11]

Figure 2.1: P-V diagrams of alternative Otto and continuous Brayton cycle.

between the specific heat added and removed:

$$w_{turb} = w_{net} + w_{comp} = q_A + w_{comp} - q_R \tag{2.2}$$

$$w_{net} = q_A - q_R \tag{2.3}$$

To evaluate this equation we first need to understand each stage of the cycle. To accomplish this the cycle diagram in Fig. 2.2 can be followed and divided into 4 stages, finding the difference in enthalpy at each stage:

$0 \rightarrow 3$: This first stage takes place in the inlet and compressor. It corresponds to an adiabatic, quasi-static and isentropic compression.

$$w_{comp} = h_3 - h_0 = c_p(T_3 - T_0) \tag{2.4}$$

$3 \rightarrow 4$: This second stage takes place in the combustor. It corresponds to a constant pressure combustion, modeled as a constant pressure heat addition.

$$q_A = h_4 - h_3 = c_p(T_4 - T_3) \tag{2.5}$$

$4 \rightarrow 5$: This third stage takes place in the turbine stage and nozzle. It corresponds to an adiabatic, quasi-static and isentropic expansion. Here energy is extracted to drive the compressor and to produce power.

$$w_{turb} = h_5 - h_4 = c_p(T_5 - T_4) \tag{2.6}$$

$5 \rightarrow 6$: This last stage takes place in the atmosphere. It corresponds to heat removal at constant pressure, returning to the initial conditions.

$$q_R = h_0 - h_5 = c_p(T_0 - T_5) \tag{2.7}$$

With this analysis, the thermal efficiency of the cycle can be expressed as:

$$\eta = \frac{w_{net}}{w_{in}} = \frac{q_A - q_R}{q_A} = 1 - \frac{q_R}{q_A} = 1 - \frac{c_p(T_5 - T_0)}{c_p(T_4 - T_3)} = 1 - \frac{T_0(\frac{T_5}{T_0} - 1)}{T_3(\frac{T_4}{T_3} - 1)} \tag{2.8}$$
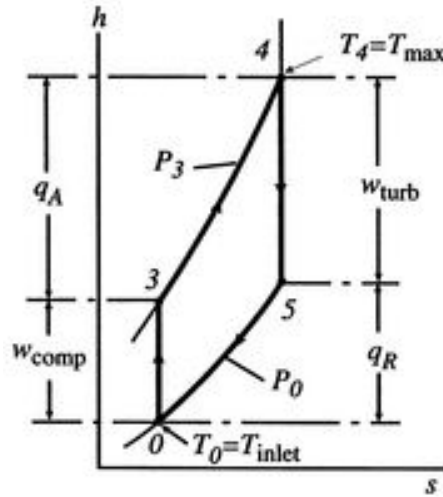
Figure 2.2: Enthalpy vs Temperature diagram of Brayton cycle. [11]

This equation can be further simplified by considering the fact that the compression relations of the compressor and turbine are the same and using the isentropic relations:

$$\frac{P_3}{P_0} = \frac{P_4}{P_5}$$

$$\pi_{30} = \frac{P_3}{P_0} = \left(\frac{T_3}{T_0}\right)^{\frac{\gamma}{\gamma-1}}$$

$$\pi_{54} = \frac{P_5}{P_4} = \left(\frac{T_5}{T_4}\right)^{\frac{\gamma}{\gamma-1}}$$

(2.9)

Combining these:

$$\frac{T_3}{T_0} = \frac{T_4}{T_5}$$

(2.10)

Therefore, Eq. 2.8 can be reduced to:

$$\eta = 1 - \frac{T_0}{T_3} = 1 - \left(\frac{1}{\pi_{30}}\right)^{\frac{\gamma-1}{\gamma}} = 1 - \frac{T_5}{T_4}$$

(2.11)

From this result it can be concluded that in order to increase the cycle efficiency we can do two things, increase the compressor ratio or the TIT. This last option is what concerns this thesis.

2.2. Turbine Cooling Methods

As demonstrated in the previous section, it is really important to achieve a TIT that is as high as possible. However, we are limited by the resistance of the turbine blades that immediately face this hot flow. Not only are these blades in a very hot environment, but they are also spinning at extreme velocities, so a blade that weighs only a few kilos could be facing centrifugal forces equivalent to a few tonnes of force. For example, a blade that weighs 1kg spinning at 16000 rpm with a rotor diameter of just 20cm would feel a force equivalent to almost 29000 kg. Furthermore, the wall temperature of the blade will not be uniform, at the stagnation points it will present the maximum temperatures. This means that the blade could have high temperature gradients that would place even more stresses on the component.

Therefore, in order to extend the component's life it is of vital importance to implement an effective blade cooling system.

In the first gas turbines, in the 50s, blades were not cooled and relied upon having a high max operating material temperature. At the time those machines could reach operating temperatures of 1000 - 1100 ºC. However, nowadays temperatures as high as 1600ºC can be reached. This is possible due to improvements in the materials being used, but primarily due to improvements in the cooling system, as can be observed in Fig. 2.3. The different cooling systems can be divided into internal and external and both will be explained in the following sections. The air used for cooling is typically extracted from the compressor stage and directed to the blades, rotor etc.
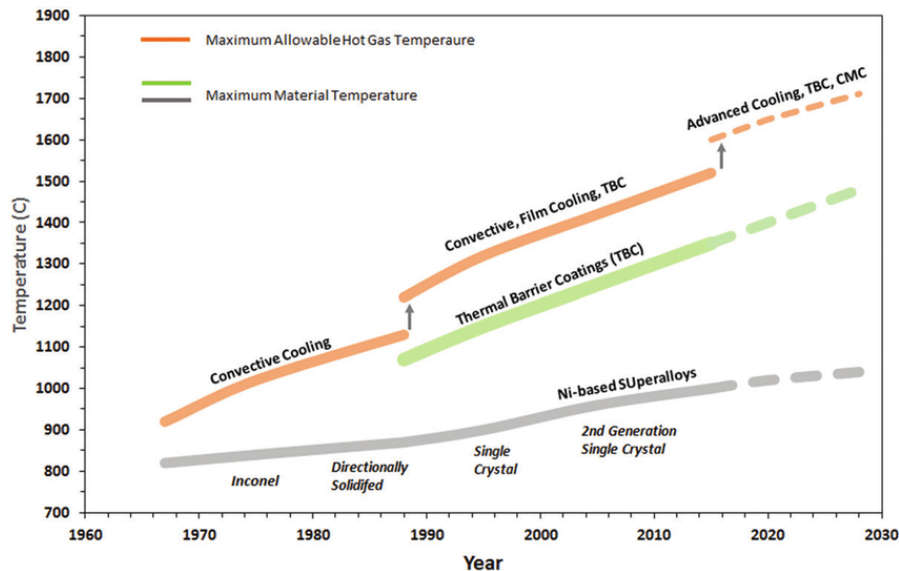
Figure 2.3: Evolution of gas turbine temperatures with cooling and materials improvements over time. [12]

2.2.1. Internal Cooling
In internal cooling methods, the air is circulated in the inside of the blade, cooling down the blade. These can be further divided into convection or impingement cooling.

Convection Cooling
This is the most commonly used method. Cooling air flows inside of the blade and heat is exchanged via convection. As can be observed in Fig. 1.2b, the inside of the turbine blade is equipped with several ribs and pins that increase the wetted area, turbulence and disrupt the boundary layer to increase heat exchange, by making it reattach with a lower thickness, which increases heat transfer as will be explained in Sec. 2.5.2. In the first blades that implemented this technology the air would just flow from the hub to the blade's tip, referred to as single pass cooling. However, nowadays the air flows through several serpentine passages as shown in Fig. 1.2b, this is called multi-pass. With the advent of AM these internal passages can be manufactured with more complex designs that could further increase the cooling of the system.

Impingement Cooling
Impingement cooling is an alternative method of cooling used at those spots where the temperatures reached are very high, for example the leading edge stagnation line. As can be observed in Fig. 1.2b, air is blown through some small holes, creating jets, these then impinge on the internal wall, highly increasing the heat exchange at these discrete locations. [13]. Generally the air then circulates around internal channels of the blade, cooling down other regions of the blade via convection.

2.2.2. External Cooling
External cooling methods are of crucial importance to extend the lifetime expectancy of the turbine hot section components. Generally it involves the creation of a thin cold air boundary layer that grants

thermal protection to the blade, casing, combustor liner, etc. [14] However, this comes at a price, air is extracted from the compressor stage and injected in the turbine stage, and this poses a penalty to the efficiency of the cycle. [14]

Film Cooling

As mentioned previously, this method relies upon the creation of a cold air protective layer that "insulates" the component form the hot air. This can be achieved in several ways, one is to implement a 2D slot. However, with this method it is complicated to obtain good mechanical properties. Therefore, discrete film cooling is preferred. Pressurized air is released through the holes, as shown in Fig. 2.4a, generating a complex jet-in-crossflow interaction that cools down the blade. This method can be extended to cover the whole blade, full blade film cooling, as shown in Fig. 2.4. The method described here is referred to as passive, however there exist active film cooling methods. The comprise pulsed jet film cooling or plasma actuators, however, these will not be further discussed here but for more information refer to [14].

(a) Turbine blade with leading edge holes for film cooling. [15]

(b) Turbine blade with holes for full blade film cooling.
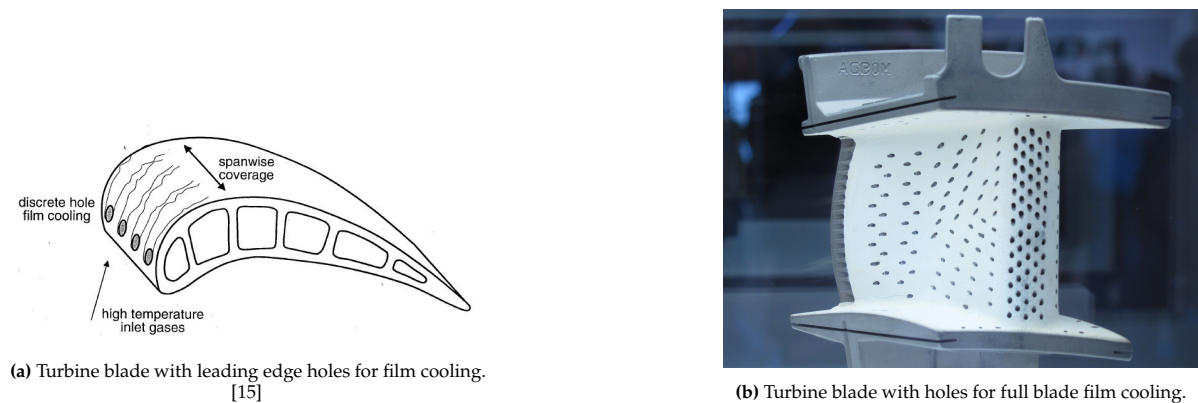
Figure 2.4: Discrete vs Full blade film cooling.

Transpiration Cooling

Transpiration cooling is a method in which the coolant flows through the micro-pores of a porous wall. This method relies upon two concepts. The first, as with film cooling, is creating a protective layer on the surface that decreases heat transfer from the mainflow to the wall. The second, is cooling through transpiration, heat exchange occurs between the solid structure and the coolant [16]. This method is very promising as it has been demonstrated that its cooling effectiveness is higher than that of film cooling, however, this technology has not been applied yet to a turbine [17].

Thermal Coating

Thermal barrier coating consists on the application of a protective layer of insulating material on the surface of the metal component to protect it from the mainflow hot gas. These materials present a very low thermal conductivity and sustain a large thermal gradient, being able to reduce the temperature by almost $100°$. The white surface of the blade presented in Fig. 2.4b corresponds to the thermal barrier.

2.3. Additive Manufacturing

AM is a technology that is having a huge impact on the way some components are produced. Not only is it being applied in the Aerospace sector, but other industries like medical and automotive are also implementing it. To get an idea on the interest that this method is gaining, we can look at the number of papers published yearly, Fig. 2.5. From this it is clear that this is a breakthrough technology and it looks like it's potential must still be unveiled.

Additive manufacturing, also referred to as rapid prototyping due to its origins as a method for quickly producing prototypes, is a fabrication process in which a component is created by adding layer upon layer of material. As previously mentioned, this is advantageous when compared to traditional manufacturing

Documents by year
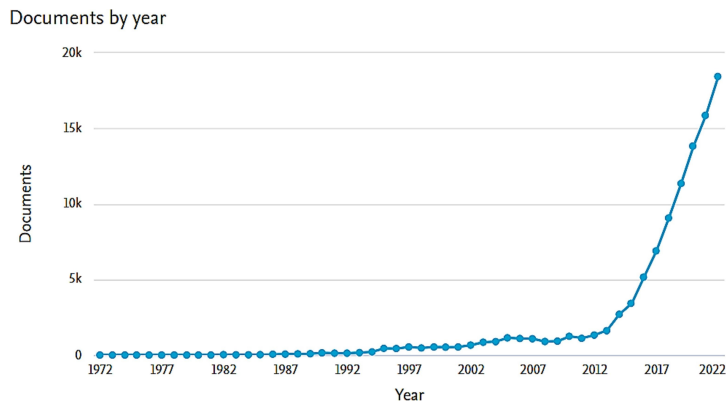
Figure 2.5: Publications by year on AM research. [18]

methods like casting or machining. It allows for the creation of complex geometries without added manufacturing complexity, increasing design options and almost eliminating manufacture feasibility studies. This is what makes it very attractive: previously impossible to produce designs can now be manufactured.

To understand further the scope of this thesis it is important to understand the underlying fundamentals behind AM. Even though there exist a wide variety of methods, these will not be examined here as it falls beyond the scope of this thesis. However, extensive information can be found in the literature [19] [18]. Nonetheless, L-PBF will be described due to its role in the fabrication of turbine blades and other components.

2.3.1. Laser Powder Bed Fusion (L-PBF)

In this method a fine layer of metal powder, ranging from $20\mu m$ to 1 mm, is applied on a substrate plate or an already processed layer. Subsequently, a high power laser beam is used to selectively melt and fuse together the metal along the desired contour. The build platform is then lowered, and a new layer of metal powder is applied. This process is repeated until the component is finished. The unfused powder can then be recycled and used in the next batch. A schematic of this process is presented in Fig. 2.6.
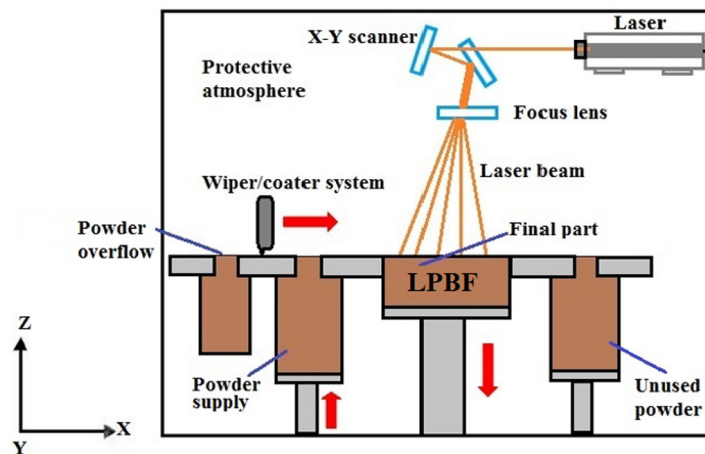
Figure 2.6: Schematic of how L-PBF process works. [20]

Even though the concept behind how this technique works might seem simple, it involves a lot of physical phenomena that complicate the process, with more than 150 parameter involved [20]. This makes it very hard to control the final quality of the component. Parameters like the material used, the print angle [21] [22] and layer thickness [23] have a big impact on the surface finish. This surface finish is of vital importance for the aim of this thesis, thus, in the next section, the surface roughness parameters employed to characterize it will be described.

2.3.2. Surface Roughness

AM components present a higher level of surface roughness than those produced using other manufacturing methods. On outer surfaces, this can be removed, however, for the micro-cooling channels in the turbine blades, as discussed in Sec. 2.2.1 it can not be removed, or the process is arduous.

In engineering the surface finish typically consists of some irregularities that can be random or uniformly distributed over a smooth surface [24]. The frequency of these irregularities will determine how they are classified. If their frequency is high then it is considered as roughness, when medium as waviness and the low frequencies as form, as illustrated in Fig. 2.7 [25] [9].
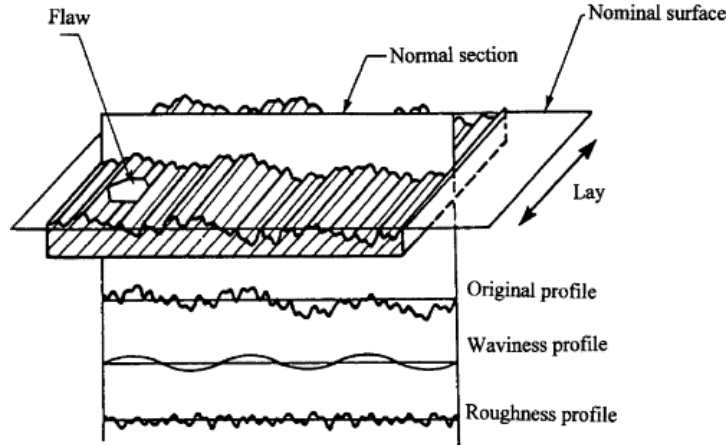
Figure 2.7: Difference between roughness, waviness and form. [25]

To characterize the surface roughness some international statistical standard parameters have been adopted, an example is ISO 1302 [9]. These can be measured along a sampling line, denoted as R parameters, or on a surface, S parameters [9]. Due to the nature of the measuring technique employed for this project we will stick to the R parameters. These are the ones used to create the upscaled rough surface plate, procedure which is presented in Sec. 3.2.3.

Surface Roughness R Parameters

The most important roughness parameters, as described in the ISO standard aforementioned, are grouped in Table 2.1. Note that they all correspond to line sampling, except for the Effective Slope ES, that is calculated from the roughness amplitude function k(x,z). This one is included here due to its importance for scaling the roughness function [26], however, it has not been used throughout this study.

Table 2.1: Roughness parameters definition.

Parameter	Description	Mathematical Description
R_a	Arithmetic Mean Deviation	$\frac{1}{l} \int |y| dx$
R_q	Root-mean-square roughness	$\sqrt{\frac{1}{l} \int |y| dx}$
R_p	Maximum peak height above the mean line, within a single sampling length.	$max[y(x)]$
R_v	Maximum valley depth below the mean line, within a single sampling length.	$|min[y(x)]|$
R_z	Maximum peak to valley height of the profile	$R_v + R_p$
R_{sk}	Skewness	$\frac{q}{(R_q^3)} \frac{1}{l} \int |y|^3 dx$
R_{ku}	Kurtosis	$\frac{q}{(R_q^4)} \frac{1}{l} \int y^4 dx$
ES	Effective Slope	$\frac{1}{l_x l_y} \int_0^l \int_0^{l_z} \left| \frac{\partial k(x,z)}{\partial x} \right| dx dy$

It is important to understand the physical meaning of each parameter. In fact, for example, the R_a

parameter by itself is not significant. This is because two surfaces may have the same R_a, while having different roughness profiles, with different values of R_p, R_{sk}, etc. Therefore, R_q is more physically significant [9].

Other parameters that can be misinterpreted are the skewness and kurtosis. The former gives an idea of the topological symmetry of the rough surface profile. As depicted in Fig. 2.8a, a value of 0 means that the distribution of valleys and peaks is a perfectly centered Gaussian. On the other hand, the kurtosis measures the sharpness of the roughness profile. While the skewness can be either positive or negative, the kurtosis must be positive. Again, a schematic depicting the physical meaning of this parameter is shown in Fig. 2.8b [9].

(a) Skewness schematic.

(b) Kurtosis schematic.
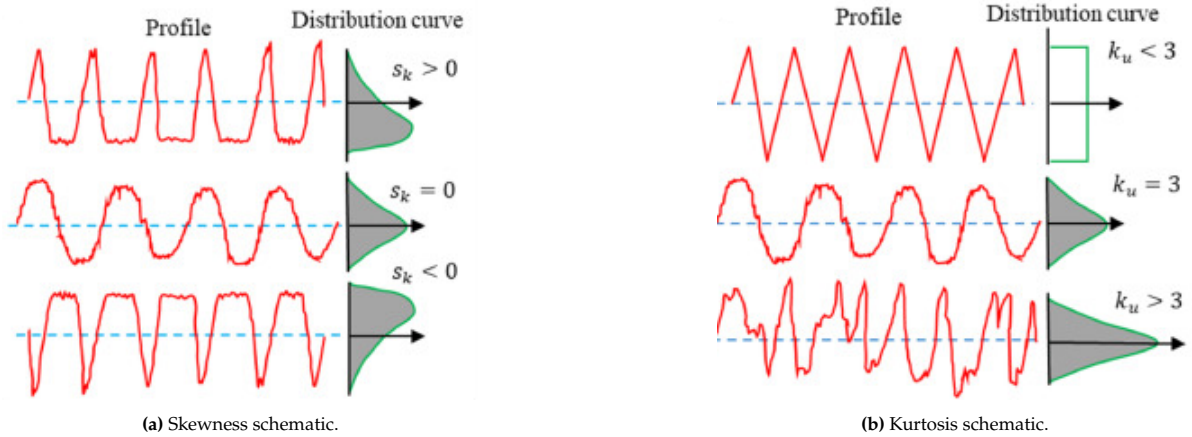
Figure 2.8: Different roughness profiles and amplitude distribution curve. [9]

AM vs "Traditional" Surface Roughness
Parts fabricated using AM will be subject to dimensional inaccuracies and high surface roughness. In fact, even the printing angle will have an important effect on the surface roughness. The properties of the upskin and downskin surfaces of the printed components will be different, the latter presenting an overall worse surface quality with more defects. The most notable is the adherence of partially molten residual powder particles to the surface, as shown in Fig. 2.9. These have a significant influence on the roundness of the cooling channel and on its final diameter, which can differ substantially from the desired one [27]. Furthermore, conventionally manufactured channels typically have a uniform surface roughness due to the fabrication processes employed, however, this might not be true for those produced using AM [28].

2.4. Wall bounded turbulent flows (Smooth)

This section explains some of the fundamental concepts of fluid dynamics on which this study is based, focusing specially on turbulent flows and heat transfer. Turbulence generated by shear can be divided into two types of flows: wall bounded and free turbulence, such as a jet flow. However, for the purpose of this study we will focus on the former.

We will consider only a purely smooth theoretical wall. First, the different flow regions will be characterized, and some universal scaling laws will be presented. Later, we will discuss the modes of heat transfer as well as the thermal boundary layer.

2.4.1. Flow Regions

First we will consider the fully-developed flow inside a smooth circular channel. Due to symmetry this can be reduced to a 2D flow between parallel walls, as schematized in Fig. 2.10. If we assume stationary and horizontally homogeneous flow, then for the velocity:

$$\frac{\partial}{\partial t} = 0; \qquad \frac{\partial}{\partial x} = \frac{\partial}{\partial z} = 0 \tag{2.12}$$
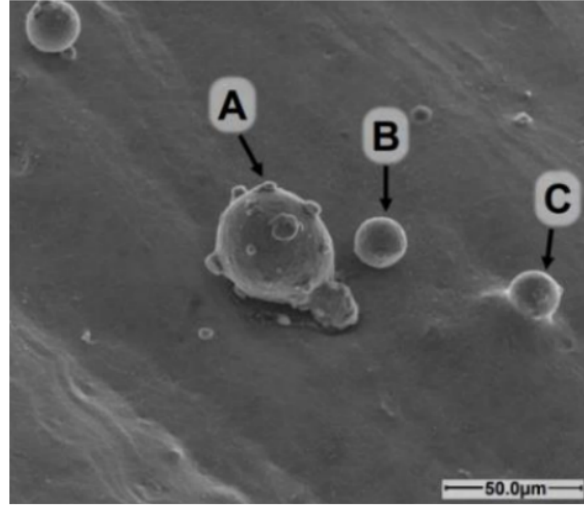
Figure 2.9: Microscope image of powder particles adhered to the surface. [29]

Thus, the Reynolds-averaged continuity and x-y momentum equations, as presented in Appendix A, can be reduced to:

$$\frac{\partial \overline{v}}{\partial y} = 0 \tag{2.13}$$

$$0 = -\frac{\partial \overline{p}}{\partial y} - \rho_0 \frac{\partial \tau_t}{\partial y} \tag{2.14}$$

$$0 = -\frac{\partial \overline{p}}{\partial y} - \rho_0 \frac{\partial \overline{u'^2}}{\partial y} \tag{2.15}$$

Where $\frac{\tau_t}{\rho_0} = -\overline{u'v'} + \nu \frac{\partial \overline{u}}{\partial y}$. If we integrate Eq. 2.13 and apply the boundary conditions, $\overline{v} = 0$ for y = 0, then $\overline{v} = 0$. Hence, the average velocity only has a component in the x-direction. Furthermore, Eq. 2.15 can be integrated to $\frac{\overline{p}}{\rho_0} = f(x) - \overline{v'^2}$, thus $\frac{\partial \overline{p}}{\partial x} \neq f(y)$. Therefore, the pressure can be expressed as:

$$\overline{p}(x, y) = \overline{p_0}(x) - \rho_0 \overline{v'^2}(y) \tag{2.16}$$

From this analysis it can be concluded that $\frac{\partial \overline{p}}{\partial x} = \frac{d\overline{p_0}}{dx}$.

It is interesting to now introduce the wall friction velocity and wall shear stress, as defined in Eq. 2.17, for subsequent analysis.

$$u_* = \sqrt{\frac{\tau_w}{\rho_0}} \tag{2.17}$$
$$\tau_w = \rho_0 u_*^2 = \tau_t(0)$$

By integrating Eq. 2.14 in the y-direction, and applying boundary conditions, a relation between u_* and the pressure gradient can be obtained:

$$u_*^2 = -\frac{H}{\rho_0} \frac{d\overline{p_0}}{dx} \tag{2.18}$$

Finally, substituting Eq. 2.18 into Eq. 2.14 and integrating we find that the total shear stress is a linear function of y:
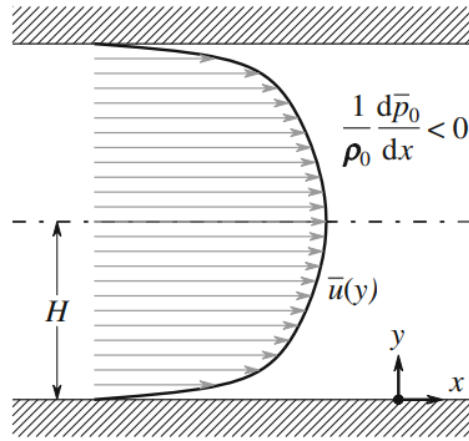
Figure 2.10: Schematic of a flow between parallel plates. [30]

$$\frac{\tau_t}{\rho_0} = u_*^2 \left(1 - \frac{y}{H}\right) \tag{2.19}$$

The solution obtained analytically is exact, however, to continue further with this analysis we must include a closure hypothesis so as to obtain the velocity profile in the channel. For this purpose we can apply Prandtl's mixing length hypothesis, $\mathcal{U} \approx \mathcal{L} \left|\frac{\partial \overline{u}}{\partial y}\right|$, where $\mathcal{U}$ and $\mathcal{L}$ are the characteristic length and velocity scales of an eddy. Moreover, we will apply the Boussinesq closure hypothesis, in which the kinematic viscosity ν is substituted by the eddy viscosity K, Eq. 2.20. Even though this theory is purely empirical it can approximate reality quite satisfactorily. For more information on this refer to [30]. To apply this hypothesis we need to divide the channel into 2 regions, the core region and the wall region, also referred to as the inner and outer regions.

$$K = \mathcal{U}\mathcal{L} = \mathcal{L}^2 \left|\frac{\partial \overline{u}}{\partial y}\right| \tag{2.20}$$

Core Region
This comprises the center or core of the channel. Here, it can be assumed that the eddies scale with the size of the channel, so $\mathcal{L} = \beta H$. Furthermore, if the flow is fully turbulent then the viscous stresses are negligible. If we apply the expression for the eddy viscosity as presented in Eq. 2.20, then Eq. 2.19 reduces to:

$$\frac{\tau_t}{\rho_0} = -\overline{u'v'} + K\frac{\partial \overline{u}}{\partial y} = \mathcal{U}\mathcal{L}\frac{\partial \overline{u}}{\partial y} = \mathcal{L}^2 \left|\frac{\partial \overline{u}}{\partial y}\right|\frac{\partial \overline{u}}{\partial y} = \beta^2 H^2 \left|\frac{\partial \overline{u}}{\partial y}\right|\frac{\partial \overline{u}}{\partial y} = u_*^2 \left(1 - \frac{y}{H}\right) \tag{2.21}$$

This expression can be integrated to reach the solution in Eq. 2.22, where u_0 is the center channel velocity and β is a constant that can be extracted from experimental data and has a typical value of around 0.13.

$$\overline{u} = u_0 - \frac{2}{3}\frac{u_*}{\beta}\left(1 - \frac{y}{H}\right)^{\frac{3}{2}} \tag{2.22}$$

Wall Region
As we approach the wall the assumption that the eddies scale with the channel size no longer holds due to the influence of the wall. However, we can apply $\mathcal{L} = \kappa y$, with the "Von Karman" constant κ, for more information refer to [30]. Furthermore, from experimental wall data it has been demonstrated that $\tau_t \approx \rho_0 u_*^2$, so if the flow is fully turbulent it holds that:

$$\kappa^2 y^2 \left| \frac{\partial \overline{u}}{\partial y} \right| \frac{\partial \overline{u}}{\partial y} = u_*^2 \tag{2.23}$$

Thus:

$$\overline{u} = \frac{u_*}{\kappa} ln\left(\frac{y}{y_0} \right) \tag{2.24}$$

This section is normally referred to as the **logarithmic wall layer** for obvious reasons. The integration constant y_0 will be discussed in a later section. This law is self-similar and is usually presented in it's non-dimensional form, Eq. 2.25. The values of κ & B are independent of the Re, however, the values found in the literature vary. For this study the values used are 0.41 and 5 respectively.

$$u^+ = \frac{1}{\kappa} ln y^+ + B \tag{2.25}$$

Under close analysis it can be seen that this solution does not hold when y = 0. This means that some of the assumptions made no longer hold when we are very close to the wall. To be specific, if go back to the definition of the eddy viscosity, $u_*^2 = K\frac{\partial \overline{u}}{\partial y}$, and introduce into it Eq. 2.24 we obtain that $K = \kappa u_* y$. As can be seen, K becomes smaller as y decreases, therefore, there will be a point where $K \approx \nu$ and the viscosity effects become dominant. The region where this is applicable is referred to as the **viscous sublayer**, neglecting the turbulent stresses it follows that:

$$u_*^2 = \nu \frac{\partial \overline{u}}{\partial y} \qquad \xrightarrow{\int} \qquad \overline{u} = \frac{u_*^2}{\nu} y \tag{2.26}$$

This new expression satisfies the boundary conditions at y = 0.

At this point we have derived three different expressions for the mean velocity profile at three different regions, to determine the complete velocity profile we need to couple them using some kind of matching conditions. First, we start with the intermediate zone between the viscous sublayer and the logarithmic layer, typically referred to as the **buffer layer**. We will introduce the following dimensionless variables:

$$u^+ = \frac{\overline{u}}{u_*}; \qquad y^+ = y\frac{u_*}{\nu} \tag{2.27}$$

From experimental measurements, some of the data is presented in Fig. 2.11, it has been found that the viscous sublayer profile, Eq. 2.26, is valid for $y^+ < 5$. Meanwhile, the logarithmic profile, Eq. 2.24, is valid for $y^+ > 30$. Furthermore, the two solutions match at $y^+ = 11$, thus $y_0 = 0.135\frac{\nu}{u_*}$ [30]. Note, that this is the point where the two analytical solutions differ the most from the measurements, and in the region $5 < y^+ < 30$ the expressions derived do not hold.

To find the expression for the mean velocity profile in the transition zone between the logarithmic layer and the core region it is assumed that their expressions, Eq. 2.24 & 2.22, match at a height $y = \alpha H$, therefore:

$$\frac{u_*}{k} \left\{ ln\left(\alpha \frac{u_* H}{\nu} \right) + 2.0 \right\} = u_0 - \frac{2}{3\beta} u_*(1 - \alpha)^{\frac{3}{2}} \tag{2.28}$$

The constant value of +2 in the left side of the expression is derived by introducing the non-dimensional variables from Eq. 2.27 and the derived expression for y_0 in the logarithmic wall layer profile. The values of the other constants introduced, α and β, can be found in the literature [30]. Therefore, after this analysis, the boundary layer can be divided into the sections depicted in Fig. 2.12.
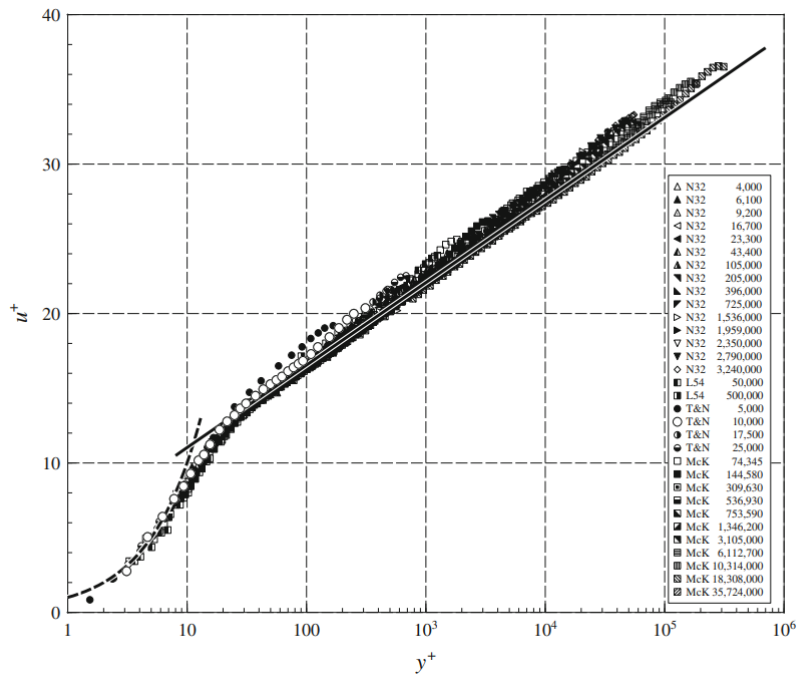
Figure 2.11: Dimensionless mean velocity profile vs dimensionless wall distance for turbulent pipe flow. The solid and broken line correspond to the profiles 2.24 & 2.26 respectively. [30]
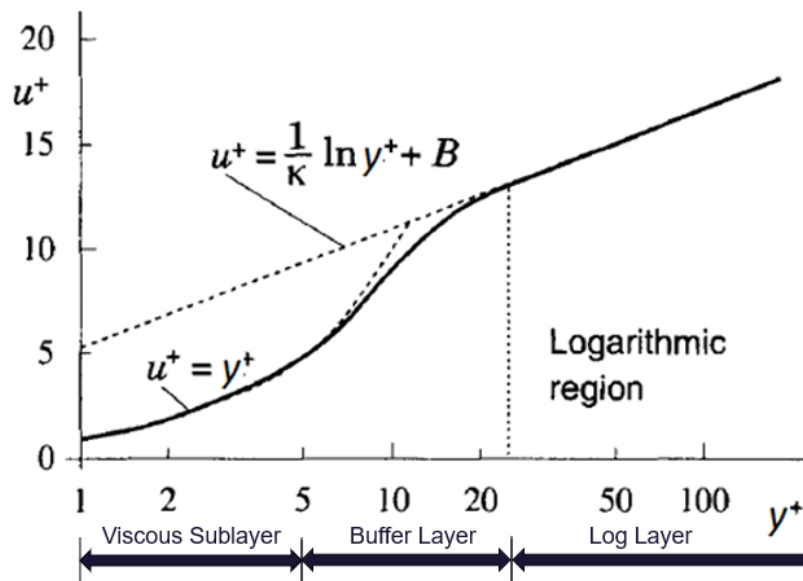
Figure 2.12: The law of the wall, non-dimensional velocity u^+ vs y^+, adapted from [31]

2.4.2. Power Law

For laminar pipe flows a parabolic relationship can be analytically determined for the velocity profile, Eq. 2.29 [32]. For turbulent flow it is not possible to derive such an equation. However, some successful models have been established by fitting curves to experiment or numerical data like the power law model, Eq. 2.30 [33]. Where the exponent n is, in general, a function of the Re.

$$\frac{U}{U_0} = 1 - \left(\frac{r}{R}\right)^2 \tag{2.29}$$

$$\frac{U}{U_0} = \left(1 - \frac{r}{R}\right)^{\frac{1}{n}} \tag{2.30}$$

This model has two issues, first, the derivative at the centerline point is non-continuous, and second, when the Re is very low it does not approach the laminar flow profile from Eq. 2.29. For this reason, Salama A. [32] developed a new modified model:

$$\frac{U}{U_0} = \left[1 - \left(\frac{r}{R}\right)^m\right]^{\frac{1}{n}} \tag{2.31}$$

In his study the model was compared against CFD data to determine the values of the parameter m & n. It was concluded that a constant value of m = 2 over the whole Re range was appropriate ($10^4 - 10^7$). Meanwhile, for the parameter n it was determined that the best option was a logarithmic equation, Eq. 2.32.

$$n = 0.77ln(Re) - 3.47 \tag{2.32}$$

This model has been used as a comparison/validation tool for the velocity profile in the wind-tunnel. However, care must be taken, this model has been established for a round pipe, and even though in [32] it is stated that this same formulation could be developed for a non-circular pipe, like a square, no such model has been found. Therefore, this model will be used as a benchmark, but some deviation is to be expected.

2.4.3. Defect Law

Previously, it was shown that in the outer region, formed by the core and logarithmic region, the friction velocity u_τ and the channel height H are the characteristic velocity and length scale. This means that a scaling law could be applied to the velocity profile in the form of:

$$\frac{U_0 - <U>}{u_\tau} = F\left(\frac{y}{H}\right) \tag{2.33}$$

U_0 is a reference velocity, this would be the centerline velocity for a pipe or channel flow. This equation is referred to as the defect law, it describes a universal scaling behaviour for the outer region. In Fig. 2.13 it is depicted for round pipe flow, however, independent of the flow type, the slope always approaches the reciprocal of the von Karman constant, -2.5 [30].
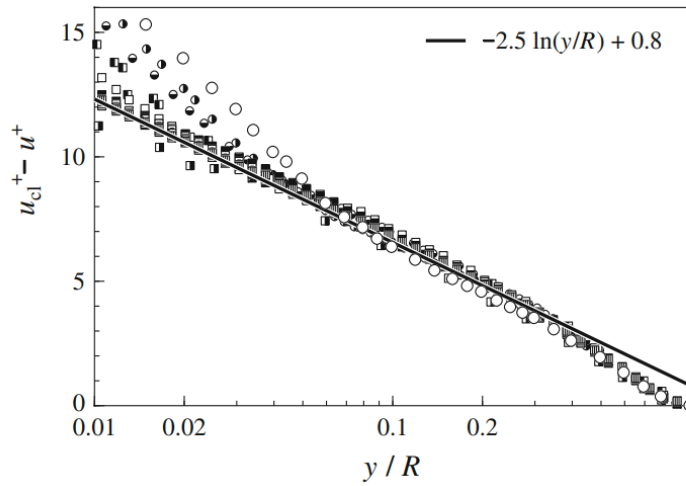
Figure 2.13: Defect law for a turbulent pipe flow [30]

2.4.4. Channel Flow Development

So far, only a channel flow has been considered in which the flow is fully developed. For the scope of this thesis, however, we generally have to consider that the first section of the duct is characterized by the development of the boundary layer, due to changes in the section shape, size, etc. In Fig. 2.14 the BL development in a pipe is depicted for a laminar flow. The boundary layer region where the viscous effects dominate thickens until the point where the whole pipe is dominated by viscous effects, as we are in a laminar flow. Herein, the velocity profile remains unchanged and the flow can be considered to be fully developed. The distance at which this is achieved is referred to as the hydrodynamic entrance length, L_h.
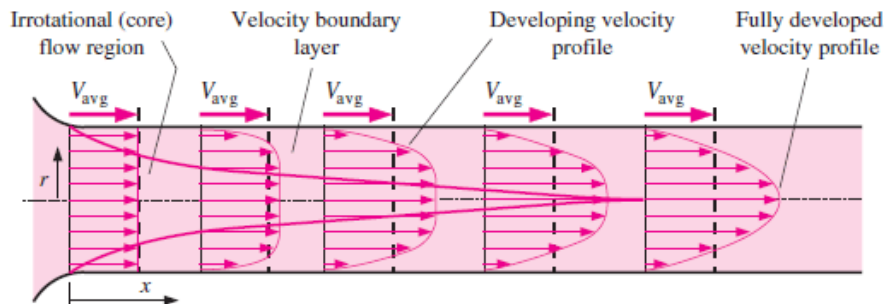
Figure 2.14: Velocity boundary layer development for laminar flow in a pipe.[34]

This length will depend on the Reynolds number (Re) and on whether or not the flow is laminar or turbulent. For a round pipe this length can be obtained by using [35],[36]:

$$L_{h,laminar} = 0.0575 Re D_h \tag{2.34}$$

$$L_{h,turbulent} = 1.358 D_h (Re)^{1/4} \tag{2.35}$$

As can be seen, for a laminar flow L_h depends linearly with the Re, while for a turbulent it is to the power of 1/4. Thus, for a turbulent flow, the entrance length is much shorter. In most practical applications an L_h of 10*D_h is usually accepted since the entrance effect becomes negligible [36]. However, others recommend different values, for example Nikuradse recommends up to 40*D_h [37].

A thermal entrance length can also be defined, this would be the distance required to stabilize the temperature profile. In general, if the Pr is close to 1 ($Pr_{air} \approx 0.71$) this thermal entrance length will be approximately equal to the hydrodynamic entrance length.

2.4.5. Heat Transfer

Heat transfer (HT) is the process through which thermal energy is transmitted from one point to another due to a spatial difference in temperature, either in a medium or between different media. This process can take place through three different "modes": conduction, convection and thermal radiation. The last mode takes place whenever a surface has a finite temperature above the absolute zero, emitting electromagnetic waves that reduce the internal energy of the emitter object [35]. However, this HT mode is of little importance for this study due to the nature of the research objective. Due to this, only conduction and convection will be described more extensively.

Conduction

Conduction takes place in solids or fluids that present no macroscopic motion. This would be applicable to solids and fluids confined in thin places or in micro-gravity conditions. When looking at any media from an atomic standpoint, all molecules will be vibrating and/or rotating, this motion is directly related to the energy level of that particular particle. Temperatures are just a measure of this internal energy. Therefore, the higher this internal energy of the particles, the higher the temperature of the media. If two regions present a different temperature then, as molecules vibrate and collide, there will be a momentum exchange, and inherently an exchange of energy. This is the underlying physical process behind conduction. This heat transfer mode can be quantified by using the Fourier law:

$$\dot{q} = -k\nabla T = -k\left(i\frac{\partial T}{\partial x} + j\frac{\partial T}{\partial y} + k\frac{\partial T}{\partial z}\right) \tag{2.36}$$

From this equation it is important to note that conductive heat transfer takes place in every direction in which there is a temperature gradient. Furthermore, the negative sign in front of the expression denotes that the heat flux will travel in the opposite direction of the temperature gradient. Namely, in accordance to the Second Principle of Thermodynamics, heat travels from hotter to colder regions, increasing the entropy of the system.

Convection

Convective heat transfer can be divided into two main mechanisms. The first is diffusion, and it is associated to the random motion of molecules, similar to conduction, but now the particles are able to change of location. The second is due to the macroscopic motion of the media. For this study convection is of special interest, that is the HT between a moving fluid and wall surface due to a temperature difference between them.

A distinction can be made between free and forced convection. The former occurs when there is a density difference in the fluid which creates some motion due to the buoyancy effect. An example of this would be the scenario where a fluid is in contact with a surface which is at a different temperature. Moreover, in regions of very low flow velocity, like the boundary layer, diffusion dominates. Nonetheless, note that exactly at the fluid-wall interface, where the fluid velocity is exactly 0, only conduction occurs. On the other hand, forced convection occurs when an external force induces the flow motion, for example, with a fan drive. Regardless of the mechanism in place, convection is described by Newton's law of cooling:

$$\dot{q} = h(T_w - T_{f,\infty}) \tag{2.37}$$

It can be observed that the convection heat transfer is directly proportional to the temperature difference, with proportionality constant h, the heat transfer coefficient. From the definition presented, the heat flux $\dot{q}$ will be positive when the wall temperature T_w is higher than the main-flow temperature $T_{f,\infty}$ and thus energy is being added to the fluid.

Thermal Boundary Layer

In Section 2.4.1 it was demonstrated how the velocity will form a boundary layer where the velocity decreases progressively until it matches the no slip condition at the wall. Just like with the velocity, there will also be a thermal gradient next to the wall. The derivation of the equations will not be shown here, however, it can be demonstrated that the thermal and momentum boundary layer have the same behaviour. However, the thermal boundary layer differs by a factor, the Prandtl number, as can be

observed in Eq. 2.38. A is a function of Pr that needs to be determined. The Pr is introduced in Sec. 3.2.1, but for air $Pr \approx 0.7$ so both layers behave very similarly.

$$\frac{T_w - \overline{T}(y)}{q_w/(\rho c_p u^*)} = \begin{cases} Pr y^+ & 0 < y^+ < 5 \\ \frac{1}{\kappa} \ln y^+ + A(Pr) & y^+ > 30 \end{cases} \tag{2.38}$$

2.5. Wall bounded turbulent flows (Rough)

Up to this point the focus has been placed on explaining the flow behavior without considering the properties of the wall. We have assumed a perfectly smooth wall, but in reality, all materials will have some irregularities, roughness. This has already been characterized in Sec. 2.3.2.

As in the previous section, we will first look a the effect on mean flow and boundary layer, moving on to the effect on heat transfer. Furthermore, we will explore the research that has been done regarding these topics, building up to the present state of the investigations of Additive Manufacturing induced surface roughness.

2.5.1. Roughness Effect on Flow

The first studies on the effect of surface roughness on flows date back to the 19th century, conducted by Hagen [38] and Darcy [39]. The latter would go on to modify the Prony equation, for calculating head loss due to friction, together with some added modifications by Julius Weisbach. Their new empirical equation relates the head loss to friction and pressure loss and is known as the Darcy-Weisbach equation, see Eq. 2.39. It contains the dimensionless friction factor, the Darcy friction factor f_D.

$$\frac{\Delta p}{L} = f_D \frac{\rho}{2} \frac{<v>^2}{D_H} \tag{2.39}$$

Some time later, Nikuradse [37] continued upon this work by conducting a series of experiments where he measured the flow friction through a rough pipe. To do this, he glued carefully seived sand grains to a smooth tube, so as to artificially vary the roughness. This methodology gave rise to the roughness parameter known as sand grain roughness, k_s. Schlichting [40] performed some similar research in which he used different roughness elements like cones, rivets and bumps, relating their effects to Nikuradse's sand grains friction losses by defining an "equivalent sand grain roughness". Others like Moody [41] & Colebrook and White [42] continued these investigations using actual physical roughness. Moody developed the famous diagram that has his name which relates the Darcy friction factor, Reynolds number (Re) and relative surface roughness $\frac{\epsilon}{D}$ for a fully developed circular pipe flow, see Fig. 2.15.

To understand how important of an effect the roughness is going to have on the flow we can look at the so called "Roughness Reynolds Number", which is defined as hu^*/ν. This gives a ratio between the roughness height and the thickness of the viscous sublayer. If it is < 1 the wall can be considered as smooth, so the flow behavior remains unchanged [30].

However, if it is > 1 then two different roughness regimes can be identified. If Re_k is smaller than a certain threshold then it is considered as a transitionally rough regime, where both viscous and pressure forces are involved. On the other hand, if it is higher than this threshold, we are in the fully rough regime and the viscous sublayer is completely destroyed and inertial effects dominate. A reference value of this threshold can be found in the literature [9].

Mean Flow

The effect of the roughness perturbation on the boundary layer results in an increase in the wall shear stress, and thus a change in the near wall velocity profile. However, the effect of the roughness remains contained in the roughness sublayer, which extends three to five roughness heights above the the surface [9]. Meanwhile, the outer layer remains unchanged. This can be observed in Fig. 2.16, the mean velocity profile is similar to that of a smooth wall, but with a downwards shift (ΔU^+).
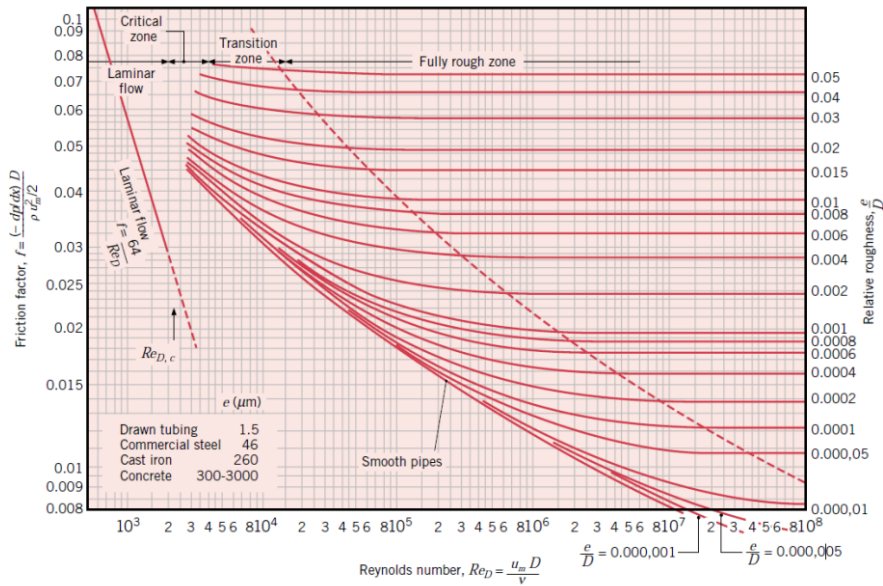
Figure 2.15: Moody Diagram [35]

Clauser studied this and found that roughness only induces a downwards shift, see Eq. 2.40, in of the log-law profile as a function of the roughness Reynolds number. Furthermore, he developed the Clauser chart method, which is widely used as an indirect technique to determine u^* from boundary layer experimental data, this method will be used in this study and is explained in Sec. 3.4.1.

$$U^+ = \frac{1}{\kappa} ln y^+ + C - \Delta U^+ \tag{2.40}$$

This formulation can be applied from $y^+ > 50$ and $y/\delta < 0.2$. The values for the constants k and B employed have been already presented in Sec. 2.4.1. Finally, $U(y)$ and U_∞ can be obtained from the experimental measurements. The term ΔU^+ has been characterized by means of roughness functions that relate the downwards velocity shift to some kind of roughness measurement. Again, this function is not universal and typically depends on the type of roughness.

2.5.2. Roughness Effect on HT

Now we shift our focus from the flow properties, i.e. pressure drop, to the heat transfer characteristics. The first studies around this topic for rough pipe flows were performed by Cope in 1941 [43]. He placed some artificial surface roughness in water cooled pipes and tested how these enhanced the heat transfer with respect to a smooth pipe. The results showed that is was possible to increase the heat transfer while maintaining an equivalent pressure drop. Later, Dipprey and Sabersky [44] measured the heat transfer and friction factor of tubes with sand-grain type roughness at different Prandtl numbers. To achieve this, distilled water was employed as the working fluid and it's bulk temperature was changed using electrically heated tubes. They attempted to apply a heat-momentum transfer analogy and compared their results to both theoretical and experimental results that exited previously. During the period between the 1950s and 1980s interest shifted to heat transfer enhancement produced by artificial roughness which would be used inside of nuclear reactors. An example of this is the work done by Donne and Meyer [45], who in 1977 performed their study using two-dimensional rectangular ribs. In this same publication they presented a new method in which, by using the Stanton number, they attempted to formulate a correlation between the friction factor and heat transfer.

As mentioned, these studies focused on artificial roughness, but in the past decades interest has now shifted into physical roughness, especially that produced by AM. Researchers like Wong et al. [46] and Cormier et al. [47] investigated the effect on heat transfer of a variety of artificial roughness, like
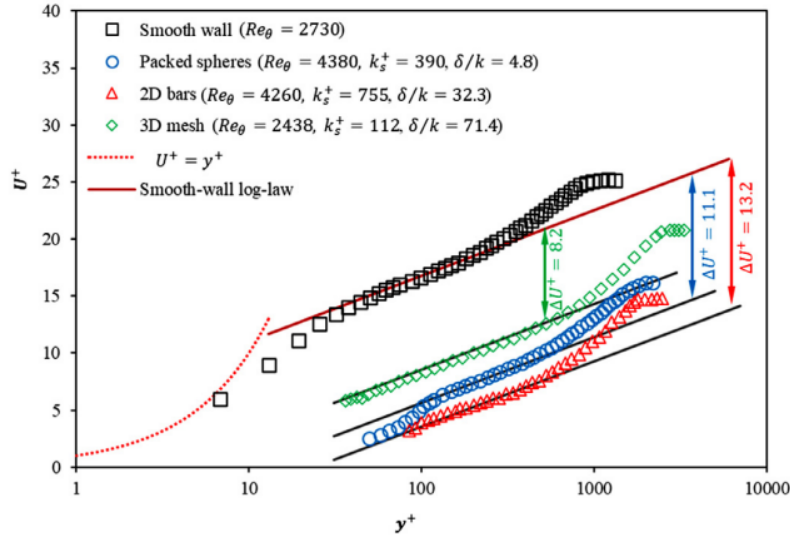
Figure 2.16: Downwards shift of the mean velocity profile for different rough surfaces. Extracted from [9]

fins, manufactured using AM technology. However, it is not until the study by Ventola et al. [48] published in 2014 that interest was placed on the effect of AM induced surface roughness. In their study they measured a convective heat enhancement of up to 73% (63% on average) on a rough flat surface manufactured using Direct Metal Laser Sintering. Nonetheless, they only focused on external surfaces, some of the first studies investigating AM roughness in internal flows were performed by a research group from the Pennsylvania State University. In their first publication from 2016 [49] Stimpson et al. studied the effect that the build direction has on AM channels. For this purpose they used some coupons built using DMLS that had different rectangular micro-channels printed in them. Their results showed that the pressure drop was significantly affected by the build direction, however, the heat transfer was unaffected. In another of their studies [50], published shortly after, they found that the roughness greatly increased both the pressure drop and the heat transfer coefficient. However, they discovered that the increase in heat transfer was not proportional to the increase in friction factor. Later that year, in a different study [29], they analyzed the surface roughness parameter of the channels they had previously tested. They found that the relative arithmetic mean roughness correlated well with the equivalent sand grain roughness from Nikuradse. Furthermore, they presented a correlation to predict the Nusselt number value of the AM channels.

In conclusion, the increase in roughness will imply an enhancement on the heat transfer when compared to a smooth surface. The mechanisms behind this are somewhat understood, however, no analogy or scaling laws have been found yet. The regions of thinnest thermal boundary layer, which will normally be found in the windward locations, corresponding to impingement zones [51], is where highest heat transfer should be located. On the other hand, the regions of detaching or reversed flow correspond to thick thermal boundary layers that will have lower heat transfer.

Although the mechanism that explain HT are complex, there are empirical correlations that relate the most common dimensionless parameters to heat transfer. One such example is the correlation developed by Dittus-Boelter, as shown in Eq. 2.41, which is applicable for fully developed turbulent flows in smooth circular pipes with $0.6 < Pr < 160$, $Re > 10000$ & $L/D_h > 10$. Other correlations, such as that proposed by Gnielinski, also exist, but they will not be presented.

$$Nu_{DB} = 0.023 Re^{\frac{4}{5}} Pr^n \qquad (2.41)$$

2.6. Particle Image Velocimetry

The recently developed Particle Image Velocimetry (PIV) method is very useful as it can be used to study the flow behavior in a non-intrusive manner. The first studies that applied this technique to this field of study were carried out by S.Y Son et al. [52] and investigated the effect of ribbed walls on the wall heat transfer. To do this, they correlated the averaged velocity and turbulent kinetic energy distributions with some experimental heat transfer measurements obtained in a different study. By doing this, they were able to find that the heat transfer increase was mainly due to the higher local flow impingement near the ribs. In a more recent study, [53] by Y. Kuwata et al., PIV was used to investigate the effect of rough walls in a channel flow. They studied the effect of the effective slope ES and skewness factor S_k on the transition behavior to fully rough regime and discovered that the effect of S_k is quite limited, while that of ES is more important up to a value of $ES >= 0.18$ where it no longer as a noticeable impact. In other studies, like that by C. Shingote [54], PIV was used to study the boiling flow behavior inside of a heated channel.

This technique allows for the measuring of the instantaneous velocity field within a planar section or even a 3D volume. Due to these qualities Particle Image Velocimetry (PIV) is a good technique to study the influence roughness has on the flow behaviour and turbulence generation. This section will provide an overview of the technique, beginning with its fundamental principle and subsequently explaining some basic concepts: flow seeding, imaging, and illumination.

2.6.1. Basic Principle

This technique is based on measuring the displacement experienced by some tracer particles that are injected into the flow. The particles are illuminated by a intense light sheet that is typically generated using a laser and some lenses. The particles will reflect some of this light and this is recorded on two images, taken within a very short time interval. To do this a camera is placed perpendicular to the generated light sheet, see Fig. 2.17 for a typical PIV experiment setup.
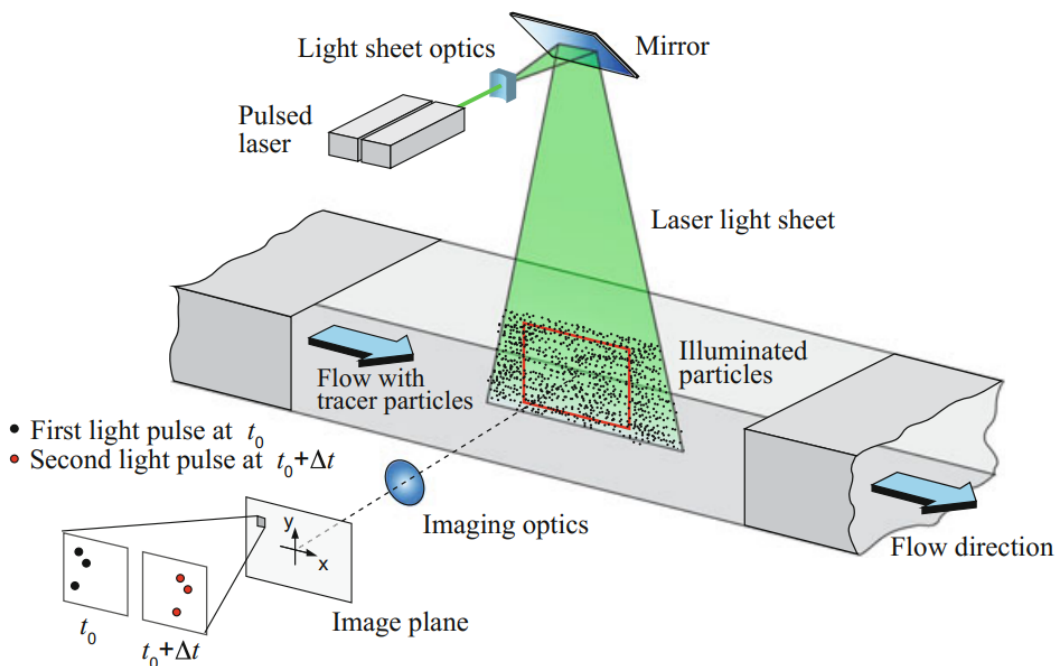
Figure 2.17: Typical 2D PIV experimental setup from [55].

The recorded images are analyzed by means of a computer software that cross-correlates the images, finding the displacement of a local group of particles. For this, the image is divided into smaller windows, called interrogation widows. Then, the statistical cross-correlation algorithm is applied on the small interrogation windows and it returns a cross-correlation map where the position of the

peak indicates the particle displacement in x and y coordinates for that window. The highest peak would correspond to the motion of the particles within that interrogation window. The displacement is obtained in pixels, so it has to be translated into real life distance, then it can be divided by the laser pulse separation time to find the particle's velocity.

2.6.2. Flow Seeding

PIV measures the velocity of the tracer particles, not the velocity of the flow. For the particles to follow the flow without slip they need to satisfy some specific size and mass conditions. To determine these we can assume that, for a very small particle, the quasi steady viscous term dominates the particle dynamics, Eq. 2.42 . Where d_p is the trace particle diameter, μ is the fluid dynamic viscosity, ρ_p is the seeding particle density and ρ_f is that of the fluid. The velocity U_f corresponds to the fluid velocity and U_p to the particle.

$$U_f - U_p = \frac{1}{18} \frac{d_p^2 (\rho_p - \rho_f)}{\mu} \frac{dU_f}{dt} \qquad (2.42)$$

This velocity difference is known as the slip velocity and it should be close to 0. To achieve this either $\frac{(\rho_p - \rho_f)}{\rho_f} << 1$ or particles with very small diameters can be used. Achieving the first condition in air is not possible, therefore particles with diameters of $0.5 - 5\mu m$ are employed. These can be either solid particles or smoke. An easy way to quantify this particle behavior is through the Stokes number, Eq. 2.43. τ_f can be approximated as $\frac{L_f}{\Delta U}$. τ_p can be obtained from solving Eq. 2.42, the step response time typically follows an exponential decay law in the form of $U_p = U_f(1 - e^{-t/\tau_p})$, which results in $\tau_p = d_p^2 \frac{\rho_p}{18\mu}$. As can be observed in Fig. 2.18 this response time is most sensitive to the particle size.

$$Stokes\ number = \frac{particle\ response\ time}{flow\ characteristic\ time} = \frac{\tau_p}{\tau_f} \qquad (2.43)$$
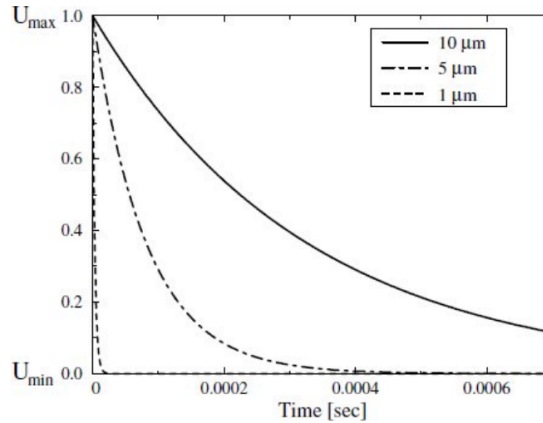
Figure 2.18: Time response of oil particles with different diameters. [56]

Not only this, but the particles need to scatter enough light to be captured by the camera. For this reason, when testing with air, usually oil droplets or solid particles like aluminum oxide (AlO_2) are used. The light scattering behaviour also depends on the incidence angle, as shown from Mie's scattering theory in Fig. 2.19.

2.6.3. Imaging and Illumination

In this study a High Speed Camera has been used together with a pulsed Nd:YAG laser. The most important parameters from the camera are the focal length of the lens, the aperture and the magnification. The maximum magnification will determine the smallest Field of View (FOV) that can be detected by
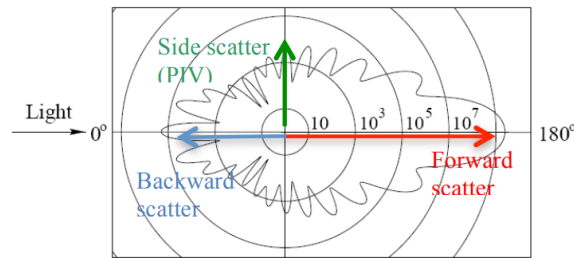
Figure 2.19: Scattered light intensity as a function of the scattering angle for a 1 μm oil droplet in air. [57]

the camera and it is a very important parameter that needs to be used when obtaining the velocity field. This parameter can be calculated as:

$$M = \frac{sensor\ size * pixel\ pitch}{FOV} \tag{2.44}$$

The aperture number, which is included within the f-stop value, is of vital importance. This is because it will largely affect the diffraction effect, and thus the apparent size of the particles in the captured images. To get an accurate value of the particle displacement the apparent particle size needs to be bigger than one pixel. If it is smaller then the displacement can only be determined in steps that are of the size of the pixel pitch. This is called "peak locking" or "pixel locking". A good apparent size is of 2 to 3 pixels, so that the displacement can be interpolated from the pixel light intensity. If the size is larger this can give rise to problems as some particles might overlap. See Sec. 3.2.5 for the calculation of the particle image size and the aperture number used in the present research.

The most common device used for illumination, due to the intense light requirements and short time intervals, is a solid-state double pulsed Nd:YAG laser, emitting light at a frequency of 532 nm. These lasers typically produce a pulse of about 20 - 500mJ energy with a very short pulse duration that range from 5 to 15 ns. However, their repetition rate is quite small, typically from 10 - 30 Hz, which means that they are not good enough to perform a time-resolved PIV. To solve this issue, a Nd:YLF laser can be employed.

2.7. Computer Fluid Dynamics

Recent studies are not only limited to experimental research, with the advancement of technologies and increase in computing power it is now possible to run Computer Fluid Dynamics (CFD) simulations modeling the AM induced surface roughness. However, this is challenging, as the physical surface roughness, specially that from AM, presents a wide variety of topographical features that are complicated to characterize. Hanson et al. [58] used both a numerical and experimental approach for their research. Using x-ray tomography they extracted the roughness patter of an AM channel and using an ellipsoid distribution they created two surfaces that replicated the measured roughness statistical parameters. They then upscaled the generated geometry by a factor of 102x so as to 3D print it and test it in the wind tunnel. The results from this experiment were combined with a Reynolds-Averaged Navier Stokes CFD simulation to obtain a detailed view of the flow field and it's behavior. The surfaces generated with ellipsoids presented 30% lower friction factor when compared to the original engine-scale channel, however, the baseline up-scaled rough channel differed by approximately 15%.

Other CFD studies focus more on the local heat transfer effects which are not understood as well as the mean flow effect. Studies like that from Kevin Zhong et. al. [59] try to validate previously proposed models for the heat-transfer coefficient. However, they found that overall heat transfer presents distinct local mechanisms depending on the flow region. In a later study [60], by the same research team, found that the heat and momentum transfer analogy breaks down as the fully rough regime is approached. Furthermore, they break down the heat transfer into two distinct zones: exposed and sheltered regions. The first are high-shear regions with high heat transfer, while the latter are reversed-flow regions

experiencing lower and more uniform heat transfer. They try to find a model for the heat transfer coefficient based on this idea.

CFD relies on solving numerically some discrete form of the Navier-Stokes equations, that govern fluid-motion [61]. When these are solved without any modeling, capturing all the turbulent scales, then it is refer to as a Direct Numerical Simulation (DNS). Kolmogorov proposed the small turbulent scale universality hypothesis, asserting that at these scales, ruled by viscosity, the statistical properties become universal and dominated by the energy cascade and the dissipation rate [62]. This allows the modeling of the small scales, only resolving the large turbulent scales that have a big impact on the flow behavior. This approach is know as Large Eddy Simulation (LES) [61].

Both DNS and LES present a problem: high computing power and time requirements. This is because these methods require a very fine mesh grid so as to resolve the turbulent eddies. Furthermore, as the Re number increases the smallest turbulent scales become smaller, further increasing computing times. For DNS the computational cost scales proportionally to $Re^{9/4}$ while for LES with $Re^{4/3}$ [63]. Nonetheless it is possible to completely model all turbulent scales and perform instead a Reynolds Averaged Navier-Stokes Simulation (RANS). The derivation of the underlying equations can be found in Appendix A, this turbulence modeling vastly reduces computational costs.

<div style="text-align: right; font-size: 4em;">3</div>

<div style="text-align: right; font-size: 2.5em;">Methodology</div>

This chapter will delve deeper into the methodology developed, clarifying how results are obtained and processed. First, the experimental methodology will be described. The task that required the most man-hours, the wind-tunnel test section and PIV system design, will be described here. In a later section, the CFD simulations employed are described and to conclude some important data post-processing methods are depicted.

3.1. AI tools Used

Throughout this project AI tools have been employed, specifically ChatGPT [64]. The great capabilities of this technology meant that the generation of codes, and the learning process of new programming languages, was much simpler. Furthermore, it played a significant role in assisting with the grammar correction of this manuscript.

3.2. Experimental Methodology

As previously mentioned, the wind-tunnel test section had to be designed and manufactured, this topic is addressed first, accompanied by a dimensional analysis of both the wind-tunnel and the surface model to be tested. Additionally, the PIV system developed is described, including the selected PIV instrumentation utilized and image processing techniques employed. Finally, the testing campaigns will be outlined.

3.2.1. Introduction: Motivation for scaled up experiment & Dimensional Analysis

Naturally, the PIV and heat transfer experiments to investigate local effects can not be performed using the real scale channels and working conditions. A typical gas turbine cooling channel operates at pressures that may reach several tens of atmospheres, with temperatures between 600 °C - 1000 °C and flow velocities of $\approx$ 100 m/s, which is possible due to the high air density, which can be 5x higher than that at atmospheric level. This means that the tests have to be performed under dynamically-similar conditions but achievable in a test-lab. Due to this, in the previous studies, it was decided to upscale the channel and also create a new wind-tunnel for this work. The newly designed test section has to be dynamically similar to the real gas turbine cooling channel and to the SRHT rig, in which the heat transfer experiments were performed by W. Kaibin [65]. The up-scaling is discussed in the dimensional analysis presented bellow.

Dimensional Analysis

The experimental campaign carried out for this study and those performed in the lab by previous students depend on a wide range of parameters. In order to reduce the number of variables that need to be tested, a dimensional analysis can be performed, obtaining the relevant non-dimensional numbers that define the flow behavior. Note, that this analysis holds only for the PIV rig. Furthermore, the objective of the new wind-tunnel is to replicate a cooling channel flow, maintaining dynamic-similarity. For a generic pipe flow with heat transfer we would expect the following variable dependencies:

1. Flow conditions: u_m, ρ_{air}, Δp, μ_{air}, k_{air}, $c_{p_{air}}$, ΔT, $\dot{q}$, a_{air}, $\Delta T_{w,f}$

2. Channel geometry: D_h, L_c, k_{solid}, $c_{p_{solid}}$

3. Roughness : R_a, R_z, R_q, R_{sk}, R_{ku}.

To make the analysis more simple we will group the variables into two groups, those that affect only momentum or heat transfer. Note, that due to the nature of the problem some dependencies can be removed. We assume the flow is fully developed, so the flow is independent of channel length L_c. Furthermore, we will group all the roughness parameters under a global variable, the equivalent sand grain height. Note that, there is not theoretical relation between the roughness parameters and this variable. Furthermore, Δp and $\dot{q}$ are the final parameters related to momentum and heat transfer that we want to determine. This means that the independent variables are:

1. Momentum transfer: u_m, ρ_{air}, μ_{air}, a_{air}, D_h, k_s

2. Heat transfer: u_m, ρ_{air}, μ_{air}, k_{air}, $c_{p_{air}}$, a_{air}, D_h, k_{solid}, $c_{p_{solid}}$, k_s, $\Delta T_{w,f}$

If a dimensional analysis is performed following Buckingham's π-theorem, as shown in [66] [67], we would obtain that for momentum transfer there are 3 units while for HT there are 4. This means that we will obtain 3 independent non-dimensional numbers for momentum transfer and 7 for HT. The selected independent variables are D_h, μ_{air}, u_m, k_{air}. This results in the following non-dimensional numbers:

1. Momentum transfer: $\mathrm{Re} = \frac{\rho_{air} u_m D_h}{\mu_{air}}$, $\mathrm{Mach} = \frac{u_m}{a_{air}}$, $\frac{k_s}{D_h}$

2. Heat transfer: Re, Mach, $\frac{k_s}{D_h}$, $\mathrm{Pr} = \frac{c_{p_{air}} \mu_{air}}{k_{air}}$, $Pr_{solid} = \frac{c_{p_{solid}} \mu_{air}}{k_{air}}$, $\frac{k_{solid}}{k_{air}}$, $\frac{\Delta T_{w,f} k_{air}}{u_m^2 \mu_{air}}$

Furthermore, as mentioned previously, to account for pressure losses the Darcy friction factor, as presented in Sec. 2.5.1, will be employed. To characterize the HT we will use the Nusselt number Nu, presented in Eq. 3.1. This parameter is related to the heat transfer coefficient h, that appears in Newton's law of cooling shown in Eq. 2.37, and it will be employed instead of $\dot{q}$.

$$Nu = \frac{h * D_h}{k_{fluid}} \tag{3.1}$$

In the HT we have a few parameters that would not typically appear, these are the ones related to the solid characteristics. In fact, these are not present in the non-dimensional Navier-Stokes equations. However, we have included these here because we consider that the HT inside the solid might be having some kind of influence on the convection HT due to the saturation of the spheres. Furthermore, the last parameter can be modified as follows:

$$\frac{\Delta T_{w,f} k_{air}}{u_m^2 \mu_{air}} = \frac{\Delta T_{w,f} k_{air}}{u_m^2 \mu_{air}} \cdot \frac{Pr}{Pr} = \frac{\Delta T_{w,f} c_{p_{air}}}{u_m^2} \cdot \frac{1}{Pr} = \frac{1}{Ec \cdot Pr} \tag{3.2}$$

Where Ec is the Eckert number. After all these simplifications and assumptions the problem, for a straight channel, reduces to:

1. $f_D = \mathrm{f}(\mathrm{Re}, \mathrm{M}, \frac{k_s}{D_h})$

2. $\mathrm{Nu} = \mathrm{f}(\mathrm{Re}, \mathrm{M}, \frac{k_s}{D_h}, \mathrm{Pr}, Pr_{solid}, \frac{k_{solid}}{k_{air}}, \mathrm{Ec})$

Throughout this section the hydraulic diameter D_h has been used instead of simply D. Its formal definition is $D_h = \frac{4A}{P}$ [68] and this has been employed to evaluate the wind-tunnel D_h. It is important to highlight the importance of the hydraulic diameter evaluation, specially when calculating the Darcy friction factor. This is because f_D is proportional to D_h^5, see the derivation shown in Eq. 3.3. Therefore, a small variation in the diameter value employed will have a very big effect on the resulting friction factor.

$$f_D = \frac{\Delta p D}{L u_m^2 \frac{\rho}{2}} = 2 \frac{D_h}{L} \frac{\rho A^2 \Delta p}{\dot{m}^2} \xrightarrow{A = \frac{\pi D_h^2}{4}} f_D = \frac{\pi D_h^5}{8L} \frac{\rho \Delta p}{\dot{m}^2} \tag{3.3}$$

The Eckert number should not be of significance in our study as the flow is incompressible, as will be seen later through the Mach number. However, the HT experiments performed by W. Kaibin [65] had different values of Pr, as due to the nature of the experiment, they were carried out with a higher flow temperature. However, the difference is 0.5% so its influence is negligible. Also note that, for this project the relative roughness k_s/D_h is kept constant as only one rough surface is being tested. Nonetheless, the roughness tested is an upscaled model of the real roughness, as will be further discussed in the next section. This is because we are testing in a wind-tunnel that has a D_h which is much larger than the original micro-channels, therefore, the original roughness parameters (R_a,R_z, etc.) need to also be upscaled to conserve similarity.

As a final note, it is important to identify which of these parameters are conserved between a real turbine cooling channel flow and the scaled up experiment. Due to the applied up-scaling factor, the relative roughness will be conserved, and also some of the individual roughness parameters. The Re number is also conserved, however, the Pr is not. The materials used are not the same as for a turbine blade so all the parameters related to solid heat transfer are not conserved. Even though the Mach number will not be exactly equal, in general for the turbine cooling channels it is < 0.3, which means that the flow is incompressible. This same analysis is performed for the SRHT rig & CFD data, a compilation of the parameters is presented in the following table:

Table 3.1: List of parameters that remain equal/different between the real turbine cooling channel, SRHT data & CFD compared to the PIV test rig.

Conserved		Different	
Real Turbine	**SRHT & CFD**	**Real Turbine**	**SRHT & CFD**
Re, M, $\frac{k_s}{D_h}$	Re, M, Pr, $\frac{k_s}{D_h}$	Pr, Pr_{solid}, k_{solid}	Pr_{solid}, k_{solid}

In order to simplify and summarize this analysis, a list presenting the characteristic values of the classical parameters found in a real gas turbine are provided in Table 3.2, along with the corresponding values from the PIV rig, SRHT rig and CFD.

Table 3.2: List of parameters that remain equal/different between the real turbine cooling channel, SRHT data & CFD compared to the PIV test rig.

	Real Turbine	PIV	SRHT & CFD
Re	10^4 - 10^5	10^4 - $5 \cdot 10^4$	$2 \cdot 10^4$
M	<0.3	<0.3	<0.3
Pr	0.7 - 1.2	0.708	0.702

3.2.2. Wind-tunnel design

The bulk of the work for this thesis has been designing, building and setting up the experimental rig, which has to be dynamically similar to that of the SRHT rig and allowing for optical access for PIV measurements. A schematic of the newly build wind tunnel at the Siemens Energy Fluid Dynamics Lab for the purpose of this thesis is presented in Fig. 3.1 together with a picture of the testing room. This is a small black room inside of the Fluid Lab designed to block all light, improving the images quality and eliminating any possible risks to other personnel. Tests are performed with the operator outside of the testing room to prevent injuries from the laser. One of the first steps was designing a suitable test section that allowed for PIV measurements in the wind tunnel.

The newly built wind-tunnel is at atmospheric pressure and has a velocity range of $\approx$ 0.9 m/s - 8.33 m/s, resulting in a Re range of $\approx$ 5500 - 53000. It is equipped with an 83W SystemAir K 100 EC sileo fan. At present, the tunnel tunnel does not have any contraction and consists of a straight section. Consequently, the velocity is measured through a direct correlation of fan rpm and volume flow.

The tests mainly involved two different set-ups, with the laser illuminating parallel and perpendicular to the test plates. Therefore, it was necessary to create a detachable design, making it possible to remove the whole test section and simply rotate it by 90° to change the measuring plane.

Even though on most wind-tunnels the blockage effect has a big repercussion and must be accounted for, in this experimental campaign no aerodynamic analysis of a model will be performed, we are replicating

(a) Schematic of the Wind-tunnel.   **(b)** Testing room.
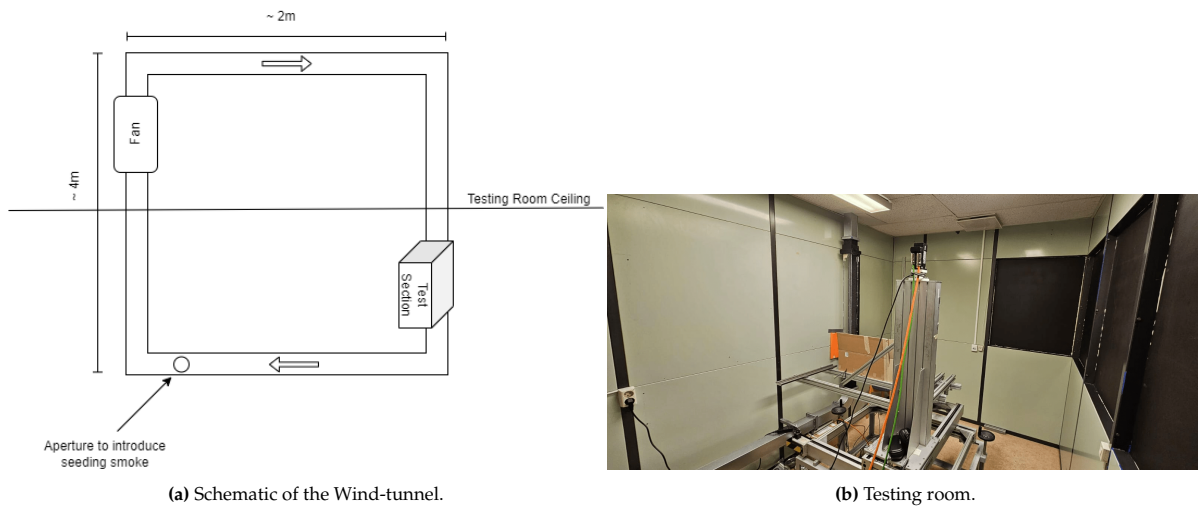
Figure 3.1: Set up of the wind-tunnel and testing room image.

a channel flow. Thus, the decrease in effective cross section due to the boundary layer growth or wake blockage is not an issue in this scenario.

The wind-tunnel section is designed to accommodate the test plates developed by W. Kaibin [65]. A detachable test bed was made to allow easy change of the test plates, as shown in 3.2. The plates are inserted in the central groove and they are kept in place by some side bolts that put pressure on the plates.

Apart from the testing bed, the other side walls must be transparent to allow for PIV measurements. Moreover, as mentioned, this wind tunnel must be dynamically similar to that of the SRHT rig from W. Kabin [65], so that the non-dimensional parameters related to the surface roughness, presented in Sec. 3.2.1, are conserved. For this reason it was decided to create a square test section of dimensions 100x90mm. These dimensions are different from the metallic parts of the tunnel, thus a detachable adapter was designed to attach this new test section to the wind tunnel, presented in Fig. 3.3. The metallic section of the wind-tunnel was slid into the groove of the adapter and glued with epoxy resin.
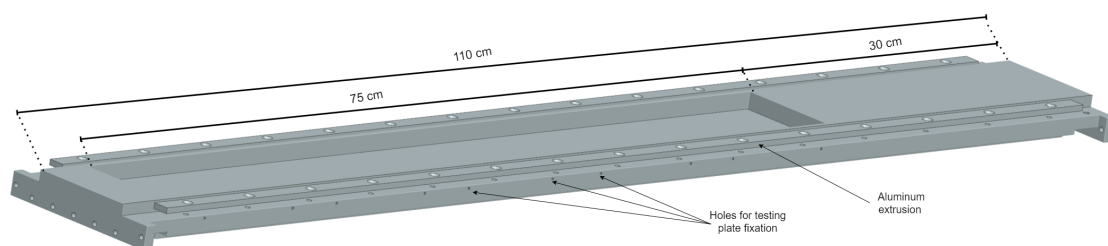
Figure 3.2: Test-bed CAD model.

The final test section design can be observed in Fig. 3.4. The side walls were manufactured using 5mm thick plexiglass and all other components were 3D printed in plastic. To avoid leakages all parts were glued using epoxy and applying silicon. Furthermore, the detachable parts all have gaskets to fill possible irregularities and keep the test section airtight. The long side of the test-bed includes an aluminum extrusion that is bolted to the test-bed. The bolts slide through an overhand/extension of the plexiglass cover and in this way, when they are tightened, pressure is applied, making the test section airtight.

3.2.3. Analogue Rough Surface Modeling

The rough surfaces, from now on also referred to as analogue surface, shown in Fig. 3.8, recreates the upscaled surface roughness of an Inconel 939 printed channel using L-PBF. Even though these were
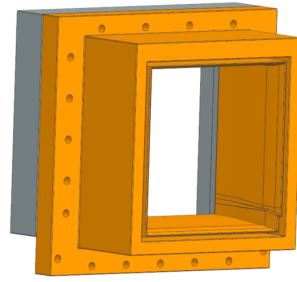
Figure 3.3: Adapter CAD model.
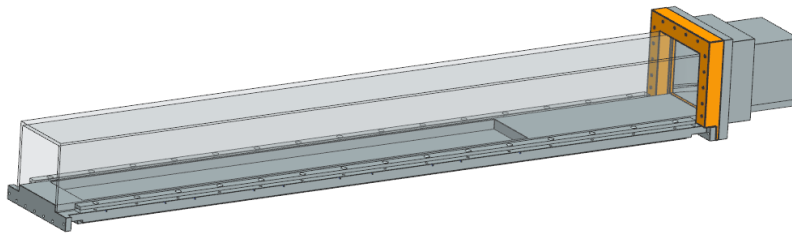
Figure 3.4: Final test section design.

produced by a previous student W. Kaibin [65], due to their importance to the purpose of this work their generation will be discussed here.

To model the SR of the real channel, spheres are randomly distributed with different diameters on a smooth channel by using an in-house developed Python script. This is done in an attempt to replicate the roughness measurements of the real AM surface. This method was inspired by the work done by Clemerson et al. [69], and was implemented by several previous Master thesis students. The roughness investigation was done by cutting in half a L-PBF printed Inconel 939 1.25mm diameter channel manufactured at 90° (vertical). The roughness profile was then measured using a skidless contact stylus profilometer, Fig. 3.5a. A typical roughness profile obtained using this method is presented in Fig. 3.5b. In total 3 measurements were made, the averaged results with their corresponding deviations are listed in Table 3.3.
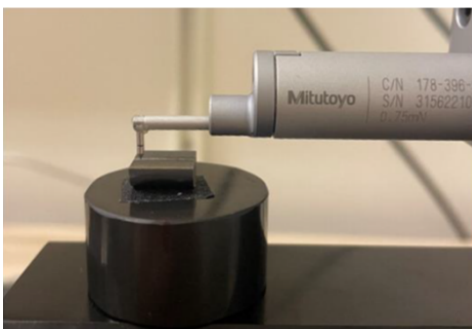
(a) Profilometer Mitutoyo Surftest SJ-410 when measuring.
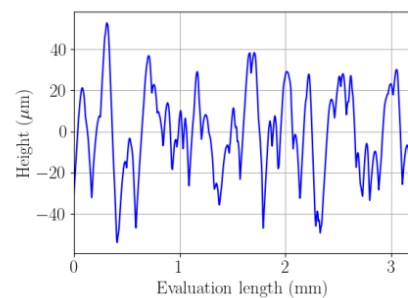
(b) Profilometer measured profile.

Figure 3.5: SEM pictures of the inner surfaces of the tested AM channel [70].

Moreover, some scanning electron microscope (SEM) pictures were made by Björnram and Ljunggren for another Master's thesis [70]. From those pictures, presented in Fig. 3.6, the spheres' dimensions

were characterized. For this purpose, Lehmann [71] manually counted the spheres and recorded their diameters. The method's results vary greatly depending on the user that performs the measurements, but his results serve as a good estimate of the diameter distribution.
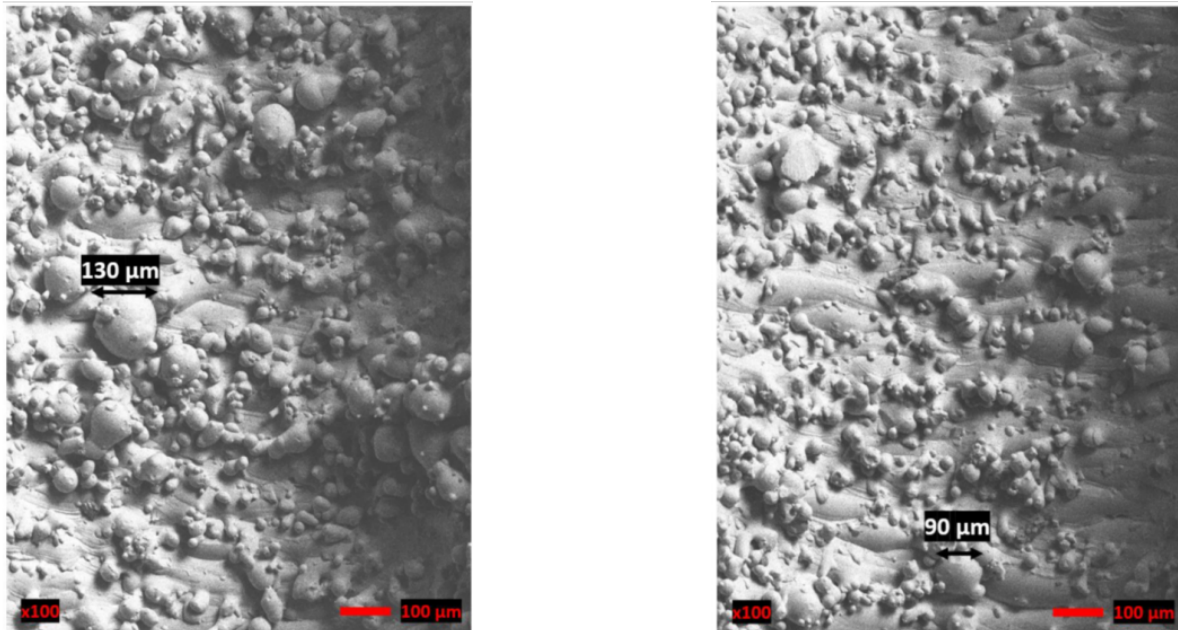
Figure 3.6: SEM pictures of the inner surfaces of the tested AM channel [70].

The measured diameter distribution was matched by W. Kaibin [65] varying the coefficients of a gamma probability function, which is described in Appendix C. However, this did not match satisfactorily the roughness parameters measured. Consequently, a different approach was used, and a relationship was established, by trial and error, between the roughness and the probability distribution parameters. The resulting relation is presented in Appendix C.

Note that these roughness parameters need to be upscaled so as to conserve similarity between the original test object and the wind tunnel channel, as explained in Sec. 3.2.1. The hydraulic diameter of the wind tunnel section from the original investigation from W. Kaibin [65] is of 96.7mm, which is slightly different from the tunnel used for this project. This is due to imperfections on the plexiglass walls, however this is negligible. The original test object had a nominal channel diameter of 1.25mm, therefore, the upscale ratio was originally selected as $r = 96.7/1.25 \approx 77.4$.

Finally, in Fig. 3.7 the measured distribution can be observed together with the gamma function and the generated sphere diameter distribution. The sphere density is also based on the manual selection process described previously, which yielded a total 848 spheres in $2.28mm^2$. This corresponds to a density of 372 spheres/mm^2, however, a slightly higher value was used, of 380. This was done to account for cases where a sphere is fully embedded within a bigger one.

Since the script positions the spheres randomly on the channel surface, and the diameter distribution is fixed, only one parameter remains that can be varied by the user, the offset (Ω). This is the normal distance from the plate surface to the sphere center. This non-dimensional parameter is defined as $\Omega = \frac{offsetdistance}{D_s/2}$. In this way if $\Omega = 0$ then the sphere center is positioned tangent to the smooth surface. Furthermore, from this definition the value of Ω must stay in a range from -1 to +1, if not, the sphere would be either fully embedded in the solid plate or floating in the channel.

To adjust this parameter, the script uses an offset distribution function, just like for the diameters. However, from the SEM pictures the offset cannot be measured, therefore, a simple normal offset distribution was introduced. This function is defined in Appendix C, the final parameters used were $\mu = 0$ & $\sigma = 0.2$ and the function was limited to values within ±0.45. These were also selected based on trial and error, so as to match the roughness measurements shown in Table 3.3. In this same table the
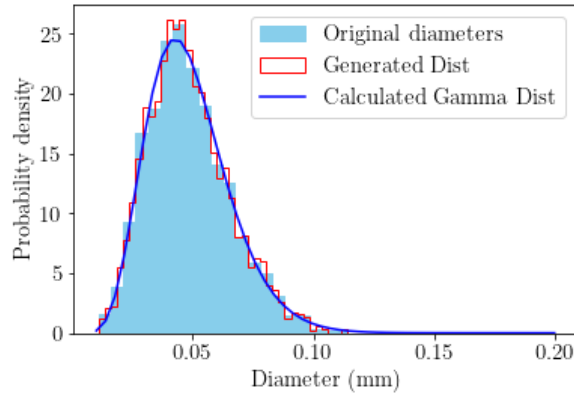
Figure 3.7: Adapted gamma distribution and histogram of the generated & measured sphere diameters.

resulting roughness parameters of the rough analogue surface are presented.

Table 3.3: Roughness profile parameters from the real Inconel 939 sample (90°, 1.5mm), measured with a profilometer, and the generated channel for the simulations.

Profile parameter	R_a	R_z	R_q	R_{sk}	R_{ku}
Measured Average Value	1.077	5.689	1.325	0.46	2.79
Generated Average	1.103	5.741	1.304	0.944	3.157
Deviation [%]	2.41	0.91	-1.58	105.2	13.62

The final geometry can be observed in Fig. 3.8a. Even though some complex features of the roughness which could be seen in the SEM pictures are missing, the generated geometry closely resembles the AM Inconel 939 channel roughness. The plates were then printed via stereolithography using Accura Xtreme grey and a layer thickness of 0.1mm to guarantee a fine surface finish. One of the printed plates is shown in Fig. 3.8b.
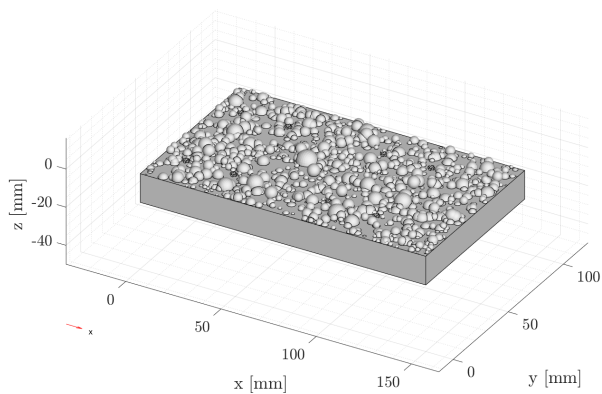
(a) CAD model of the upscaled analogue rough surface.

(b) Printed plate.

Figure 3.8: Upscaled analogue rough surface plate.

3.2.4. PIV Instrumentation

For the PIV testing campaign some very specific instrumentation is required. There are three essential pieces of hardware: a seeding generator to generate the tracer particles, a laser for illumination and a camera to record the image pairs. Other important pieces of equipment are the camera-laser synchronizer

and the PIV processing software. A schematic of the test set up and how all these devices are connected is shown in Fig. 3.9.
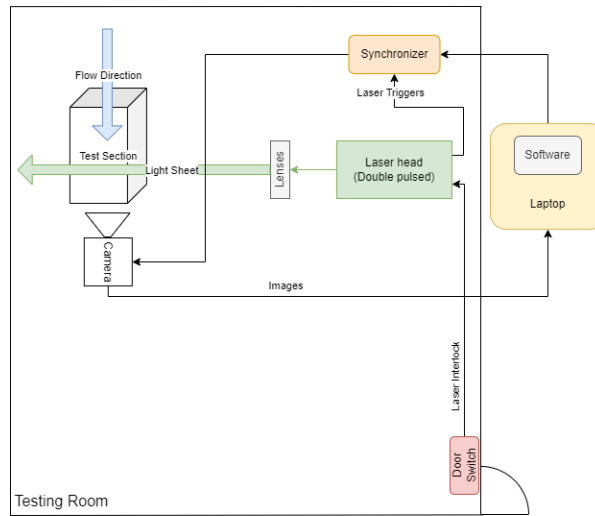
Figure 3.9: Schematic of the testing set-up. Flow direction is perpendicular to the floor.

Seeding Generator

To generate the tracer particles a TINI CX hand held fog generator is used, as shown in Fig. 3.10. It uses a fluid named Tiny Fluid which is a glycol and water based mixture, generating a non-toxic fog. No information has been found regarding the particle size, so it is assumed that the mean droplet diameter (d_p) is of 1 μm.

The value of the droplet size, as explained in Sec. 2.6.2, is important in order to have a Stokes number lower than 1. Using $\tau_p = d_p^2 \frac{\rho_p}{18\mu}$ we obtain that the particle response time is approximately $3.0 \cdot 10^{-6}$s. On the other hand, assuming that the tunnel wind speed is 2.5 m/s, the fluid characteristic time will be of 0.0379s. Therefore, the resulting Stokes number is $\ll 1$ and the particles will correctly follow the flow without slip.

Figure 3.10: TINI CX seeding generator.

Laser

The laser used for the experiments is a Nano-S DualPower65-15 Laser from Litron Lasers. The laser system consists of a double pulsed and Q-switched Nd:YAG laser. It produces infrared laser light at a wavelength of 1064nm, which is then halved to 532nm, visible green light, by a harmonic generator. The maximum energy generated by the laser is 65mJ, thus, it is considered a Class 4 laser. For this reason, a special course and safety analysis had to be performed, however, these are not included as they are not of interest for the purpose of this report. The pulse duration is of 4ns and the maximum repetition rate is of 100Hz. However, a repetition rate of 15Hz has been employed, this is because the laser system has been tested by the supplier at this frequency, providing some important optimal triggering parameters, namely the Q-switch timings. The laser includes an attenuator that can be employed to reduce the laser power, instead of having to adjust the laser internal timings.

Laser Sheet Creation

To generate the laser sheet a two-lens set up with a cylindrical and spherical lens is used. A schematic of this system can be observed in Fig. 3.11 . The first lens expands the beam vertically and the second lens then contracts the light sheet, compensating for the first expansion and maintaining a constant sheet width. Calculating the laser sheet height in this case is straightforward, simply by using $D = \frac{f_2}{f_1}d$. In our experimental set up the lenses have a focal length of 40mm and 500mm respectively and the laser beam diameter is of 4mm, so:

$$D = \frac{500}{40} * 4mm = 50mm$$

The minimum laser sheet thickness, which is commonly referred to as the laser sheet waist, can be obtained using Eq. 3.4, however, due to space limitations the tests were performed at a region where the laser sheet thickness was of 2mm. As will be discussed in Sec. 3.2.5, this thickness is acceptable for the testing campaigns performed.

$$w = 2\frac{2.44\lambda f_2}{d} = 2\frac{2.44 * 532nm * 500mm}{4mm} = 0.325mm \tag{3.4}$$
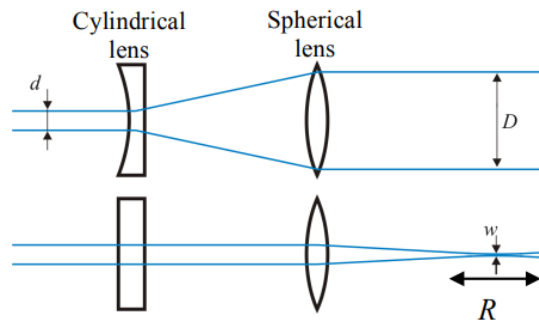
Figure 3.11: Schematic of the laser sheet generation optics. [57]

Camera

The camera employed for the experimental campaign is a Chronos 2.1-HD High Speed Monochromatic Camera (Fig. 3.12). It is unconventional to use this type of camera with a dual pulse laser system, as it does not have a double shutter feature. Therefore a customized synchronizer system was developed, as detailed in the next section.

The camera sensor chip is able to record at 1000FPS when set with the maximum resolution of 1920 x 1080. It has a pixel pitch of $10\mu m$, so the total size of the image sensor is 19.2 x 10.8mm. As will be explained later, the shutter gating triggering mode was used. In this mode an external signal fully controls the shutter, setting both the exposure time and the frame-rate.

Camera Lens

The camera lens selected for this experimental campaign was the Samyang 100mm $f_\# = 2.8$ UMC Macro Lens for Canon EF, Fig. 3.12. Some specific criteria were employed to select this camera lens. First, it has a manual ring to control the lens aperture, with a broad range from a minimum f-stop ($f_\#$) of 32 up to a maximum of 2.8. This was a key requirement, as the camera is not able to electronically control the aperture. Moreover, it has type C lens mount which is quite uncommon in photography, so it requires an adapter. Second, being a macro lens it is possible to reach a magnification of 1:1, enabling us to obtain highly magnified images close to the rough analogue surface.

Figure 3.12: Camera and Lens.

Laser & Camera Support Structure

A support structure was also designed to hold the laser unit, camera and laser lenses. This was built on a Dantec Dynamics traverse system, allowing for the simultaneous movement of both the camera, laser and lenses in three axis. This greatly simplifies the testing campaigns as the camera does not need to be re-calibrated with each movement and it always remains focused on the light sheet, see Fig. 3.13.
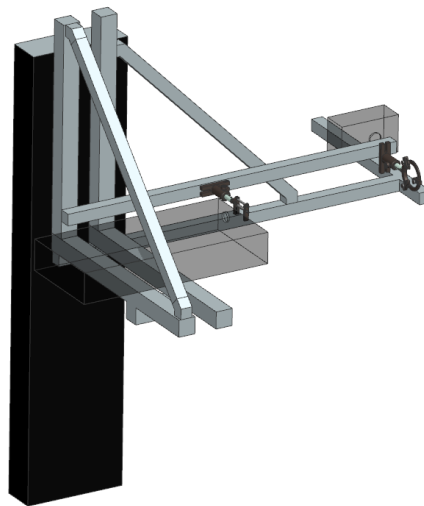
Figure 3.13: Camera and Laser support structure on the Dantec Dynamics traverse System.

Synchronizer

The simultaneous triggering of the laser and camera is controlled by a self-developed Arduino code using an Arduino Uno R4 board. The laser system is the 'master' in this process and the Arduino acts as an intermediate controller to trigger the camera. This is a 32-bit microprocessor with a clock speed of 48MHz. The code is included in Appendix B, but the basic functioning of it is explained here.

The board has several "Interrupt Digital Pins", that are set to detect a rising signal. Once this interrupt pin is triggered it will pause the execution of the code and execute the associated function to that interrupt. The first signal is the flash-lamp internal trigger of the laser-head 1. Once this signal is received, the Arduino sends a signal to the camera, which then opens the shutter. After some time the Q-switch is triggered, sending the first laser pulse. The Arduino then detects the Q-switch signal and, after a certain delay time, it stops the "shutter open" signal that the camera is receiving, closing the shutter. Intermediately after, the Arduino sends again the "shutter open" signal, keeping it open for a trivial amount of time, in the order of ms. With this a single loop has been completed, obtaining an image pair. This process is depicted in Fig. 3.14 together with a schematic of the Arduino circuitry.
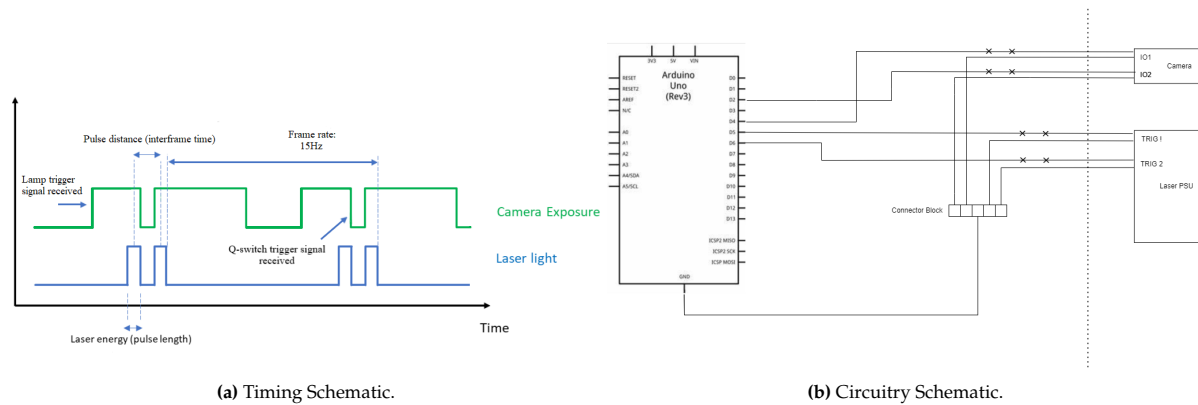
(a) Timing Schematic.

(b) Circuitry Schematic.

Figure 3.14: Arduino Synchronizer.

Opening and closing the camera shutter in this way is problematic during the camera black calibration. This black calibration is performed because the camera will automatically subtract a black reference image from all captured frames to improve the quality of the image. This calibration is unique for each resolution, frame rate, etc. so it has to be done before each testing campaign. However, it was not possible to execute the black calibration using directly the Arduino shutter opening/closing signal described previously because the camera would get stuck and never finish calibrating. The motive for this is still unknown, and the issue has not been further investigated due to time restrictions. However, the solution used to work around this was to create a simulated signal, using the same Arduino, that tries to replicate the one from the laser-Arduino system. By doing this the black calibration was completed, but with some issues. First, some horizontal lines of "locked" pixels appear on the images, as can be seen in Fig. 3.15a at the location marked with a blue arrow. Furthermore, on occasions one of the images from each image pair, either image A or B, appears to have some added white noise. This is probably because the shutter does not remain open for the same amount of time for frame A as for frame B.
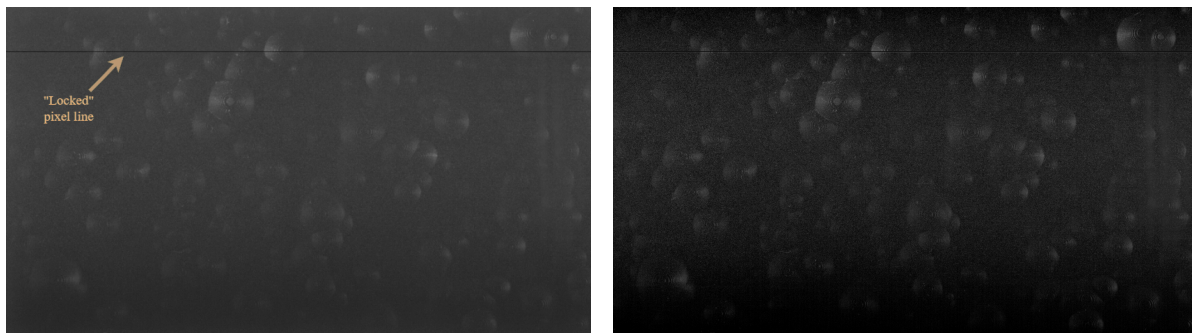
(a) Frame A depicting the line of "locked" pixels & white noise.

(b) Frame B with no white noise.

Figure 3.15: Images depicting the image quality issues after the camera black calibration (The contrast has been enhanced).

Software

As discussed, the image recording was controlled by the Arduino software and the camera settings were adjusted via the Chronos web-page. Meanwhile, the laser timings and illumination was set on the included LUCi Controller. By doing this it was possible to adjust the separation time between two images thanks to the Arduino Synchronizer.

The image post processing software used was the open source PIVlab for Matlab [73]. This employs a cross-correlation algorithm to calculate the velocity field from the PIV images. Further post processing of the velocity field data was performed mainly using Matlab.

3.2.5. PIV Settings

In this section the camera and laser settings for a given example test are described. Depending on what is the focus of the specific test the Field of View (FOV) will change. However, for most of the

experiments performed the objective is to view half of the channel width, 5cm, so we will use this value as an example. The camera is positioned so that the wall normal direction corresponds to the highest resolution side. This would result in a FOV of 5cm x 2.81cm.

A crucial parameter to ensure the quality of the measurements is the particle image size. This should be around 2-3 pixels. Since the smoke particles are very small, with an assumed mean particle diameter (d_p) of 1 μm, the effective image size will be determined by the light diffraction effect, therefore:

$$d_{eff} = \sqrt{Md_p^2 + d_{diff}^2} \tag{3.5}$$

The magnification M can be obtained by diving the image size by the object size. So for this example we have that:

$$M = \frac{SensorSize}{FOV} = \frac{1920 \cdot 1 \cdot 10^{-5}m}{5 \cdot 10^{-2}m} = 0.384 \tag{3.6}$$

The particle image size due to the diffraction effect can be calculated using Eq. 3.7. In this equation λ corresponds to the laser light wavelength. Using Eq. 3.5 the required d_{diff} to obtain an effective particle image size of 3px or 30 μm is 30 μm.

$$d_{diff} = 2.44\lambda(1 + M)f_{\#} \tag{3.7}$$

From the previous equation, it can be observed that the particle image size is controlled by adjusting the camera aperture, via the f-stop number. This results in a required $f_{\#}$ of 16.7, in general a value of 16-19 has been employed. As explained previously, the camera is placed perpendicular to the laser sheet, which is the direction in which less light is scattered by the particles. However, the particle visibility was appropriate and generally only 50% of the maximum possible laser power was required. Note that, when performing tests close to the plates, specially over the rough analogue surface, extra precautions need to be taken as the reflections from the plates could burn the camera sensor, both due to an indirect or direct reflection.

Another important factor to take into consideration is the particle displacement in between frames. This is controlled via the pulse separation time. It is typically recommended to keep the in-plane particle displacement bellow $\frac{1}{4}$ of the interrogation window size. The same applies to the out of plane movement, this should be kept bellow $\frac{1}{4}$ of the laser sheet thickness. Even though the timing is adjusted from experiment to experiment, a typical speed of 2.5m/s is selected to perform this calculation here. With this we can easily obtain the required timing as follows:

$$d_{max,in-plane} = V_{max,in-plane}dtM \rightarrow dt = \frac{d_{max,in-plane}}{V_{max,in-plane}M} = \frac{\frac{1}{4} * 16 * 10 \cdot 10^{-6}}{2.5 * 0.384} \approx 42\mu s \tag{3.8}$$

Furthermore, there is a second criterion that should be fulfilled, keeping the out-of-plane particle displacement lower than $\frac{1}{4}$ of the laser sheet thickness. Unfortunately, as this is a new wind-tunnel, no out-of-plane velocity measurements were available, therefore, as a worse case scenario, it will be assumed that the max out-of-plane velocity will be half of the bulk stream-wise component. As shown in Eq. 3.9, the out-of-plane displacement in this scenario would be of $\approx 0.1mm$, considering that the measured laser sheet thickness is of 2mm, the displacement criterion is fulfilled.

$$d_{max,out-of-plane} = V_{max,out-of-plane}dt = 0.5V_{max,in-plane} * dt = 0.5 * 2.5 * 42\mu s \approx 0.1mm \tag{3.9}$$

With these setting all the criteria are met. A summary of the PIV settings used can be found in Table 3.5. This table presents the settings obtained for the half-channel FOV, as well as an example of those used for the near-wall boundary layer measurements.

3.2.6. Image Post-Processing

As mentioned, the post processing is carried out using PIVlab. For every test 1000 images pairs are obtained and pre processed before applying the cross-correlation algorithm. First, the average background image is subtracted from the images. This eliminates possible bright spots/shadows due to reflections, improving the correlation SNR. A Contrast Limited Adaptive Histogram Equalization (CLAHE) is applied. This filter operates in a small tile and spreads out the most frequent intensities of the image. Furthermore, an intensity highpass filter is applied which removes the low frequencies of the images [72]. A comparison between a raw image and the pre-processed image can be seen in Fig. 3.16. It is clear that bright spots due to glue on the test section plexiglass have been removed and that the general visibility has been enhanced.
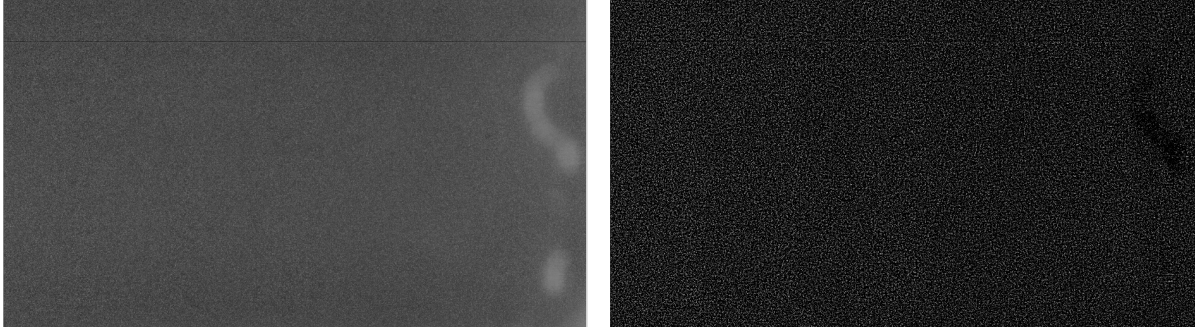
Figure 3.16: Comparison of the raw PIV images with the pre-processed image. Raw image (left), Pre-processed (right) (The contrast has been enhanced).

These images are then correlated to extract the velocity field, to do this a multi-pass cross-correlation function is applied. The first pass is set to a size of 64 x 64 pixels with an overlap of 50%. The subsequent 3 passes are kept as a square of 32, 32 and 16 pixels. To reduce computation times the Fast Fourier Transform (FFT) window deformation is used to solve the discrete cross correlation function, Eq. 3.10, where A and B correspond to the interrogation windows from the first and second image. The FFT method computes the correlation matrix in the frequency domain. The issue associated with this method is that every particle will induce some information loss, however, this can be reduced by running several passes [72].

$$C(m, n) = \sum_{i} \sum_{j} A(i, j) B(i - m, j - n) \tag{3.10}$$

Other characteristics of the PIVlab analysis algorithm won't be explained here, but can be found in the literature [72][73]. However, it is worth mentioning that as a peak finding technique a two-dimensional Gaussian function is used and that the correlation robustness method is set to "standard". Nonetheless, for the near wall rough analogue surface tests this was set to "extreme". Compared to the "standard" setting this one performs a repeated correlation, a linear cross correlation instead of circular and the window deformation scheme used is a spline method instead of a linear one. A summary of these parameters can be found in Table 3.4. This comes with a very high computation time cost, but greatly reduces the bias error, the RMS error and the number of spurious vectors [73].

Table 3.4: Correlation robustness settings in PIVlab, adapted from [73].

Correlation Robustness	Window Deformation	Cross Correlation	Repeated Correlation
"Standard"	Linear	Circular	Off
"Extreme"	Spline	Linear	On

To remove outlier vectors first some acceptable velocity limits are set by visually analyzing the 2D cloud of velocity values. Furthermore, a median and standard deviation filter is applied. These are set to the recommended values of 8 and 3 respectively, for more information refer to [72]. Finally, removed data

points are replaced by some interpolated values. PIVlab uses a boundary value solver for this purpose [72].

Table 3.5: Example of the PIV settings for different FOV.

		Half-channel	Boundary layer
Camera settings	Resolution		1920 x 1080
	Pixel Pitch	10 μm	
	Lens Focal Length	100 mm	
	FOV	5cm x 2.81cm	2.1cm x 1.2cm
	Magnification (M)	0.384	0.914
	Aperture $f_\#$	16 - 19	13 - 16
Laser Settings	Pulse Duration	4 ns	
	Wavelength	532 nm	
	Laser Sheet Thickness	2mm	
	Pulse Separation	22 - 75 μs	44 - 65 μs
Post-processing	Interrogation Window	16 x 16 px	
	Overlap	50%	
	Number of Image Pairs	1000	
	Interrogation Window [y^+]	5 - 7	2 - 3

3.2.7. Testing Campaigns

As mentioned, this is a newly built wind-tunnel, therefore, the flow quality has not been checked. For this purpose an initial testing campaign was carried out using smooth plates. Note that, in this scenario the wind-tunnel has two axis of symmetry, consequently, tests were only performed in one of the planes. It was decided to test parallel to the test-bed where the plates are positioned, and these components are described in the following section. This was done so as to avoid reflections and due to the improved camera visibility closer to the wall. The results from these tests are presented in Sec. 4.1, in the end it was concluded that the flow quality was acceptable for testing. However, features will be implemented to the tunnel to improve it in the future, like a grid mesh.

The second experimental campaign involved the testing of the rough plates, these results are presented in Sec. 4.2. These measurements were performed both in the parallel and perpendicular plane to the rough test plates. The main focus of this project was placed on the HT, therefore, most measurements were performed on the parallel plane. These were made 7.5, 15, 23 and 46 mm away from the rough plates. The initial point was the closest distance we could get next to the rough plates while avoiding dangerous reflections from the spheres. As will be explained in Section 3.2.3 & 3.2.4, the spheres have a max height of 5.7 mm and the laser sheet thickness is approx. 2mm, thus, the laser sheet could theoretically be placed at around the 7mm point. However, tests were performed slightly further away for safety and to improve the signal to noise ratio (SNR).

Boundary layer measurements will also be presented, however, these have several limitations, specially due to time restrictions. Nonetheless, the preliminary results will also be presented in Sec. 4.2.5. These measurements were performed perpendicular to the rough analogue surface and at two different locations. Only the results for one of them will be presented, corresponding to the plate center. As will be explained in that section, the results vary depending on the position where the test was performed; therefore, a more extensive testing campaign would be required.

3.3. CFD Simulations

In some previous work done as part of an internship, Computer Fluid Dynamics (CFD) was applied to simulate the fluid flow and heat transfer over the same rough surfaces using the software STAR-CCM+. These simulations replicated exactly the same test section that has been employed in this study, therefore, these have been analyzed in parallel to the PIV results.

The CFD simulations performed used RANS together with a steady state solver. The numerical methodology will not be thoroughly explained here, however, it is necessary to point out some important remarks. First, the inlet conditions tried to replicate those of the wind-tunnel, matching the values of Re, Pr and M. Furthermore, given that the Mach number is low, <0.3, and the flow can

be considered incompressible, a segregated flow solver was employed. In this way the mass and momentum conservation equations are decoupled and solved sequentially, reducing computation time.

RANS requires a turbulence closure model to be applied. Nonetheless, before choosing one, the wall treatment method needs to be selected. Due to the complex geometry and flow interactions it was decided that applying a wall model might not be appropriate. Therefore, in an attempt to resolve the wall the y^+ value was kept under 1. However, using an All y^+ treatment gave better results because the rest of the walls has a $y^+ > 1$, so this method was chosen. Finally, it was decided to use a pre-initialized Reynolds Stress Model. This is a second order closure model that adds six additional transport equations, increasing computation times, but capturing better anisotropy in the turbulence, giving a more detailed and complete representation of the turbulence.

In that work, it was necessary to simulate both the fluid an solid part of the tunnel/channel. Therefore, an interface was created between both allowing conjugate heat transfer between the fluid and solid domain. Moreover, only one analogue rough surface was simulated since the simulation was set up as repeating periodic. It was decided to do this because the interest is on a fully developed turbulent flow and setting up the simulation like this greatly reduces computation cost and time.

3.4. Data Post-Processing

In this section, the different post-processing procedures employed will be explained. First, the methods used to obtain the wall friction velocity will be depicted. Then, the position mapping and heat transfer correlation procedures will be presented. Finally, the uncertainty analysis performed is explained.

3.4.1. Wall Friction Velocity Calculations

Some of the analyses performed require the usage of the wall friction velocity (u_τ) as the velocity scale to non-dimensionalize the data. Two methods have been employed to obtain this. For the test performed with smooth wall, a value was calculated from the Moody Diagram as validation, and using the Clauser Chart Method. However, for the testing campaign with the rough analogue surfaces, only the latter was used. Both methods will be described here.

Moody Diagram

The Darcy friction factor, introduced in Eq. 2.39, can be expressed in terms of the wall shear stress as [74]:

$$f_D = \frac{8\langle\tau\rangle}{\rho\langle u\rangle_{yz}^2} \tag{3.11}$$

If we introduce in this formula the expression for the wall shear stress, then an equation for the wall friction velocity can be found, Eq. 3.12. If the Re and relative roughness is known, then the value of f_D can be extracted from the Moody Diagram, Fig. 2.15, and introduced in this expression to find an estimate of the wall friction velocity.

$$f_D = \frac{8\langle u_\tau^2 \rho\rangle}{\rho\langle u\rangle_{yz}^2} \quad \rightarrow \quad \langle u_\tau\rangle = \langle u\rangle\sqrt{\frac{f_D}{8}} \tag{3.12}$$

Clauser Chart Method

This method is an indirect technique used to determine u_τ by assuming a logarithmic law for the mean velocity profile when direct measurements of the wall shear stress are not available. Note, that this method presents many problems and can mask some complex flow behaviors [75], however, it is very widely used and will be employed in this study.

The method assumes that the velocity profile follows the universal logarithmic law of the wall, as presented in Eq. 2.24, from this equation the Clauser chart formulation can be derived. To do this we must multiply both sides by u_τ/U_∞ and express a friction coefficient similar to Darcy, $C_f = 2(\frac{u_\tau}{U_\infty})^2$:

$$\frac{U(y)}{U_\infty} = \left[\frac{1}{\kappa}\frac{u_\tau}{U_\infty}\right] ln\left(\frac{yU_\infty}{\nu}\right) + \left[\frac{1}{\kappa}\frac{u_\tau}{U_\infty}ln\left(\frac{u_\tau}{U_\infty}\right) + B\frac{u_\tau}{U_\infty}\right] \rightarrow$$

$$\frac{U(y)}{U_\infty} = \left[\frac{1}{\kappa}\sqrt{\frac{C_f}{2}}\right] ln\left(\frac{yU_\infty}{\nu}\right) + \left[\frac{1}{\kappa}\sqrt{\frac{C_f}{2}}ln\left(\sqrt{\frac{C_f}{2}}\right) + B\sqrt{\frac{C_f}{2}}\right]$$

This equation determines a family of lines for different values of C_f. In this study, a Matlab non-linear least square fit between this equation and the measured data was done to find the value of C_f and from this extract u_τ. Note, that this method is only valid in the region where $y^+ > 50$ & $y/\delta < 0.2$. The values employed for κ & B are those presented in Sec. 2.4.1.

3.4.2. Position Mapping

In order to correlate the measured velocity to the HT we need to know the position over the rough analogue surface at which we are measuring. For this purpose, when testing the analogue rough surface, in order to map the PIV rig data onto the coordinates of the 3D model, a calibration image of the spheres is taken. The camera focus is placed directly on the rough surface for this image and then it is moved perpendicularly backwards to the testing position.

The camera projection model from real 3D coordinates to 2D can be expressed as:

$$\begin{bmatrix} u \\ v \\ 1 \end{bmatrix} = \begin{bmatrix} p_{11} & p_{12} & p_{13} \\ p_{21} & p_{22} & p_{23} \\ p_{31} & p_{32} & p_{33} \end{bmatrix} \begin{bmatrix} X \\ Y \\ Z \\ 1 \end{bmatrix} \tag{3.13}$$

Where (u,v) are the image coordinates and (X,Y,Z) are the real world coordinates. This projection matrix can be factorized as P = K[R t], where K is the calibration matrix with the camera distortion information, R is the rotation matrix and t is the translation vector. The projection matrix P has twelve unknowns, however, in order to simplify the mapping process, only 2D coordinates were employed. This reduces the necessary number of reference points from 6 to 3, however, a few extra points are always selected in order to improve the accuracy of the solution.

The reference coordinates were extracted from the CAD model, see Fig. 3.17b. These same points are selected on the PIV calibration image and the coordinates are translated from pixels to physical units via the magnification factor, which was obtained previously as explained in Sec. 3.2.5. Then, the linear system of equations is solved and the projection matrix is applied to the PIV image.
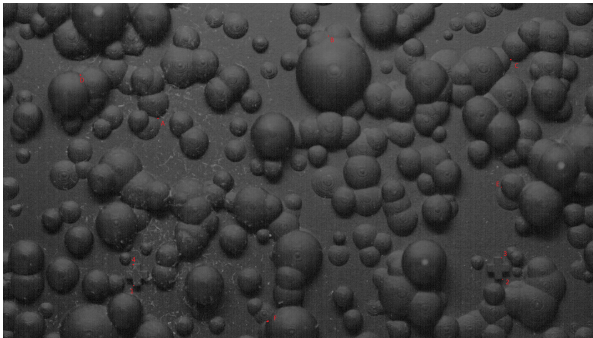
(a) PIV rough analogue surface calibration image with reference points.
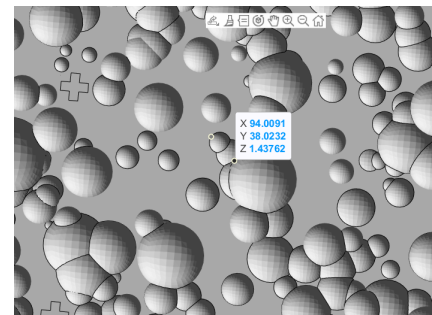
(b) Example CAD model coordinates of the analogue rough surface. (Point F)

Figure 3.17: Reference point selection for coordinates mapping.

During the selection of the reference points some important details must be taken into consideration:

- Avoid points that can not be seen by camera, like sphere overhangs.

- Avoid points that lie on shadowed parts of the PIV calibration image as the exact intersections can be hard to distinguish.
- Points must be spaced out and grouped towards the corners. These will have a higher weight when solving the linear system.

After this process the velocity values obtained are interpolated to the coordinates of the HT data [65]. It was decided to interpolate the velocity because the PIV data is distributed in a uniform grid, meanwhile, the HT data is stored in an unorganized distribution. The reason for this is because the Nu values were calculated using the in-house software *C3D* which uses a 3D mesh of the CAD model. In Fig. 4.19 the original velocity distribution from the PIV rig can be observed together with the plot of the velocity values interpolated onto the HT data coordinates.

3.4.3. HT Cross Correlations

As mentioned, one of the main goals of this research is to identify a relation between the flow behaviour and the HT enhancement. For this purpose, apart from analyzing the data and flow behaviour in a qualitative manner, some correlation coefficients will be used to try and find quantitative relations between the desired variables. Inspired by the work from S.Y Son, et al. [52], we will try to spatially correlate the mean flow and TKE fields to the Nu measured on the wall by the SRHT rig. To do this the following correlations are applied to the data, generating a 2D correlation map:

$$\left(\frac{\phi}{(\phi_{max})}\right)\left(\frac{Nu}{Nu_0}\right) \rightarrow \begin{cases} \left(\frac{\sqrt{U^2+W^2}}{(\sqrt{U^2+W^2})_{max}}\right)\left(\frac{Nu}{Nu_0}\right) \\ \left(\frac{TKE}{TKE_{max}}\right)\left(\frac{Nu}{Nu_0}\right) \end{cases} \tag{3.14}$$

In this study the value of Nu_0 will be taken as the maximum measured Nu, it was decided to do this so as to keep the correlation strength values always bellow 1, simplifying the data analysis process. As can be seen, for this correlation to return a high value the two variables must be high at the same location.

The Pearson correlation coefficient will also be calculated, this describes the linear relationship between the data. Note, that it is not expected for the data to follow a linear relationship, therefore, the result from this coefficient should be very weak. This coefficient is defined as:

$$r = \frac{\sum_{i=1}^{n}(X_{a,i} - \overline{X_a})(Y_{b,i} - \overline{Y_b})}{\left(\sum_{i=1}^{n}(X_{a,i} - \overline{X_a})^2 \sum_{j=1}^{n}(Y_{b,j} - \overline{Y_b})^2\right)^{1/2}} \tag{3.15}$$

The other coefficient that has been applied, and might be more valuable for this study, is the Spearman's rank correlation coefficient. This one measures if the variables follow a monotonically increasing or decreasing relation. If it is positive then the relation is positive monotonic, which means that as one variable increases the other one also increases, but a different rates. Its formula is:

$$r = 1 - \frac{6\sum d_i^2}{(n^3 - n)} \tag{3.16}$$

In this formula d_i represents the difference in rank between the two variables being evaluated and n is the sample size. For more information refer to the bibliography [76].

3.4.4. Uncertainty Analysis

Currently there is no accepted and reliable method to quantify the uncertainty of PIV measurements. This is due to the fact that PIV involves instruments and uncertainty sources, like laser sheet misalignment or camera settings, that are very difficult to measure. In this study two methods have been followed, first the statistical uncertainty of the measurements has been quantified, determining the precision of

the measured values or random error. Second, in an attempt to determine the accuracy of the data, the cross-correlation distribution for the interrogation windows will be analyzed as this can contain the combined effect of different error sources, determining the systematic error.

To determine the statistical uncertainty of the data we calculate the standard deviation, using Eq. 3.17, at every data point using the 1000 velocity fields obtained per test. To calculate the standard deviation of the mean we need to use Eq. 3.18, which holds if the samples are statistically independent, and calculate the overall average. For the near wall rough analogue surface measurements, which are expected to have the highest uncertainty, this results in $\sigma = 0.4994$ m/s & $\sigma_{mean} = 0.0158$ m/s. Therefore, the uncertainty on the mean velocity field is ±0.70 %. This same analysis was performed on the TKE fields which resulted in a $\sigma = 0.2994$ m/s & $\sigma_{mean} = 0.0095$ m/s. Again, this means that the expected uncertainty on the mean TKE field is of ±3.64 %. When using the "extreme" correlation robustness setting on PIVlab the percentage statistical uncertainty reduces slightly to ±0.67 % & ±3.54 % respectively.

$$\sigma = \sqrt{\frac{1}{N-1} \sum_{i=1}^{N} (x_i - \overline{x})^2} \tag{3.17}$$

$$\sigma_{mean} = \frac{1}{\sqrt{N}} \sigma \tag{3.18}$$

Using the measured velocity rms velocity error it is possible to calculate the dynamic velocity range (DVR) this defines the range of velocity variation over which measurements can be performed. At a Re = 20000 the max mean velocity for the near-wall measurements ranges up to $U_0 = 2.75$ m/s, while for the center-channel measurements it is $U_0 = 4.01$ m/s. Using the DVR definition from Adrian [77], Eq. 3.19 we obtain a DVR of 5.51 & 8.03 respectively. For the smooth wall center-channel measurements the DVR increases to ≈ 23 as $\sigma = 0.2536$ & $U_0 = 5.9$ m/s.

$$DVR = \frac{U_0}{\sigma_U} \tag{3.19}$$

It is also possible to calculate the dynamic spatial range (DSR) by using Eq. 3.20. This results in a DSR = 286 for the smooth center channel tests and 417 for the near wall measurements.

$$DSR = \frac{L_{FOV}}{\Delta_{pmax}} = \frac{L_x/M}{U_0 \Delta t} \tag{3.20}$$

Determining the magnitude of the systematic errors is a much more complex task. First, we need to determine the parameters that influence the measurement uncertainty. The flow velocity is determined from the particle image displacement and inter-pulse time ($U = \Delta x / \Delta t$). Therefore, the uncertainty on the measured velocity depends on that of these two measurements, this can be demonstrated using the error propagation formula [57] which results in:

$$\varepsilon_U = \sqrt{\left(\frac{\partial U}{\partial \Delta t} \varepsilon_{\Delta t} \right) + \left(\frac{\partial U}{\partial \Delta x} \varepsilon_{\Delta x} \right)} \tag{3.21}$$

$$\rightarrow \frac{\varepsilon_U}{U} = \sqrt{\left(\frac{\varepsilon_{\Delta t}}{\Delta t} \right)^2 + \left(\frac{\varepsilon_{\Delta x}}{\Delta x} \right)^2} \tag{3.22}$$

The uncertainty related to the Δt can be determined in a straightforwards way as it depends solely on the internal timings of the laser system. In the documentation from Dantec Dynamics it is stated that the expected laser timing jigger is <0.5 ns. The inter-pulse timings used are usually in the order of 50 μs,

this means that the expected uncertainty on the timing is of around 0.002%. Note that we need to use 2*0.5 ns as we have two laser-heads. However, this uncertainty is negligible when compared to the that from the displacement determination.

In an attempt to determine the displacement uncertainty, the source files from PIVlab were modified so as to extract the cross-correlation planes for the interrogation windows. In Fig. 3.18 an example of a CC plane with a good and bad SNR can be observed. Note that the CC is linearly scaled up and has a shift applied to it inside of PIVlab, therefore the values are in the range [0,250] instead of [-1,1]. Furthermore, the sides of the CC map are completely flat as PIVlab crops them so as to simplify programming in the software.

(a) Interrogation window with a good SNR. (b) Interrogation window with a bad SNR.
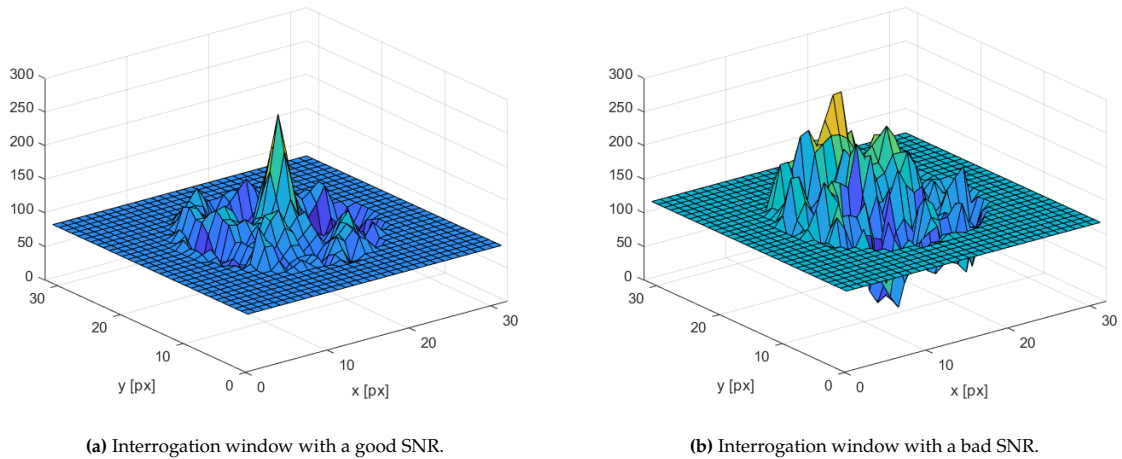
Figure 3.18: Example CC maps extracted from the near-wall testing campaign.

A way to measure the SNR is through the Primary Peak Ratio (PPR), which is the ratio of the highest peak to the second tallest one. Even though the CC is scaled in PIVlab, it was possible to extract the PPR from the original CC maps. A histogram with these values can be observed in Fig. 3.19 for the near-wall measurements and the center-channel. There are other SNR metrics that can be used, however, it was not possible to revert the scaling applied by PIVlab to the CC maps. Therefore, only the PPR has been employed. Hain and Kahler [78] state that a value of 2 can avoid spurious vectors very reliably. However, as can be observed, the PPR values achieved for this testing campaign are, in general, much lower.

(a) Near-wall test. (b) Center-channel test.
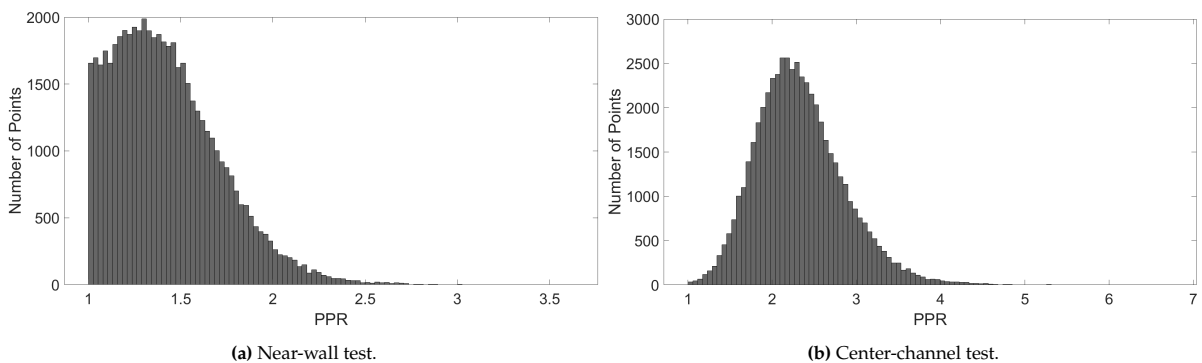
Figure 3.19: Histogram plot of PPR values obtained.

Charonko and Vlachos [79] have proposed a method to quantify the uncertainty of the measurements based on the PPR. In their work they used a phase-filtered correlation algorithm to obtain the displacements. Following their method it is possible to estimate the uncertainty if the image quality and flow conditions are know. Later, Zhenyu Xue [80] continued their line of work and applied it to other correlation methods. These are all single-pass algorithms, but the predicted uncertainty could serve as upper bound. The model they employed is that proposed by Charonko, for the PPR it takes the form:

$$u^2 = \left(Me^{-\frac{1}{2}\left(\frac{PPR-N}{s}\right)^2}\right)^2 + (A * PPR^B)^2 + (C)^2 \tag{3.23}$$

The value of N depends on the SNR quantity being used, for PPR it takes the value of 1, which corresponds to the scenario where the primary peak has the same height as the second highest one. The other parameters (M,s,A,B,C) correspond to fitting coefficients from the model. The resulting equation, for the standard cross-correlation (SSC) algorithm, after the curve fitting performed by Zhenyu Xue is presented in Eq. 3.24. The resulting curve, applied to the histogram data shown in Fig. 3.19, can be observed in Fig. 3.20. The windows of worse PPR have an uncertainty of more than 80%, these would get filtered out, while the best of 0.05%. A weighted average was performed and the resulting average uncertainty is of 8.2% for this test, for the center-channel measurements the estimate is of 4.9%. However, this is for the SSC algorithm, the multi-pass FFT algorithm which we applied is expected to have a much lower uncertainty.

$$u_{SCC}^2 = \left(10.47e^{-\frac{1}{2}\left(\frac{PPR-1}{1.12}\right)^2}\right)^2 + (1.913 * PPR^{-1.371})^2 + (2.221e - 14)^2 \tag{3.24}$$
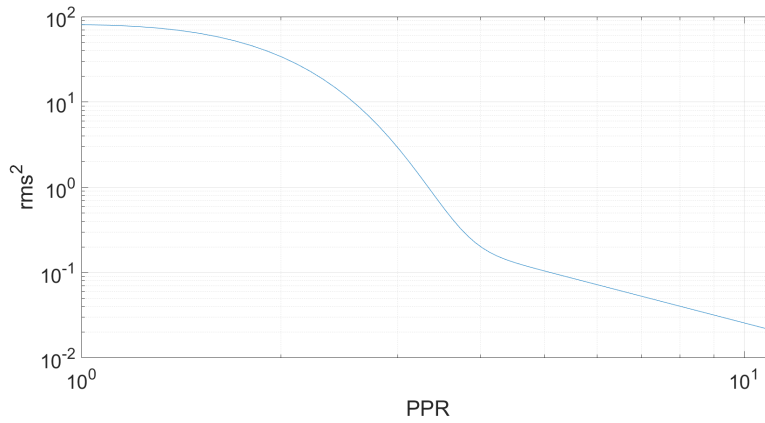
Figure 3.20: Resulting curve for uncertainty prediction from the fitting performed by Zhenyu Xue [80].

PIVlab can also output the so called "cross-correlation strength", in general, we found that having an overall value >0.5 returned good results. This is set as the lower limit to regard a test as acceptable. However, for measurements where the TKE was important it is necessary to have a higher strength. For the smooth wall tests a CCS of ≈0.8 returned good results. However, in the near-wall rough analogue surface tests a max of 0.5 was achieved, as will be discussed this was resulted in unreliable TKE measurements.

Another source of uncertainty, which is specially important for the boundary layer measurements, is the displacement gradients present in the flow field. The average shift within an interrogation window will not be the same, thus velocities tend to be overestimated, as depicted in Fig. 3.21. To reduce this bias error the spatial resolution must be high so that the velocity in the interrogation windows is almost constant.
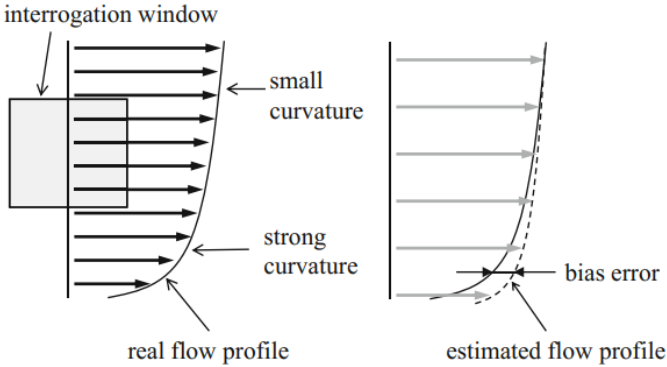
Figure 3.21: Overestimate of velocity in regions of high in-plane displacement gradients [55].

4

Results

In the following chapter, the results will be presented. First, the focus will be placed on the smooth surfaces as they served as a validation for both the wind-tunnel and the PIV set up. In the second part, the analogue Inconel 939 plates are investigated, this time placing the focus on the comparison with the HT results from W. Kaibin [65]. Furthermore, we will also contrast results with the CFD study data, trying to shine some light on the local effects that produce a HT enhancement.

4.1. Smooth Surfaces

The smooth surfaces have been tested at several different Re so as to validate the wind-tunnel's flow properties. Due to the nature of the experiments carried out, special interest has been placed on measuring the boundary layer and characterizing it. A well behaved boundary layer was crucial to ensure the validity of testing campaign with the rough plates.

First, the velocity field at the center channel position has been measured and compared to some theoretical models. Then, the near wall velocity profile was measured so as to identify the boundary layer. This was evaluated against the theoretical log-law of the wall. The Reynolds stresses were calculated and evaluated against DNS data.

4.1.1. Center-channel Velocity Field

After testing and processing the raw images following the procedure delineated in the previous chapter, a 2D velocity field is obtained. An instantaneous vector field of the center-channel velocity can be observed in Fig. 4.1. This figure shows how the velocity at the center is higher and decreases as we approach the side walls. Some non-uniformity can be observed, however, the flow is quite uniform with very little deviations. Note that, there are some spurious vectors at the bottom which correspond to a region that had some poor illumination or maybe was outside of the light sheet.

Looking at instantaneous velocity fields is very interesting, however, it is more valuable to look at overall averages and deviations. In this way it is easier to identify flow structures. In Fig. 4.2 the time averaged velocity magnitude at the center-channel position is presented. What was mentioned before about the decreasing velocity towards the sides is even more noticeable, however, it seems like the maximum velocity does not occur at the exact center of the channel ($z/\delta = 1$), this is a topic that is discussed in the Appendix D. The region with spurious velocity vectors is even more noticeable, this time it is at the top of the image as y increases downwards and the data is flipped. This region is trimmed out in the following analyses. Furthermore, at approximately $x/\delta = 0.8$ there is also a region where the velocity field is distorted, this coincides with the blocked line of pixels due to the black calibration, which was mentioned in Sec. 3.2.4 .

Analyzing these results only makes sense if they are accurate. As explained in Sec. 3.4.4, the CC coefficient which we defined previously is a direct measure of this. In this case, the CC strength (CCS) for the time averaged velocity field is 0.554, which we regarded as acceptable.
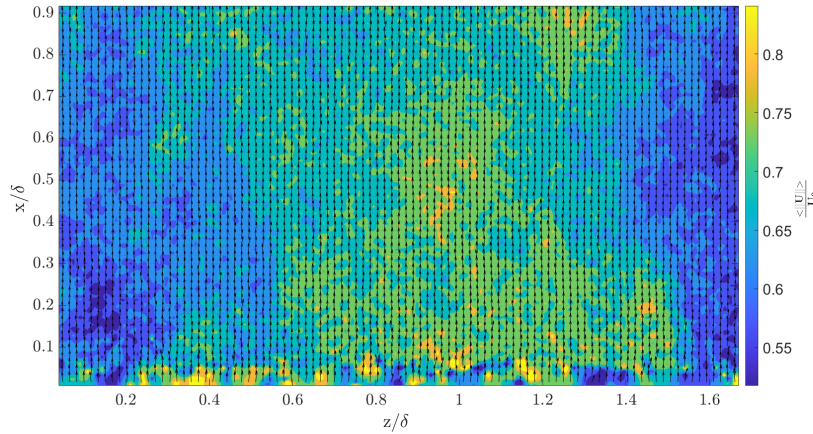
Figure 4.1: Instantaneous vector velocity field at the center-channel position with smooth walls at Re $\approx 2.86 \times 10^4$.

Figure 4.2: Time averaged velocity magnitude at the center-channel position with smooth walls at Re $\approx 2.86 \times 10^4$.

To investigate the wind-tunnel behavior, the time averaged velocity magnitude is now averaged also in the stream-wise direction, see Fig. 4.3. From this it is clear that the max velocity point is shifted to a side, and this topic is investigated in the next section.

The previous velocity profile is non-dimensionalized using the center-channel velocity, which we obtain as the maximum $\langle\langle|U|\rangle\rangle$, and compared to the Modified Power Law, which was explained in Sec. 2.4.2, the result is presented in Fig. 4.4a. It has been decided to plot only the results for half of the wind-tunnel section for clarity. Furthermore, the results are only presented for a region near the center-channel, the boundary layer will be discussed in a future section. If we compute the error as $(U_{powerlaw} - U_{measured})/U_{powerlaw}$ the result presented in Fig. 4.4b is obtained. This error is well within the uncertainty of the PIV rig and this would lead us to think that the wind-tunnel is behaving as expected, at least for this Re and at the center channel.

The center-channel turbulence intensity (TI) has also been determined, defined as:

$$TI = \frac{\sqrt{\frac{2}{3}TKE}}{\langle\langle U \rangle\rangle} \tag{4.1}$$

$$TKE = \frac{1}{2}\langle\langle u'^2 + v'^2 \rangle\rangle \tag{4.2}$$

Even though no aerodynamic coefficients will be measured in this region of the tunnel, which would

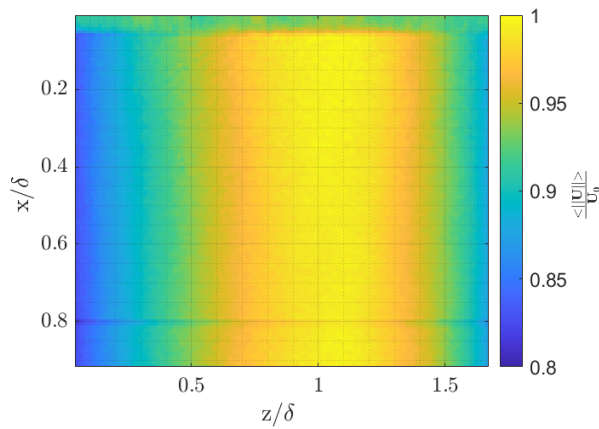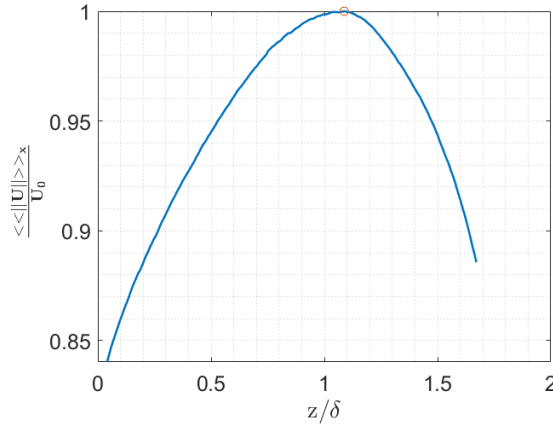**Figure 4.3:** Stream-wise & time averaged velocity magnitude at the center-channel position with smooth walls at Re $\approx 2.86 \times 10^4$.
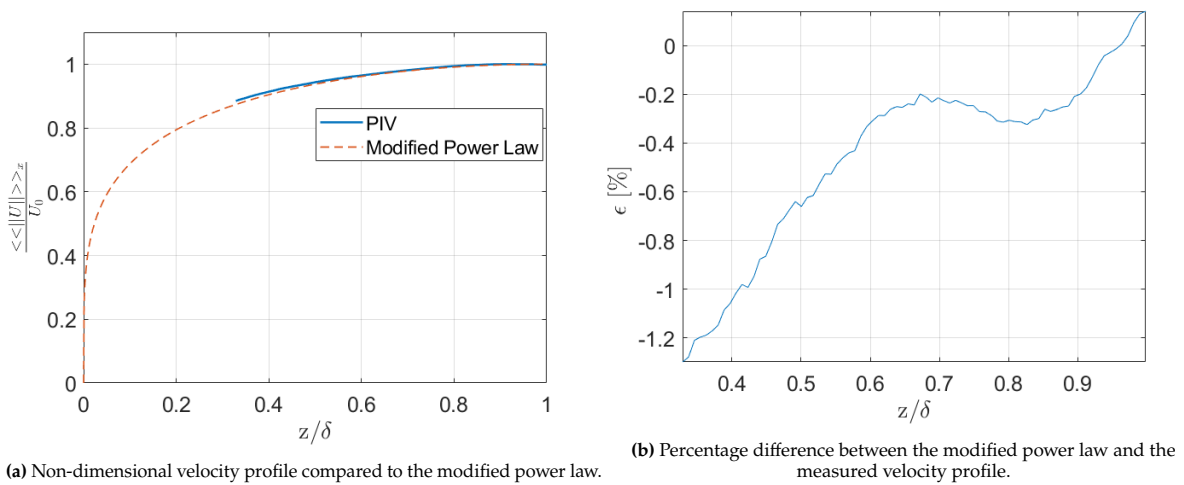
(a) Non-dimensional velocity profile compared to the modified power law.

(b) Percentage difference between the modified power law and the measured velocity profile.

Figure 4.4: Comparison of measured channel velocity profile with the modified power law.

require a very low TI, it is important to keep these values at an acceptable range to ensure that the results are not altered by this. However, to measure the TI it is necessary to have a very high CCS and SNR to make sure that most of the contribution to the turbulence measurement is from real turbulence and not noise contamination from the PIV measurements. For this purpose, the magnification was increased to 1.1, which is close to the maximum possible magnification of 1, this results in a FOV of ≈ 21mm. By doing this, the CCS increased to a value of over 0.8 for the two measurements taken, 0.813 and 0.847. These were taken at a Re of $\approx 2.91 \times 10^4$ and 1.41×10^4, yielding a TI of 2.452 % and 2.99% respectively.

In [81] a "core" region that has a high and uniform velocity was determined and studied. They found that this region has a low turbulence level, of less than 3.8%, which is in agreement with the measurements made here. They determined this core region with isocontour lines of $0.95 \cdot U_0$. For the mean measurements presented here this would correspond to approximately $x/\delta > 0.5$, therefore, the data presented in Fig. 4.4a and the average data taken for the TI measurements would fit in this "core" region. Furthermore, in [82] a value of 3.7% is taken as their reference turbulence intensity. In this study they found that the increase in centerline TI did not affect the wall log region. Moreover, the measured value is in the range of 1-5% TI stated for internal flows in other sources [83]. From this it can be concluded that the TI level present in the wind-tunnel is aligned with what is to be expected from a fully developed turbulent pipe flow and should be appropriate for the purpose of this project: replicating an internal pipe flow. However, the TI level is far from the 0.1% value of low turbulence wind-tunnels that try to replicate background TI for aerodynamic measurements.

4.1.2. Boundary Layer Measurements

As aforementioned, the second testing campaign involved performing experiments perpendicular and close to the wind-tunnel walls in an attempt to make boundary layer measurements. The stream-wise & time averaged velocity magnitude is presented in Fig. 4.5. In this figure it is clear that the measured boundary layer profile differs slightly from that of the modified power law. We will discuss this further bellow.
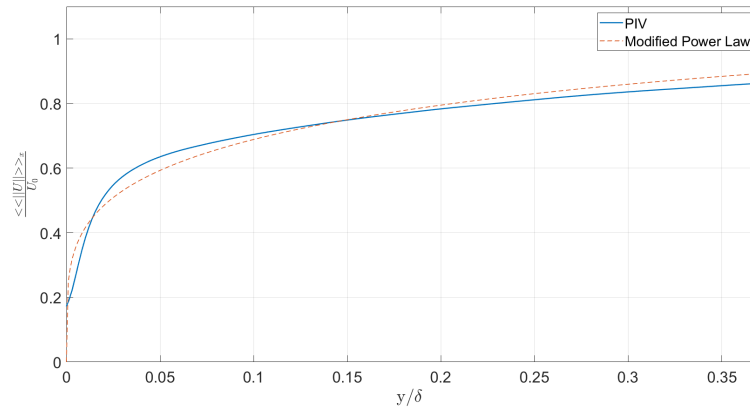

Figure 4.5: Near wall non-dimensional velocity profile compared to the Modified Power Law for Re 2.91×10^4.

The measured data was non-dimensionalized and plotted against the logarithmic law of the wall, which was discussed in Sec. 2.4.1. Until now, no measured value of u_τ was available. However, as we are testing a fully smooth channel, it is possible to extract this from the Moody diagram as an initial estimate by using the expression presented in Sec. 3.4.1, Eq 3.12. The result is shown in Fig. 4.6a. As can be observed, the data follows the log law but with a slight shift upwards. This could mean that the calculated u_τ is lower than the real value. The main culprit for this is probably the differential pressure measurement from which the volume flow is obtained, which tends to oscillate, making the task of taking volume flow measurements difficult. Nonetheless, the values are still within the uncertainty of the rig.

It can also be observed that the measurements made in the viscous sub-region, $y^+ < 5$ do not follow exactly $u^+ = y^+$, even if the data approaches this theoretical curve. This can be due to a variety of reasons, but the most likely is the reflected light from the wall. In fact, it was discovered that the plexiglass wall generated a reflected light-sheet. This will have a negative effect on the data, but again, due to time limitations, the testing plan continued. Another possible explanation is that, as the wall is approached, the velocity decreases very fast, therefore the apparent movement of particles in the image pairs is very small. This would lead to incorrect displacement measurements, this is confirmed by the very low CC strength in the region, which was lower than 0.4. Furthermore, the spatial resolution of the measurements might not be enough to fully capture this behaviour.

The Clauser Chart method, as depicted in Sec. 3.4.1, was also employed to obtain the friction velocity u_τ. The value obtained from this method was indeed slightly higher than that extracted from the Moody Diagram, see Table 4.1. When applying this value to normalize the data Fig. 4.6b was obtained. As can be observed, the data follows even more closely the log law. Moreover, the difference between the two methods is within the rig uncertainty, which would prove this as a valid method for future analysis, at least for smooth surfaces.

The measurements made at various Re are presented in Fig. 4.7, they all follow accurately the log-law. These results are a clear indicative that the boundary layer is behaving as expected, contrary to what we saw when comparing to the modified power law. Additionally, it can also be observed that at a lower Re the non-dimensional spatial resolution increases and the curve converges towards the theoretical profile of the viscous region.

As demonstrated, the boundary layer measurements follow the non-dimensional log law, but not the modified power law. To investigate this, the calculated u_τ was used to undo the non-dimensionalization
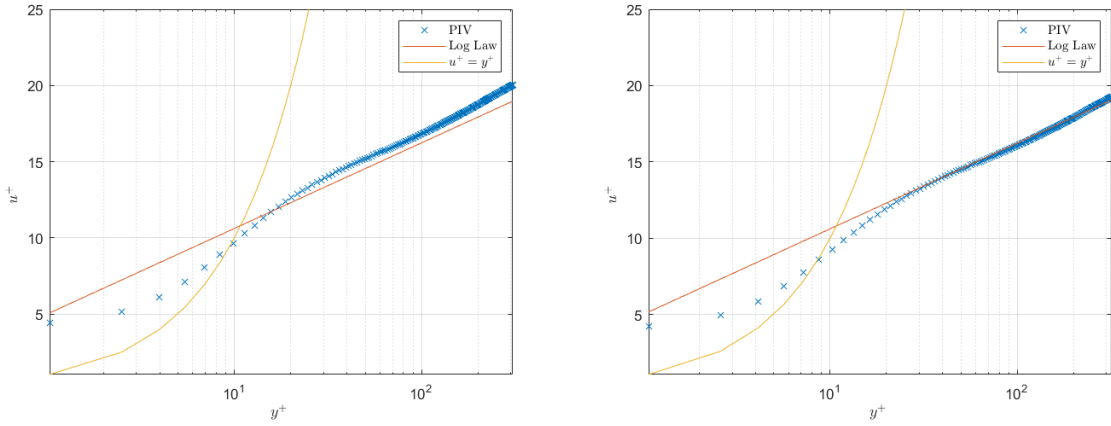
(a) Variables non-dimensionalized using the theoretical u_τ from the Moody diagram.

(b) Variables non-dimensionalized using the u_τ obtained from applying the Clauser Chart Method.

Figure 4.6: Log law plots at Re 2.91×10^4 with smooth walls.
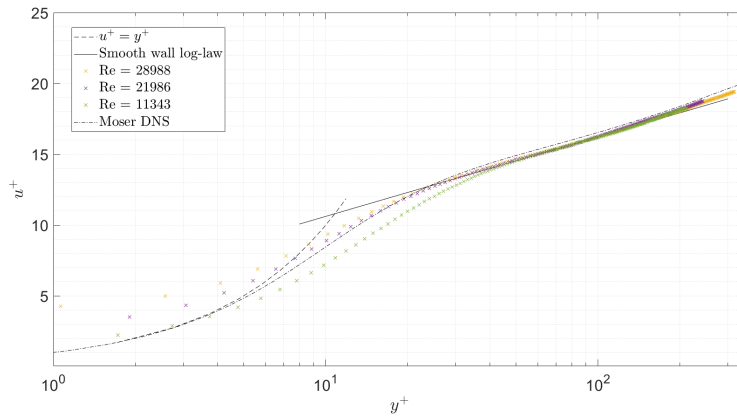
Figure 4.7: Non-dimensional velocity profile using the u_τ obtained applying the Clauser chart method for different values of Re.

of the log law. This was plotted in Fig. 4.8 against the modified power law and the measured data. From this it is obvious that the modified power law does not align with the other velocity profiles. As the spatial resolution of these measurements was high, less than 5 wall units, a bias error related to the displacement gradients is discarded. Therefore, the difference is attributed to the fact that this law was optimized for a round pipe, not a square channel. For this reason, any further comparisons in this region should be made with caution.

As explained in Sec. 2.4.3, the defect law describes a universal scaling behaviour of the outer flow region. The data was processed and plotted against this theoretical line, Fig. 4.9. Note, that here the center-channel velocity was extracted from the measurements made in the previous testing campaign, where the center-channel velocity was measured. This explains why the lines do not coincide exactly with the theoretical, we were unable to match exactly the same Re in both tests. The friction velocity value used for scaling was that obtained from the Clauser Chart Method. It is clear that the measured velocity profile follows this universal scaling, which is another indicative that the flow is well behaved.

Finally, the Reynolds stresses, defined in Appendix A, are computed and compared to the DNS data from Moser [84]. To characterize boundary layer data the Re_τ value is typically used, this is defined as $Re_\tau = \frac{u_\tau L}{\nu}$. This is important because the DNS data used here is for a Re_τ of 587, while the data presented from this test is for $Re_\tau = 864$. This data was employed as no other was found with a closer Re_τ value. The resulting plot can be seen in Fig. 4.10a. Moreover, a test at a lower and closer value of $Re_\tau = 574$ was performed, Fig. 4.10b. In both cases the $u'v'$ & $v'v'$ components follow closely the

Table 4.1: Friction velocity u_τ with fully smooth walls as extracted from the Moody Diagram and using the Clauser Chart method.

Re	u_τ **Moody**	u_τ **Clauser**	**% difference**
$\approx 2.9 \times 10^4$	0.24972	0.25966	-3.828
$\approx 2.1 \times 10^4$	0.19055	0.19915	-4.318
$\approx 1.4 \times 10^4$	0.17248	0.17256	-0.046
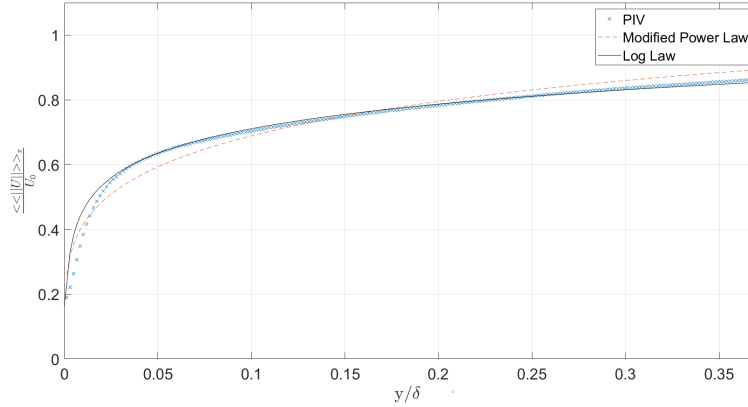
Figure 4.8: Near wall non-dimensional velocity profile compared to the modified power law & log-law for Re 2.91×10^4.

DNS data, however, for $u'u'$ there are slight differences. Nonetheless, these are very small, for example, the difference in peak position in Fig. 4.10b corresponds to 8 wall y^+ units, which corresponds to a miss-positioning of less than 0.5mm. The calibration for positioning was done using a ruler, the smallest scale division of which was 0.5mm, which could be responsible for this shift.

From all these analyses it has been demonstrated that the flow follows the expected universal scaling laws. This indicates that it is well behaved and testing can proceed without the installation of flow conditioning devices in the wind-tunnel. Furthermore, the validity of the PIV testing rig has been demonstrated.

4.2. Rough Surface

The rough surfaces have also been tested at several different Reynolds numbers. However, focus will be placed on the results at a Re of $\approx 2.00 \times 10^4$ as the available CFD and HT data was obtained at this Re. The main priority has been making measurements parallel to the rough analogue surface so as to correlate the velocity field to the local heat transfer. However, some boundary layer measurements were also made and will be briefly discussed.

As with the smooth plates, first the velocity field at the center channel position has been measured so as to identify the effect of the roughness on the central "core" region of the channel. Next, the velocity field was measured as close as possible and parallel to the rough analogue surface. The measured velocity field was then correlated to the local Nu on the wall and compared to the CFD simulations data. Finally, the boundary layer measurements performed perpendicular to the rough plate are presented.

4.2.1. Center-channel Velocity Field

The instantaneous vector field of the center-channel velocity can be observed in Fig. 4.11. Note that, as in the previous image presented for the smooth wall test in Fig. 4.1, the bottom part has some spurious vectors that correspond to a poorly illuminated region and that the filtering & interpolation process in PIVlab did not remove. Compared to those results not much difference can be observed. This is to be expected, we are far away from the roughness sublayer, defined in Sec. 2.5.1, and thus the effect of the roughness on the flow has been dissipated [9].

As in the previous section, we will focus on the mean velocity fields and profiles. In Fig. 4.12 the center-channel velocity profile is non-dimensionalized and compared to the modified power law. At
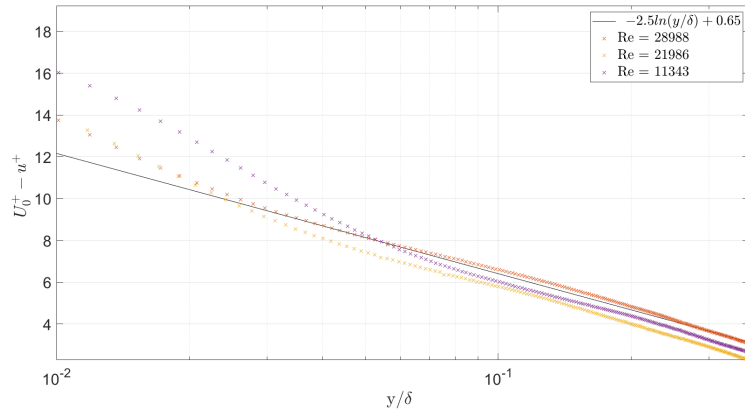
Figure 4.9: Defect law plot at $\approx 2.91 \times 10^4$ with smooth walls.

(a) $Re_\tau = 864$.

(b) $Re_\tau = 574$.
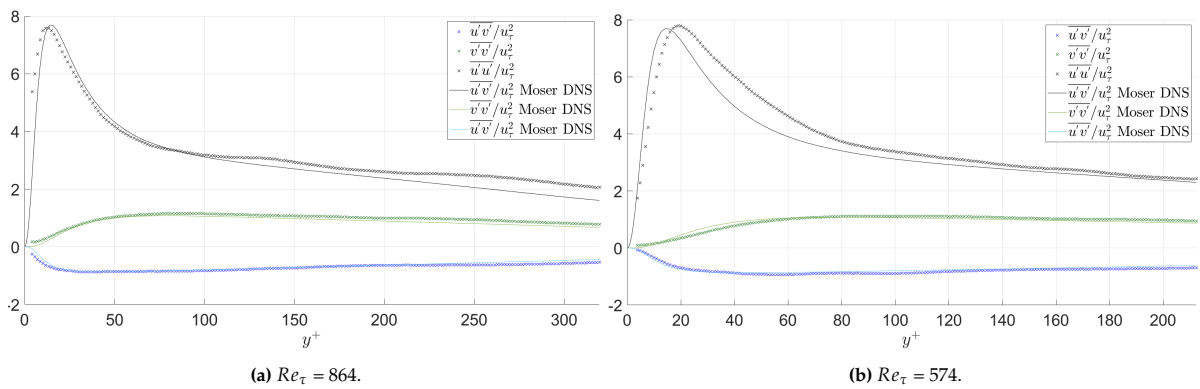
Figure 4.10: Profiles of Reynolds normal and shear stresses for smooth wall.

first glance no notable difference can be seen with respect to the smooth plates results, the velocity at the center is quite uniform and deviates at the sides. Furthermore, the symmetry problem persists. In this test we measured $U_0 = 4.01$ m/s at a channel position of $z/\delta = 1.17$. This value fits perfectly on the curve fitting performed in Fig. D.1, where the predicted center position would be 1.2 for this U_0, thus the roughness did not influence this issue.
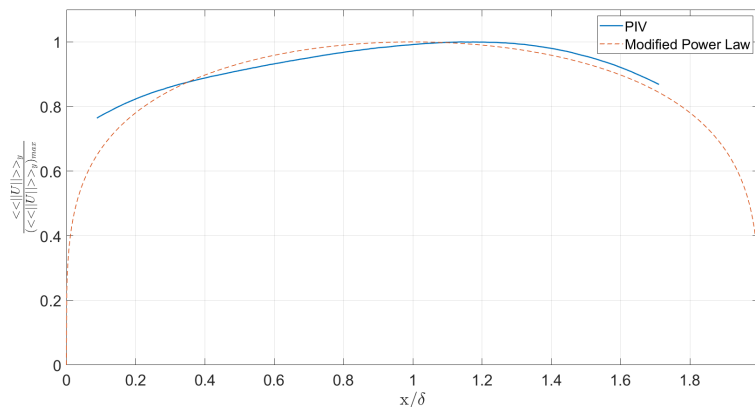
Figure 4.12: Stream-wise & time averaged $||U||$ at the center-channel position with rough analogue surface at Re $\approx 2.00 \times 10^4$.

As for the smooth plates, the mean center-channel TI has been determined. For this calculation the
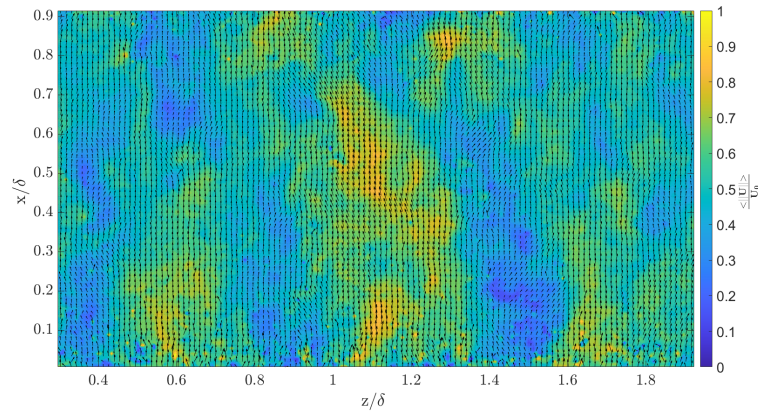
Figure 4.11: Instantaneous vector velocity field at the center-channel position with rough analogue plate at Re 1.99×10^4.

edges of the FOV have been trimmed as these had a low CCS, increasing in this way the average value to over 0.5, which was regarded as acceptable in Sec. 3.4.4. In the end a value of 6.43% TI was obtained, which is more than double the value obtained for the smooth wall measurements, so it is clear that the turbulence generated by the rough wall has not been fully dissipated yet.

4.2.2. Near-wall Velocity Field

In an attempt to visualize the local effect from the artificial roughness, measurements were made as close as possible to the wall, which turned out to be 7.5mm away from the rough analogue surface, as explained in Sec. 3.2.7. The time averaged velocity field can be observed in Fig. 4.13. Here several notable differences can be seen with respect to the center-channel measurements. It is clear that streaks have formed near the wall and the velocity field is no longer uniform. Furthermore, some interesting structures are forming. For example, at the position $z/\delta \approx 1.1$ & $x/\delta \approx 0.4$ the velocity field has a horseshoe like shape and at the region close to $x/\delta = 0.8$ & $z/\delta \approx 0.5$ the velocity deficit is very notable.

Figure 4.13: Time averaged velocity magnitude at the near wall position with rough analogue surface at a Re $\approx 2.00 \times 10^4$.

This may be related to the roughness elements present, so to investigate it the velocity field was mapped onto the 3D CAD model using the procedure explained in Sec. 3.4.2. An isometric and top view of the 3D plot can be observed in Fig. 4.14a & Fig. 4.14b respectively. From the latter is it clear that the horseshoe shape is forming due to the disruption produced by the sphere at x=60mm & y=50mm, whose height is of 5.39mm, being close to the measured R_z of 5.741mm presented in Table 3.3. On the other hand, the zone with a velocity deficit, mentioned previously, is over a region after a big cluster of spheres and where there are only a few spheres which are very small.

In Fig. 4.15 the time & stream-wise averaged velocity magnitude can be observed. Here the two high &

(a) Isometric view.

(b) Top view.
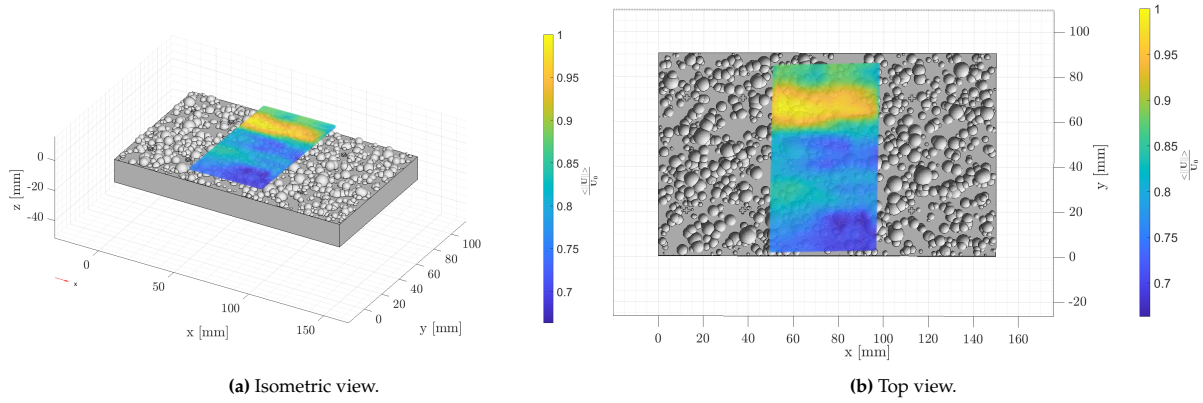
Figure 4.14: Measured velocity field near the wall at a Re $\approx 2.00 \times 10^4$ over the rough analogue surface model.

low speed streaks can be clearly identified. The difference in the velocities are quite substantial, the percentage increase in velocity from the leftmost peak to the center-channel position is of around 30%. In other studies [85] the existence of large-scale secondary motions induced by stream-wise roughness was identified. However, in this study they found these only appeared on the heterogeneous roughness, not on the homogeneous random case. In a future study it should be investigated wether or not these streaks form due to the roughness being "periodic".
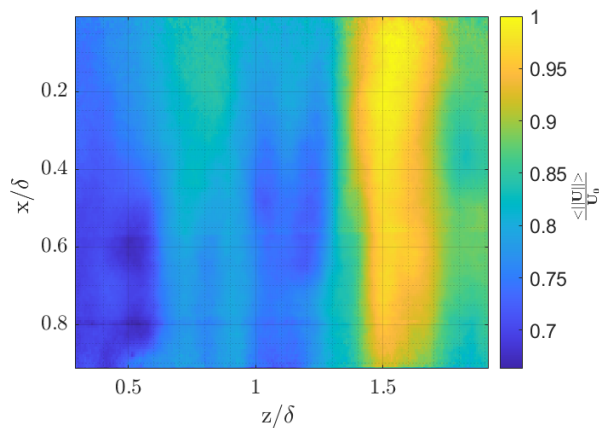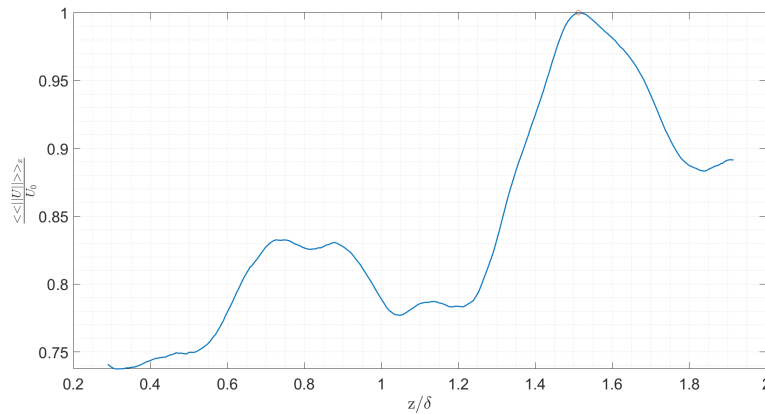

Figure 4.15: Stream-wise & time averaged velocity magnitude at the near-wall position with the rough analogue surface at Re $\approx$ $\approx 2.00 \times 10^4$.

Tests were performed at different distances from the rough analogue surface in order to study the evolution of the velocity profile and TKE. In Fig. 4.16 it can be observed that close to the wall the effect of the spheres on the velocity profile is strong and this diminishes with the distance, approaching the theoretical profile for a smooth channel at the center-channel position. This is in line with what is to be expected, with the distance the turbulence and turbulent structures generated by the spheres have had time to dissipate. In the literature [9] it is stated that the roughness sublayer for some cases can extend up to $5 \cdot k_s$, using R_z as the equivalent sand-grain roughness height this would mean that the outer limit corresponds to $\approx 17mm - 29mm$. As a matter of fact, it is in this region where the individual peaks are almost non-identifiable since the effect of the spheres has dissipated.

When performing this same analysis on the overall TKE its gradual decrease with distance from the rough analogue surface is clear, Fig. 4.17. This is to be expected, close to the roughness their inertial effects, like flow detachment, will have a big influence. Near the wall the measured TI was much higher, of 19.4% compared to a value of 6.43% at the center-channel position. However, the results from the near wall measurements must be analyzed carefully, this is because the CCS achieved for the test closest to the wall was only of 0.407. The main reason for this low CCS achieved is mainly due to the reflected
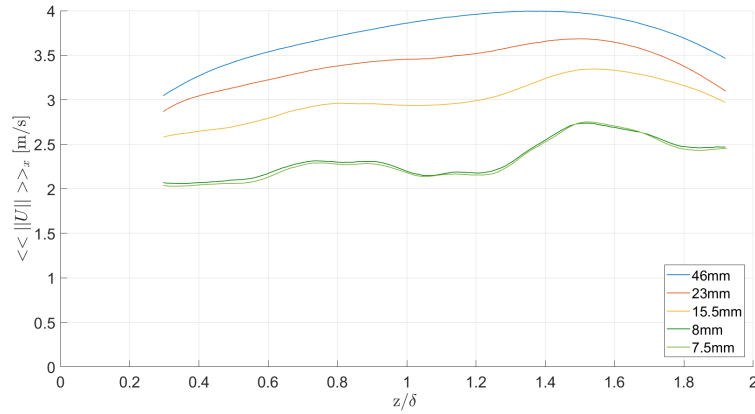
Figure 4.16: Evolution of the velocity profile with distance from the rough analogue surface at a Re $\approx 2.00 \times 10^4$.

light off the plate. To try and solve this issue the 'Correlation Quality' parameter on the PIVlab settings was set to 'Extreme', to see the effect of this parameter refer to Sec. 3.2.6. This reduces the bias error for the data, which presented less spurious vectors. As a result, there was a slight decrease in the TKE level measured, and this can be attributed to measuring uncertainty.
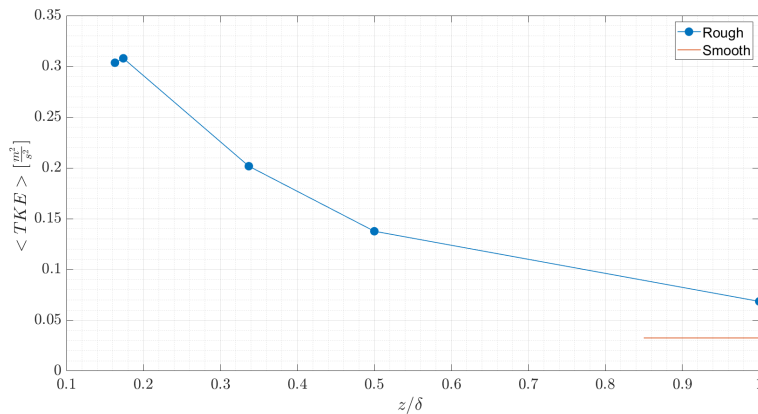
Figure 4.17: Evolution of the TKE with distance from the rough analogue surface at a Re $\approx$ 20K.

4.2.3. Cross Correlation with Heat Transfer

The main purpose of this project is to investigate the main drives of HT in channels that present very high surface roughness, which will be addressed in this section. In Fig. 4.18 the local Nu values obtained by W. Kaibin [65] are presented. Note that, in the next figures the PIV data will be rotated so that flow goes from right to left, decreasing x coordinate, so as to match the stream-wise direction used by W. Kaibin. It is important to recall here that the same test section geometry was used, however, the flow conditions on the PIV rig are slightly different, as mentioned in Sec. 3.2.1. Furthermore, the FOV from the PIV measurements is smaller than the interest region measured by the SRHT-rig, the black dashed line on Fig. 4.18 depicts this.

Inspired by the work done by S.Y. Son, et al. [52], the correlation they introduced was applied to the mean velocity and TKE, as shown in Eq. 3.14, together with other cross-correlations. To do this, first the measured PIV velocity components had to be interpolated onto the same points as the HT data following the procedure explained in Sec. 3.4.2. Fig. 4.19 shows an example of the interpolated near wall velocity together with the original PIV data and the similarity between the two validates the interpolation process.

Following this, the correlation is applied to both the velocity magnitude and the TKE. The resulting
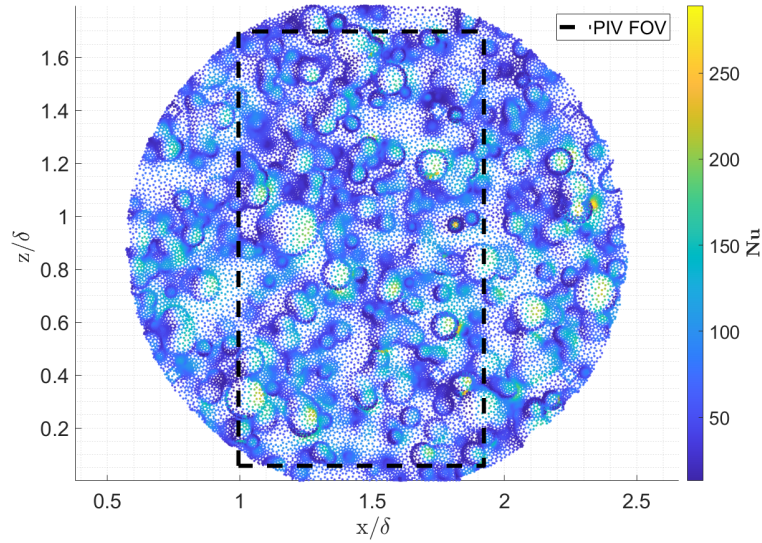
Figure 4.18: Scatter plot of the Nu values measured by W. Kaibin [65] and the PIV FOV.

correlation distributions can be observed in Fig. 4.20. From these it is clear that the mean flow-heat transfer correlation (Fig. 4.20a) shows a much higher level of correlation than the TKE-heat transfer. Nonetheless, these results must be interpreted carefully, this is because the TKE energy is still highly contaminated by the uncertainty from the PIV measurements even after trimming the edges. For this reason, looking at the CFD data will be very valuable, therefore, these results will be analyzed together with the CFD in the next section.

4.2.4. PIV & CFD

The PIV data obtained for this specific case has been compared to that extracted from the CFD simulation. This presents the same problems as the data from the SRHT rig, the Re is equal, but Pr is different, since this one on the CFD is matched to that of the SRHT rig. Moreover, the CFD simulation domain is slightly smaller than the PIV test section. This is because the simulation was performed for only the rough analogue surface plate, without including the sides of the mounting test-bed from the test section that was designed for this study. This means that the CFD domain is about 10mm smaller in the z (span-wise) direction. For these reasons, it has been decided that the CFD data will be compared to the PIV using normalized values.

The mean velocity field extracted from the PIV and CFD look very similar, at both the near wall (y/δ = 0.15) & center-channel measurement plane (y/δ = 1), as shown in Fig. 4.21. Nonetheless, some differences can be observed, specially on the left half of the channel ($z/\delta < 1$). At the near wall plane the peaks at $z/\delta \approx 1.3$, corresponding to the high speed streak, look very similar in shape. However, for the other high speed region the overall velocity level is lower and the peaks are less pronounced on the PIV data. An explanation for this could be that the flow in the wind-tunnel is not fully developed yet, as discussed in Appendix D. For example, in Fig. D.2 it can be observed how these peaks become more marked as we move downstream. Maybe if the flow was allowed to reach the fully developed state then these would approach the CFD measurements. Furthermore, the center-channel measurements, presented in Fig. 4.21b, show that the CFD follows the modified power law very closely, nonetheless this is not true for the left side of the wind-tunnel. This could be attributed to the symmetry problem of the wind-tunnel, so it should be investigated in the future once that has been solved.

As with the PIV results, the correlation from Eq. 3.14, was applied to the velocity magnitude and TKE, and the correlation maps are shown in Fig. 4.22a & 4.22b respectively. The mean flow-heat transfer correlation map is very similar to that from the PIV data, Fig. 4.20a, but with a more intense correlation at certain spots, like the sphere at $z/\delta \approx 1m$ & $x/\delta \approx 1.2m$. However, the TKE-heat transfer correlation map looks very different from that presented in Fig. 4.20b. The overall correlation level is much higher

(a) Original PIV data.

(b) Interpolated PIV data.
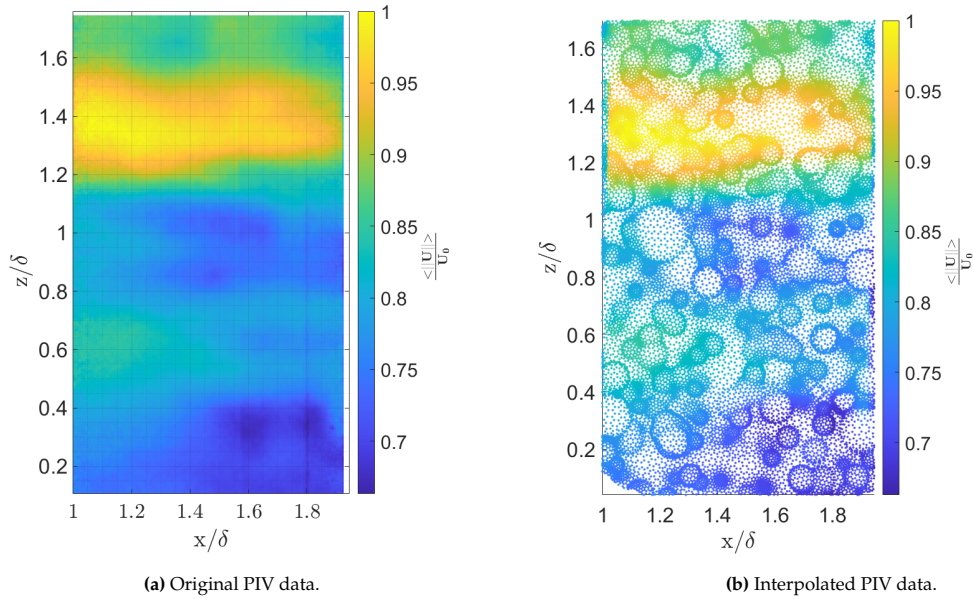
Figure 4.19: Original velocity distribution from PIV rig measurements and interpolated distribution onto HT data points.

for the CFD data and the spots of intense CC on the spheres are much more intense.

This is also clear by looking at the overall correlation level, presented in Table 4.2. The correlation on the velocity from the CFD with respect to the PIV is only about 10% higher, however, on the TKE it is more than double. We believe that the reason for this is because the data is still highly influenced by spurious velocity measurements, this is because the regions of highest TKE coincide with the regions of lowest CCS on the PIV algorithm. This could mean that the actual effect of the TKE is hidden by the noise from the PIV measuring/post-processing methodology, which increases the max TKE, and decreases the overall TKE-heat correlation.

Table 4.2: Averaged velocity-heat & TKE-heat correlation strength for PIV and CFD data at a $Re \approx 2.00 \times 10^4$.

	PIV	CFD	% difference
Velocity	0.1813	0.1993	-9.9
TKE	0.0814	0.1652	-102.9
% difference	55.1	17.1	

To try to understand better the magnitude of the influence that both the mean velocity and TKE have on the HT, the regions of high velocity and TKE were divided and plotted on a contour map superimposed over the local Nu map, Fig 4.23. Note, that due to the problems mentioned previously with the calculated TKE from the PIV data it was decided to only do this with the CFD data.

The high velocity regions are considered to be those where the velocity is >90% of the max velocity. Meanwhile, for the high TKE they are those with >80% of the max TKE. Looking at the plot it is clear that the regions of high TKE correspond to those with lower speed, something that is to be expected. Nonetheless, it is still unclear by looking at this image if the higher TKE or velocity raise the overall HT locally. In an attempt to investigate this, the zonal Nu values for these regions have been obtained, these can be seen in Table 4.3.

Table 4.3: Comparison of the average Nu, U and TKE on the regions of high speed and high TKE.

Parameter / Region	High Velocity	High TKE	Rest
<Nu>	65.8574	71.2032	63.6975
<U>	3.4068	3.1024	3.0666
<TKE>	0.4887	0.5857	0.4692
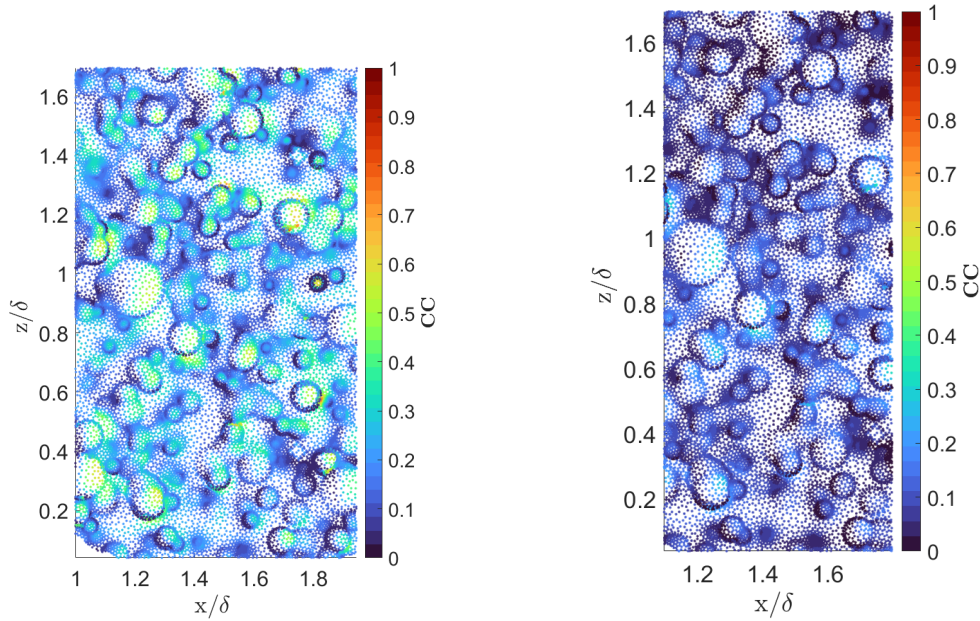
(a) Correlation distribution between mean velocity magnitude and Nu.

(b) Correlation distribution between TKE and Nu.

Figure 4.20: Correlation distributions for near wall PIV measurements at a Re $\approx 2.00 \times 10^4$.

From these it is clear that the regions of high velocity have an overall Nu very similar to the low velocity & TKE regions. Even though the velocity in the latter is 10% lower, the Nu is only 3.3% lower. However, if we compare the high TKE regions with the rest the overall Nu is almost 12% higher but with a very similar average velocity. Furthermore, the regions of high TKE that can be observed in Fig. 4.23 coincide with the wake regions of bigger spheres. Therefore, it may be concluded that the increase in TKE in the wake region of spheres enhances the HT on the spheres there. This would mean that a considerable part of the HT enhancement presented by this type of roughness could be attributed to the turbulence increase.

This is opposite to what we had seen in the previous analysis from the correlation maps. The explanation behind this might not be trivial, but looking at the zonal averaged parameters presented in Table 4.3 can explain it. From how Eq. 3.14 is formulated the term corresponding to heat will always be the same, it is the other side that changes. However, as we have seen, the variations on the average velocity are very small when compared to the variations on average TKE, therefore if we compute a mean value the result will inherently be that:

$$\left\langle \left(\frac{\sqrt{U^2 + W^2}}{(\sqrt{U^2 + W^2})_{max}} \right) \right\rangle \qquad > \qquad \left\langle \left(\frac{TKE}{TKE_{max}} \right) \right\rangle$$

The underlying motive for this is that at this distance from the rough analogue surface we are able to identify mean flow effects from the spheres, like wake regions and high speed streaks. However, we are not able to measure localized effects on the spheres, like impingement zones, re-circulation areas, reattachment points, etc., contrary to the analysis carried out by S.Y Son, et al. [52].

To visualize better these effects the velocity field at a perpendicular plane to the rough analogue surface, at the position z = 0.5*δ was extracted from the CFD and plotted together with the experimentally measured Nu along the wall, the resulting graph is presented in Fig. 4.24. From this graph the impingement points can be intuited, however, looking at a zoom in image, Fig. 4.25, the local effects are much clearer. For example, the peak at x/δ = 1.24, clearly corresponds to the impingement point on the big sphere located there. However, the peat at x/δ = 0.64 does not seem to be due to impingement,
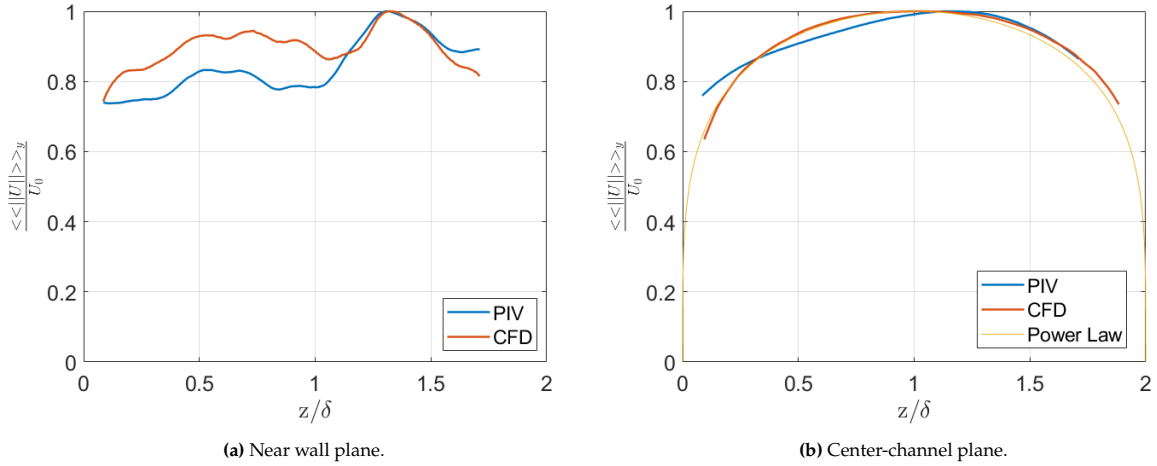
(a) Near wall plane.   (b) Center-channel plane.

Figure 4.21: Non-dimensional velocity profiles from PIV & CFD data at a Re $\approx 2.00 \times 10^4$.

but due to the flow reattachment occurring after the re-circulation area formed in between the two spheres. The effect of flow detachment from the spheres, and re-circulation, is very clear after the first and second sphere, from left to right. Furthermore, the region from $x/\delta = 0.94$ to $x/\delta = 1.10$ seems to have a lower Nu due to the "shielding" effect that the second sphere has. Moreover, something interesting is happening at $x/\delta = 0.88$, there is a peak at a re-circulation region. This may be because the air being deflected downwards by the sphere immediately behind is creating an impingement zone on the flat surface, but this can not be identified with this 2D plot. Moreover, in [51] they found that the adverse pressure gradient does not affect the heat transfer as it does the momentum and maybe other heat transfer mechanisms might be involved that could explain this unintuitive behaviour.

To further emphasize the importance of the boundary layer "reset" at the windward-facing impingement zones and to illustrate the previously made points, the correlation was applied to the wall-shear stress extracted from the CFD. In Fig. 4.26, the resulting τ_w-heat transfer correlation map can be observed. The trend is evident, the points of highest CC are the windward-facing part of the spheres. However, the CC is very weak in the rest of zones, resulting in an overall mean of only 0.0262. Applying this same CC using the local Nu extracted from the CFD (so far, only SRHT data has been used), the observed pattern persists.

Nonetheless, the overall correlation with CFD is lower than with the experiments. The reason for this is that the local Nu range on the CFD is much wider. The maximum local Nu being 588 while on the experimental data it is 289. This difference is clear when looking at the local Nu enhancement, defined as Nu/Nu_{DB}, and presented in Fig. 4.27. In the CFD, almost all of the HT enhancement can be attributed to the impingement points, explaining the high τ_w-heat transfer correlation coefficients obtained. However, the SRHT data shows that the HT enhancement is not as pronounced on the impingement points, but it is higher overall on the flat zones of the rough analogue surface. From this it can be concluded that, while the impingement points are one of the main contributors to HT, there are other effects in play that are not captured by the RANS simulations. However, it seems like the model has a lot of re-circulation areas behind big sphere clusters that diminish the local HT enhancement on the flat regions of the plate.

Other correlation coefficients, which have been described in Sec. 3.4.3, have been applied to the data. The resulting correlations can be observed in Table 4.3. From the PIV data no conclusions can be drawn, the correlations found are very weak. Furthermore, the Pearson correlation coefficient is not appropriate in this scenario as it tries to identify if there is a linear relationship between the data, which is obviously not the case. Moreover, the correlation shows a negative relation, this would mean that the HT decreases as the velocity increases, which is the opposite to what is expected in reality. The same can be said about the Spearman coefficient, it is very weak, even though the p value is lower than the significance level of 0.05. When applying the same correlation formulas to the CFD data, a clearer trend appears, a higher TKE results on a higher HT, as we found when analyzing the high velocity/TKE regions using Fig. 4.23 and the data in Table 4.3.
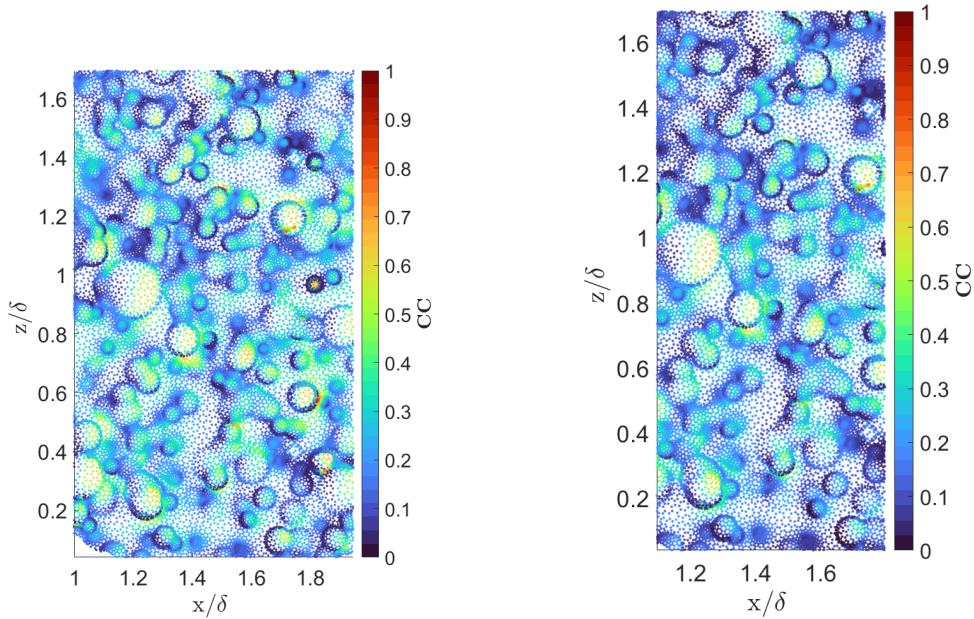
(a) Correlation distribution between mean velocity magnitude and Nu.

(b) Correlation distribution between TKE and Nu.

Figure 4.22: Correlation distributions for near wall CFD data at a Re $\approx 2.00 \times 10^4$.

These correlation coefficients were also applied to the wall-shear stress values extracted from the CFD and a significantly stronger correlation was found. This demonstrates its notable influence on HT. Upon comparing τ_w with the local Nu from the CFD, an even stronger relationship is found. The high Pearson coefficient obtained in this comparison suggests that there is an almost linear relation between the two variables. The notable difference observed when using CFD or SRHT local Nu implies that in the CFD the τ_w, linked to the boundary layer thickness, is the main driver of HT.

Table 4.4: Results from other correlation coefficients applied to heat transfer.

		PIV		CFD			
		Vel	TKE	Vel	TKE	τ_w	τ_w & CFD Nu
Pearson		-0.0992	-0.0946	0.0891	0.1621	0.5016	0.8785
Spearman	ρ	-0.1053	0.0142	0.0662	0.1687	0.4705	0.8431
	p	0	0.0178	0	0	0	0

4.2.5. Boundary Layer Measurements

As mentioned earlier in Sec. 2.5.1, the increase in roughness will disturb the boundary layer to some degree. This results in an increase in the wall shear stress which considerably affects the velocity profile near the wall. However, this disruption should be limited to the roughness sublayer and the outer layer should remain unaffected. In an attempt to capture this effect, and calculate the wall friction velocity, a testing campaign was performed in which the testing plane was perpendicular to the plates, as mentioned previously.

The modified Clauser chart method, explained in Sec. 3.4.1, was applied to the measured data so as to obtain a value for u_τ. The method was applied in the range from $3*R_z$ up to $0.6*\delta_{99}$. From studies like that by Ivan Marusic et al. [86] the log region only extends up to $0.15*\delta_{99}$. However, the measured R_z corresponds to a value of $\approx 0.1*\delta_{99}$, for this reason it was decided to relax the upper limit up to $0.6*\cdot\delta_{99}$. Note that, the R_z was used as the characteristic roughness height and zero displacement point (y_0). Fig. 4.28 compares the measured mean velocity profile for the smooth wall with that of the rough analogue surface at different values of friction Reynolds number ($Re_\tau = u_\tau D_h/\nu$). The values of u_τ obtained can be observed in Table 4.5 together with the corresponding R_z^+ & ΔU^+. Other methods were employed to obtain u_τ and predict y_0, like that proposed by Hama [87], however, these proved unfruitful.
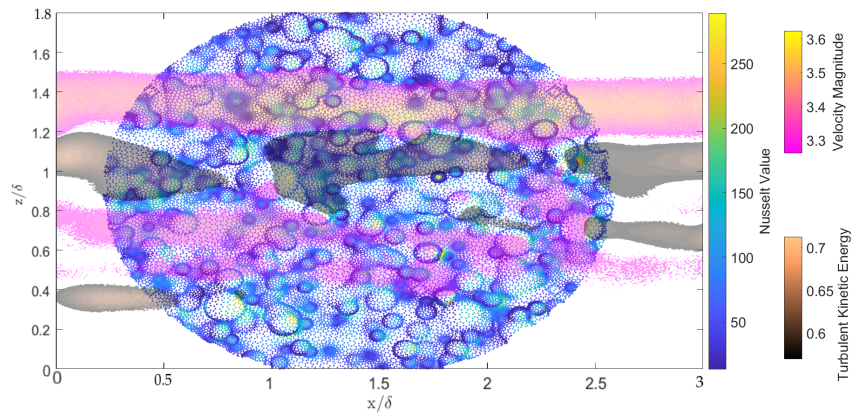
Figure 4.23: Superposition of high velocity/TKE regions extracted from the CFD data over the measured Nu by W. Kaibin [65].
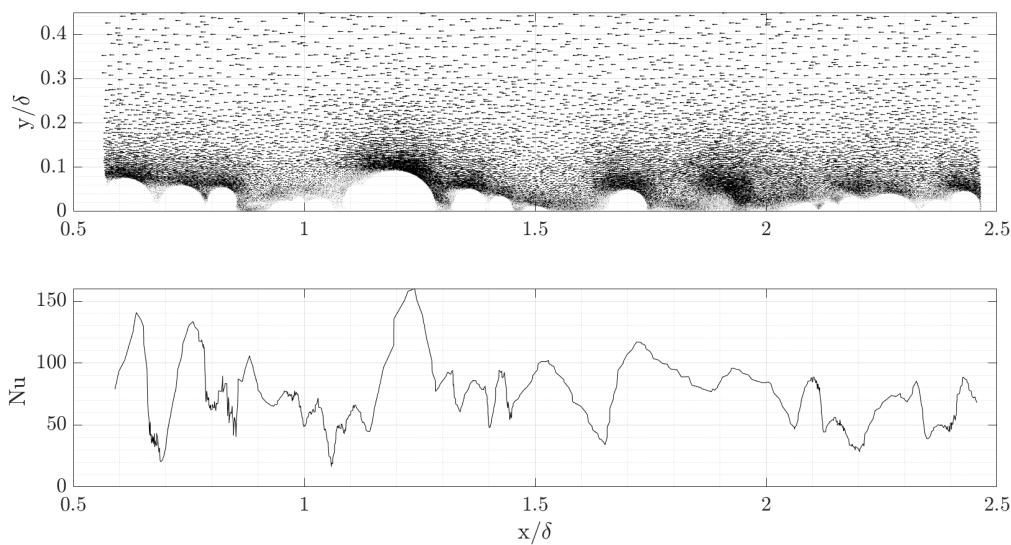
Figure 4.24: Heat transfer distribution (W. Kaibin [65]) along the center plate line together with the flow vector plot at the plane perpendicular to the rough analogue surface (CFD).

The shift in velocity follows a logarithmic relation to the non-dimensional equivalent sand grain roughness (k_s^+) and is independent of the wall distance [9]. The k_s parameter is undefined for the surface roughness generated by AM. Some authors have proposed correlations to calculate the equivalent sand-grain roughness using the roughness parameters, however, obtaining it falls outside the scope of this thesis, thus R_z was employed. The measured Re_z^+ indicates that the viscous sublayer has been completely destroyed by the roughness as the values are higher than the upper limit of the transitionally rough regime, which is typically considered to be <90 depending on the author and type of roughness.

The measured shift in the velocity profile is quite high when compared to the data found in the literature [9]. This could be due to several reasons. First, the measurements were performed at only one location, which means that the velocity profile measured is highly influenced by the spheres there. To prevent this it would be recommendable to perform tests at several different locations and averaging them. Furthermore, the value employed for the zero displacement plane probably is incorrect. This topic of research is quite extend and some like Flack and Schultz [88] have spent years investigating the turbulent flow over rough surfaces, affirming that there is not a "universal" roughness function. This could be a research topic for future investigations.

Finally, mention that the defect law and Reynolds Stresses will not be presented for the rough analogue
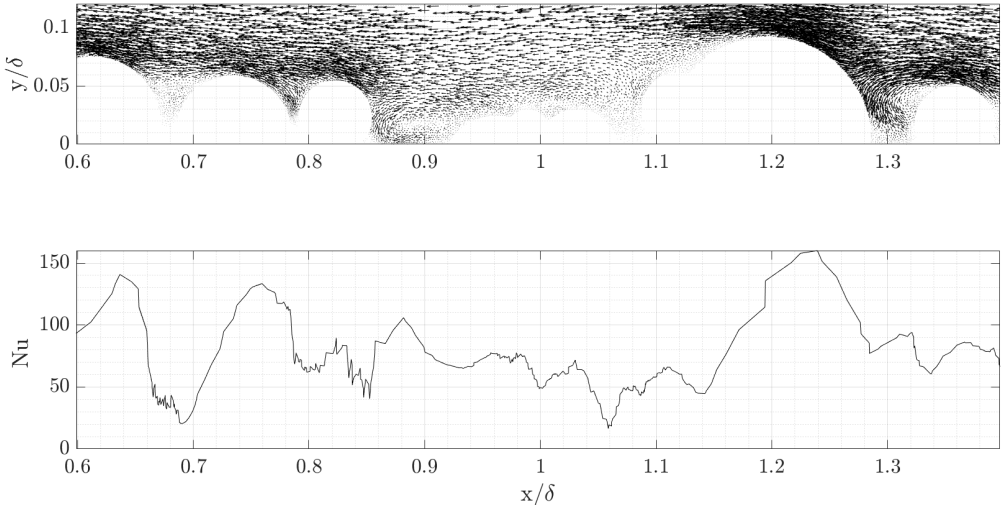
Figure 4.25: Zoom in image of Fig. 4.24.
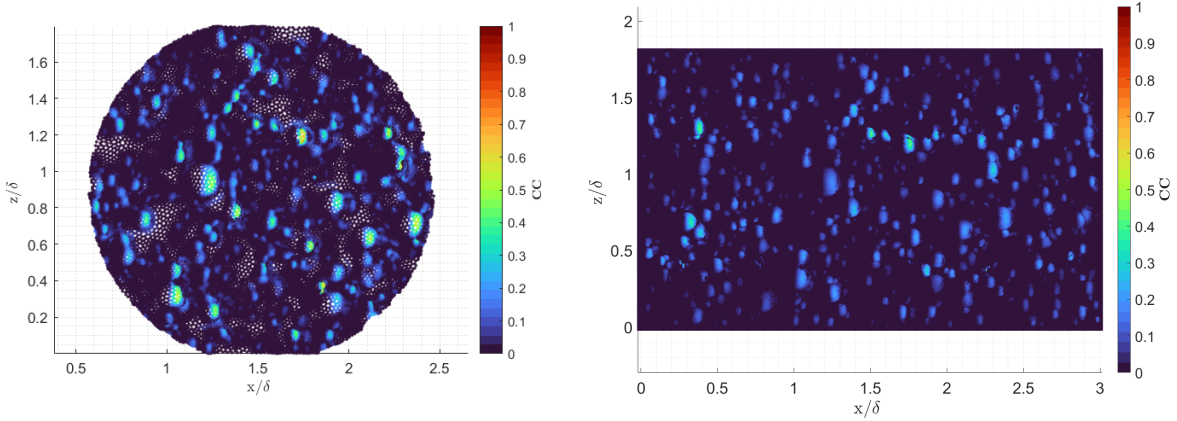
(a) Correlation distribution between the wall shear stress and SRHT rig local Nu.

(b) Correlation distribution between the wall shear stress and CFD local Nu.

Figure 4.26: Correlation distributions for CFD wall shear stress at a $Re \approx 2.00 \times 10^4$.

surface. These will not be reliable as we have no means of verifying that the measured u_τ, ϵ, etc. are accurate.

(a) SRHT data.

(b) CFD data.
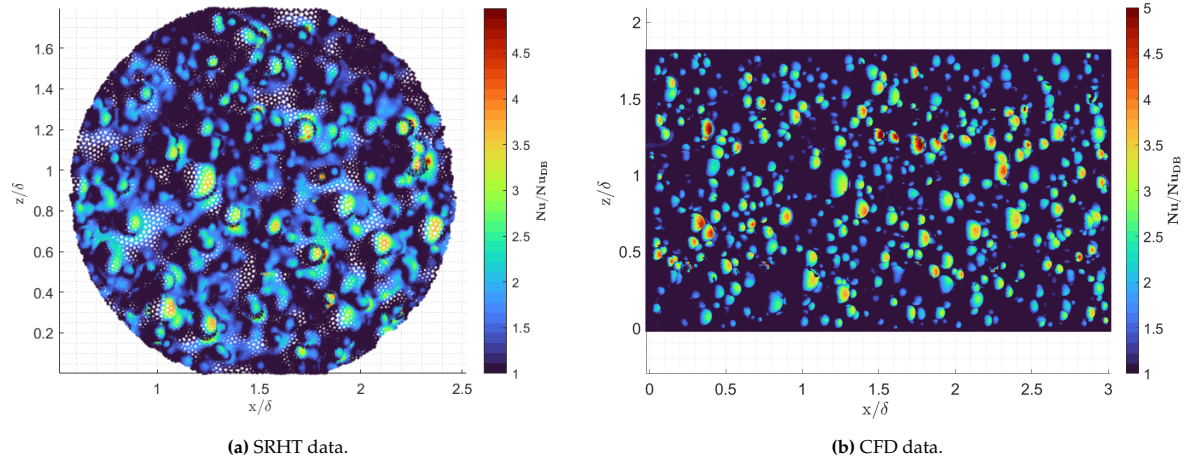
Figure 4.27: Local Nu enhancement maps at a Re $\approx 2.00 \times 10^4$.
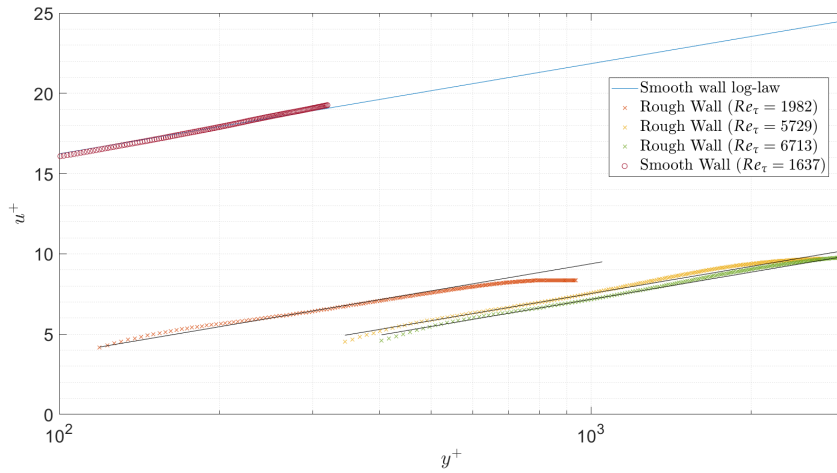
Figure 4.28: Comparison of the mean velocity profile from the experimental PIV rough analogue surface data vs smooth wall theoretical log-law region.

Table 4.5: Boundary layer parameters measured during the testing of the rough analogue surface.

Re	$\delta_{99}[m]$	δ_{99}^+	$u_\tau[ms^{-1}]$	ΔU^+	Re_z^+
13444	0.0486	1015	0.314	12.47	120
28428	0.0495	1956	0.606	13.51	231
46494	0.0394	2934	0.909	14.32	347
55316	0.0424	3437	1.065	14.68	406

5

Conclusion and Future Work

In this section the conclusions of the project are drawn together with the recommend future work.

5.1. Conclusions

A functional PIV system has been setup, and the upscaled analogue rough surface tested. Additionally, a preliminary assessment of the flow quality in the wind-tunnel and PIV system accuracy has been completed. Tests have been performed in order to study the localized effects of the surface roughness on heat transfer enhancement in a turbine cooling channel. Overall, the conclusions drawn can be summed up as follows:

1. The boundary layer at the test section location with smooth walls has been characterized. The Reynolds stresses have been computed successfully and the velocity profiled showed strong agreement with universal scaling laws, like the log-law and defect law. Therefore, the wind-tunnel was validated. Furthermore, as a secondary task, the entrance region has been identified, showing the evolution of the velocity profile along the test section.

2. Assisted by the CFD data, it has been demonstrated that the flow stagnation points are the main contributor to the heat transfer of the surface roughness studied. The zones of high wall shear, corresponding mainly to impingement points, match with the locations of higher heat transfer.

3. It has been shown that the high surface roughness leads to a complex flow behaviour and high turbulence levels. The regions of high turbulence, mainly after relatively big spheres, seem present higher heat transfer.

4. Secondary flow characteristics have been identified in the PIV measurement, like high speed streaks and the wake regions from some spheres.

5. Further development of the current PIV system is necessary to enable flow measurements closer to the rough analogue surface, thus enabling the measurement of localized effects close to the wall.

5.2. Future Work

The work on the PIV rig will be continued in the future by other master thesis students. This study has been the first utilization of the rig and the initial assembly and operation of it, therefore there is significant potential for further work and improvement. The main topics that can be addressed are:

1. Extend the test section where rough plates can be place to ensure that the flow is fully developed.

2. Improve the SNR, particularly when testing near the wall. This can be achieved by using a fluorescent paint to the plates. These would then reflect the light at a different wavelength from the laser. Subsequently, a filter can be placed on the camera lens so that only the specific wavelength from the laser is captured.

3. Add an appropriate laser dump after the test section to avoid reflections from the walls of the room, further enhancing the SNR.

4. Test other rough surfaces available to compare the HT mechanism that are taking place.

5. Derive HT-flow analogies, similar to the Reynolds analogy, to relate pressure drop and HT to the flow characteristics/ roughness parameters.

References

[1] Hannah Ritchie, Pablo Rosado, and Max Roser. "Energy Production and Consumption". In: *Our World in Data* (2020).

[2] K.K. Gupta, A. Rehman, and R.M. Sarviya. "Bio-fuels for the gas turbine: A review". In: *Renewable and Sustainable Energy Reviews* 14.9 (2010), pp. 2946–2955.

[3] Ozum Calli, C. Ozgur Colpan, and Huseyin Gunerhan. "Chapter 2.3 - Performance Assessment of a Biomass-Fired Regenerative ORC System Through Energy and Exergy Analyses". In: *Exergetic, Energetic and Environmental Dimensions*. Ed. by Ibrahim Dincer, C. Ozgur Colpan, and Onder Kizilkan. Academic Press, 2018, pp. 253–277. ISBN: 978-0-12-813734-5.

[4] Umesh Unnikrishnan and Vigor Yang. "A review of cooling technologies for high temperature rotating components in gas turbine". In: *Propulsion and Power Research* 11.3 (2022), pp. 293–310. ISSN: 2212-540X.

[5] Marwan Effendy et al. "Detached eddy simulation of blade trailing-edge cutback cooling performance at various ejection slot angles". In: *International Journal of Heat and Fluid Flow* 80 (Dec. 2019), p. 108487.

[6] Je-Chin Han. "Recent Studies in Turbine Blade Cooling". In: *International Journal of Rotating Machinery* 10 (Nov. 2004).

[7] Jacob C. Snyder and Karen A. Thole. "Understanding Laser Powder Bed Fusion Surface Roughness". In: *Journal of Manufacturing Science and Engineering* 142.7 (2020), p. 071003. ISSN: 1087-1357.

[8] Chao Zhang et al. "Additive manufacturing of products with functional fluid channels: A review". In: *Additive Manufacturing* 36 (2020), p. 101490. ISSN: 2214-8604.

[9] Mohammadreza Kadivar, David Tormey, and Gerard McGranaghan. "A review on turbulent flow over rough surfaces: Fundamentals and theories". In: *International Journal of Thermofluids* 10 (2021), p. 100077. ISSN: 2666-2027. DOI: https://doi.org/10.1016/j.ijft.2021.100077.

[10] Linda Candy. "Practice Based Research: A Guide". In: *Creativity and Cognition Studios Report* 1 (Nov. 2006).

[11] *Thermodynamics and Propulsion MIT notes*. MIT web course notes. URL: https://web.mit.edu/16.unified/www/FALL/thermodynamics/notes/node4.html.

[12] Shailendra Naik. "Basic Aspects of Gas Turbine Heat Transfer". In: Apr. 2017. ISBN: 978-953-51-3093-2. DOI: 10.5772/67323.

[13] Ronald Scott Bunker, Jason Edward Dees, and Pepe Palafox. "Impingement Cooling In Gas Turbines:Design, Applications, And Limitations". In: *WIT Transactions on State-of-the-art in Science and Engineering* 76 (2014).

[14] Jingzhou ZHANG et al. "Recent advances in film cooling enhancement: A review". In: *Chinese Journal of Aeronautics* 33.4 (2020), pp. 1119–1136. ISSN: 1000-9361. DOI: https://doi.org/10.1016/j.cja.2019.12.023.

[15] Peter Ajersch. "Detailed measurements on a row of jets in a crossflow : With applications". PhD thesis. Apr. 1995. DOI: 10.14288/1.0081025.

[16] Q. Mi et al. "Research progress of transpiration cooling for aircraft thermal protection". In: *Applied Thermal Engineering* 236 (2024), p. 121360. ISSN: 1359-4311. DOI: https://doi.org/10.1016/j.applthermaleng.2023.121360.

[17] MATSUSHITA Laboratory - Ashikaga University. "Thermal Engineering Laboratory". In: (). URL: https://www2.ashitech.ac.jp/mech/matsushita/indexen.html.

[18] Kumar Kanishka and Bappa Acherjee. "Revolutionizing manufacturing: A comprehensive overview of additive manufacturing processes, materials, developments, and challenges". In: *Journal of Manufacturing Processes* 107 (2023), pp. 574–619. ISSN: 1526-6125. DOI: `https://doi.org/10.1016/j.jmapro.2023.10.024`.

[19] Abbas Razavykia et al. "An Overview of Additive Manufacturing Technologies—A Review to Technical Synthesis in Numerical Study of Selective Laser Melting". In: *Materials* 13 (2020). URL: `https://api.semanticscholar.org/CorpusID:221573299`.

[20] Shubhavardhan Ramadurga Narasimharaju et al. "A comprehensive review on laser powder bed fusion of steels: Processing, microstructure, defects and control methods, mechanical properties, current challenges and future trends". In: *Journal of Manufacturing Processes* 75 (2022), pp. 375–414. ISSN: 1526-6125. DOI: `https://doi.org/10.1016/j.jmapro.2021.12.033`.

[21] *Dependence of LPBF Surface Roughness on Laser Incidence Angle and Component Build Orientation*. Vol. Volume 7: Industrial and Cogeneration; Manufacturing Materials and Metallurgy. Turbo Expo: Power for Land, Sea, and Air. June 2021, V007T17A015. DOI: `10.1115/GT2021-59755`.

[22] *Impact of Additive Manufacturing on Internal Cooling Channels With Varying Diameters and Build Directions*. Vol. Volume 7A: Heat Transfer. Turbo Expo: Power for Land, Sea, and Air. Sept. 2020, V07AT15A017. DOI: `10.1115/GT2020-15049`.

[23] Vaibhav Bhosale et al. "Analysis of process parameters of 3D printing for surface finish, printing time and tensile strength". In: *Materials Today: Proceedings* 59 (2022). Third International Conference on Recent Advances in Materials and Manufacturing 2021, pp. 841–846. ISSN: 2214-7853. DOI: `https://doi.org/10.1016/j.matpr.2022.01.210`.

[24] Anand K Bewoor. *Metrology & measurement*. Tata McGraw-Hill Education, 2009.

[25] J. Raja, B. Muralikrishnan, and Shengyu Fu. "Recent advances in separation of roughness, waviness and form". In: *Precision Engineering* 26.2 (2002), pp. 222–235. ISSN: 0141-6359. DOI: `https://doi.org/10.1016/S0141-6359(02)00103-4`.

[26] E. NAPOLI, V. ARMENIO, and M. DE MARCHIS. "The effect of the slope of irregularly distributed roughness elements on turbulent wall-bounded flows". In: *Journal of Fluid Mechanics* 613 (2008), pp. 385–394. DOI: `10.1017/S0022112008003571`.

[27] Galina Kasperovich et al. "The effect of build direction and geometric optimization in laser powder bed fusion of Inconel 718 structures with internal channels". In: *Materials and Design* 207 (2021), p. 109858. ISSN: 0264-1275. DOI: `https://doi.org/10.1016/j.matdes.2021.109858`.

[28] Lei Zhou et al. "A comprehensive model to predict friction factors of fluid channels fabricated using laser powder bed fusion additive manufacturing". In: *Additive Manufacturing* 47 (2021), p. 102212. ISSN: 2214-8604. DOI: `https://doi.org/10.1016/j.addma.2021.102212`.

[29] Curtis K. Stimpson et al. "Scaling Roughness Effects on Pressure Loss and Heat Transfer of Additively Manufactured Channels". In: *Journal of Turbomachinery* 139.2 (Sept. 2016), p. 021003. ISSN: 0889-504X.

[30] Jerry Westerweel, Bendiks Boersma, and Frans Nieuwstadt. *Turbulence*. Jan. 2016. ISBN: 978-3-319-31597-3. DOI: `10.1007/978-3-319-31599-7`.

[31] Oleg Gulinsky, Andrey Rogatkin, and Vadim Vorobyov. "Singularity MAXI: A comparison of CFD and Tank test results". In: Mar. 2015.

[32] Amgad Salama. "Velocity Profile Representation for Fully Developed Turbulent Flows in Pipes: A Modified Power Law". In: *Fluids* 6.10 (2021). ISSN: 2311-5521.

[33] Kaighin A. McColl et al. "Mean-velocity profile of smooth channel flow explained by a cospectral budget model with wall-blockage". In: *Physics of Fluids* 28.3 (Mar. 2016), p. 035107. ISSN: 1070-6631.

[34] Ariel Ferrera. "Harvesting Power-Modular High-Rise Cooling Tower Hydro Turbine -Commercial Economizer Design**". In: May 2020.

[35] Frank P. Incropera. "Fundamentals of Heat and Mass Transfer". In: 1981. URL: `https://api.semanticscholar.org/CorpusID:107049581`.

[36] Y. Cengel and J. Cimbala. *Fluid Mechanics Fundamentals and Applications: Third Edition*. MCGRAW-HILL US HIGHER ED, 2013. ISBN: 9780077595418. URL: `https://books.google.se/books?id=QZIjAAAAQBAJ`.

[37] J. Nikuradse. "Stromungsgesetze in rauhen Rohren". In: 1933. URL: `https://api.semanticscholar.org/CorpusID:232667976`.

[38] G. Hagen. "Ueber die Bewegung des Wassers in engen cylindrischen Röhren". In: *Annalen der Physik* 122 (), pp. 423–442.

[39] Henry Darcy. "Recherches expérimentales relatives au mouvement de l'eau dans les tuyaux". In: URL: `https://api.semanticscholar.org/CorpusID:118018324`.

[40] Hermann Schlichting. "Experimentelle Untersuchungen zum Rauhigkeitsproblem". In: *Ingenieur-Archiv* 7 (1936), pp. 1–34. URL: `https://api.semanticscholar.org/CorpusID:122277243`.

[41] Lewis F. Moody. "Friction Factors for Pipe Flow". In: *Journal of Fluids Engineering* (1944). URL: `https://api.semanticscholar.org/CorpusID:254712400`.

[42] C. F. Colebrook and C M White. "Experiments with Fluid Friction in Roughened Pipes". In: *Proceedings of The Royal Society A: Mathematical, Physical and Engineering Sciences* 161 (1937), pp. 367–381. URL: `https://api.semanticscholar.org/CorpusID:136598986`.

[43] W. F. Cope. "The Friction and Heat Transmission Coefficients of Rough Pipes". In: 1941. URL: `https://api.semanticscholar.org/CorpusID:110400004`.

[44] D. F. Dipprey and Rolf Heinrich Sabersky. "HEAT AND MOMENTUM TRANSFER IN SMOOTH AND ROUGH TUBES AT VARIOUS PRANDTL NUMBERS". In: *International Journal of Heat and Mass Transfer* 6 (1963), pp. 329–353. URL: `https://api.semanticscholar.org/CorpusID:227359804`.

[45] Mario Dalle Donne and Leonhard Meyer. "Turbulent convective heat transfer from rough surfaces with two-dimensional rectangular ribs". In: *International Journal of Heat and Mass Transfer* 20 (1977), pp. 583–620. URL: `https://api.semanticscholar.org/CorpusID:122021209`.

[46] M. Wong et al. "Convective heat transfer and pressure losses across novel heat sinks fabricated by Selective Laser Melting". In: *International Journal of Heat and Mass Transfer* 52.1 (2009), pp. 281–288. ISSN: 0017-9310.

[47] Yannick Cormier et al. "Additive manufacturing of pyramidal pin fins: Height and fin density effects under forced convection". In: *International Journal of Heat and Mass Transfer* 75 (2014), pp. 235–244. ISSN: 0017-9310.

[48] Luigi Ventola et al. "Rough surfaces with enhanced heat transfer for electronics cooling by direct metal laser sintering". In: *International Journal of Heat and Mass Transfer* 75 (2014), pp. 58–74. ISSN: 0017-9310.

[49] Jacob C. Snyder et al. "Build Direction Effects on Additively Manufactured Channels". In: *Journal of Turbomachinery* 138.5 (Jan. 2016), p. 051006. ISSN: 0889-504X.

[50] Curtis K. Stimpson et al. "Roughness Effects on Flow and Heat Transfer for Additively Manufactured Channels". In: *Journal of Turbomachinery* 138.5 (Jan. 2016), p. 051008. ISSN: 0889-504X.

[51] J.W.R. Peeters and N.D. Sandham. "Turbulent heat transfer in channels with irregular roughness". In: *International Journal of Heat and Mass Transfer* 138 (2019), pp. 454–467. ISSN: 0017-9310. DOI: `https://doi.org/10.1016/j.ijheatmasstransfer.2019.04.013`.

[52] S.Y Son, K.D Kihm, and J.-C Han. "PIV flow measurements for heat transfer characterization in two-pass square channels with smooth and 90° ribbed walls". In: *International Journal of Heat and Mass Transfer* 45.24 (2002), pp. 4809–4822. ISSN: 0017-9310. DOI: `https://doi.org/10.1016/S0017-9310(02)00192-8`.

[53] Y. Kuwata et al. "Scaling of the roughness effects in turbulent flows over systematically-varied irregular rough surfaces". In: *International Journal of Heat and Fluid Flow* 101 (2023), p. 109130. ISSN: 0142-727X. DOI: `https://doi.org/10.1016/j.ijheatfluidflow.2023.109130`.

[54] Chinmay Shingote, Farshad Barghi Golezani, and Chirag R. Kharangate. "Investigation of fluid flow during flow boiling inside a horizontal rectangular channel with single-sided heating using particle image velocimetry". In: *Experimental Thermal and Fluid Science* 156 (2024), p. 111221. ISSN: 0894-1777. DOI: https://doi.org/10.1016/j.expthermflusci.2024.111221.

[55] Markus Raffel et al. *Particle image velocimetry: a practical guide*. Springer, 2018.

[56] Markus Raffel. "Particle Image Velocimetry: A Practical Guide". In: 2002.

[57] Fulvio Scarano. *AE4-180 Experimental Aerodynamics*. Delft University of Technology course notes, 2008.

[58] *Flow in a Scaled Turbine Coolant Channel With Roughness due to Additive Manufacturing*. Vol. Volume 5B: Heat Transfer. Turbo Expo: Power for Land, Sea, and Air. June 2019, V05BT21A004. URL: https://doi.org/10.1115/GT2019-90931.

[59] Kevin Zhong, Nicholas Hutchins, and Daniel Chung. "Heat-transfer scaling at moderate Prandtl numbers in the fully rough regime". In: *Journal of Fluid Mechanics* 959 (2023), A8. DOI: 10.1017/jfm.2023.125.

[60] W. Abu Rowin et al. "Modelling the effect of roughness density on turbulent forced convection". In: *Journal of Fluid Mechanics* 979 (2024), A22. DOI: 10.1017/jfm.2023.1063.

[61] Jiri Blazek. *Computational fluid dynamics: principles and applications*. Butterworth-Heinemann, 2015.

[62] Peter Alan Davidson. *Turbulence: an introduction for scientists and engineers*. Oxford university press, 2015.

[63] David C Wilcox et al. *Turbulence modeling for CFD*. Vol. 2. DCW industries La Canada, CA, 1998.

[64] OpenAI. *ChatGPT*. 2024. URL: https://chat.openai.com.

[65] Wen Kaibin. "Investigation of Roughness Effects on Heat Transfer of Upscaled Additively Manufactured Channels in the Turbulent Region Using Infrared Thermography". In: *M.S. thesis, KTH Royal Institute of Technology* (2023).

[66] Edgar Buckingham. "On physically similar systems; illustrations of the use of dimensional equations". In: *Physical review* 4.4 (1914), p. 345.

[67] LR Glicksman, MR Hyre, and PA Farrell. "Dynamic similarity in fluidization". In: *International Journal of Multiphase Flow* 20 (1994), pp. 331–386.

[68] J Paul Day. "Substrate contributions to automotive catalytic converter performance: The role of channel shape on catalyst efficiency". In: *Studies in surface science and catalysis*. Vol. 116. Elsevier, 1998, pp. 453–463.

[69] John-Mark Clemenson, Timothy A Shannon, and Stephen T McClain. "A Novel Method for Constructing Analog Roughness Patterns to Replicate Ice Accretion Characteristics". In: *2018 Atmospheric and Space Environments Conference*. 2018, p. 3015.

[70] A. Björnram and K. Ljunggren. "Characterization of additively manufactured surfaces of cooling channels". In: *M.S. thesis, Linköping University* (2022).

[71] P. Lehmann. "Investigation of the local heat transfer characteristics on additively manufactured surfaces using infrared thermography". In: *M.S. thesis, Technical University of Munich* (2023).

[72] William Thielicke and E J Stamhuis. "PIVlab – Towards User-friendly, Affordable and Accurate Digital Particle Image Velocimetry in MATLAB". In: *Journal of Open Research Software* 2 (Oct. 2014). DOI: 10.5334/jors.bl.

[73] William Thielicke and Rene Sonntag. "Particle Image Velocimetry for MATLAB: Accuracy and enhanced algorithms in PIVlab". In: *Journal of Open Research Software* 9 (May 2021). DOI: 10.5334/jors.334.

[74] Afshin Ghajar and Yunus Cengel. *Heat and Mass Transfer - Fundamentals and Applications, 6th Edition, McGraw-Hill Education, New York, NY, 2020*. Apr. 2021.

[75] Tie Wei, Rodney Schmidt, and Patrick Mcmurtry. "Comment on the Clauser chart method for determining the friction velocity". In: *Experiments in Fluids* 38 (May 2005), pp. 695–699.

[76] P. Bhandari. "Correlation Coefficient | Types, Formulas & Examples." In: *Scribbr* (2023). URL: https://www.scribbr.com/statistics/correlation-coefficient/.

[77] Ronald Adrian. "Dynamic ranges and spatial resolution of particle image velocimetry". In: *Measurement Science and Technology* 8 (Jan. 1999), p. 1393. DOI: 10.1088/0957-0233/8/12/003.

[78] R. Hain and Christian Kähler. "Fundamentals of multiframe particle image velocimetry (PIV)". In: *Experiments in Fluids* 42 (Apr. 2007), pp. 575–587. DOI: 10.1007/s00348-007-0266-6.

[79] John Charonko and Pavlos Vlachos. "Estimation of uncertainty bounds for individual particle image velocimetry measurements from cross-correlation peak ratio". In: *Measurement Science and Technology* 24 (Apr. 2013), p. 065301. DOI: 10.1088/0957-0233/24/6/065301.

[80] Zhenyu Xue, John James Charonko, and Pavlos P. Vlachos. "Signal-to-noise ratio, error and uncertainty of PIV measurement". In: 2013. URL: https://api.semanticscholar.org/CorpusID:67781010.

[81] Y. S. Kwon et al. "The quiescent core of turbulent channel flow". In: *Journal of Fluid Mechanics* 751 (2014), pp. 228–254.

[82] Masoud Asadi, Md Kamruzzaman, and R. Jason Hearst. "The effect of inlet turbulence on the quiescent core of turbulent channel flow". In: *Journal of Fluid Mechanics* 935 (2022), A37. DOI: 10.1017/jfm.2022.36.

[83] Christopher Greenshields and Henry Weller. *Notes on Computational Fluid Dynamics: General Principles*. Reading, UK: CFD Direct Ltd, 2022.

[84] Robert Moser, John Kim, and Nagi Mansour. "Direct Numerical Simulation of Turbulent Channel Flow up to Re_τ=590". In: *Physics of Fluids - PHYS FLUIDS* 11 (Apr. 1999), pp. 943–945. DOI: 10.1063/1.869966.

[85] Guo-Zhen Ma et al. "Secondary motions and wall-attached structures in a turbulent flow over a random rough surface". In: *International Journal of Heat and Fluid Flow* 102 (2023), p. 109147. ISSN: 0142-727X. DOI: https://doi.org/10.1016/j.ijheatfluidflow.2023.109147.

[86] Ivan Marusic et al. "On the logarithmic region in wall turbulence". In: *Journal of Fluid Mechanics* 716 (2013), R3. DOI: 10.1017/jfm.2012.511.

[87] Francis R Hama. "Boundary layer characteristics for smooth and rough surfaces". In: *Trans. Soc. Nav. Arch. Marine Engrs.* 62 (1954), pp. 333–358.

[88] Karen A Flack and Michael P Schultz. "Roughness effects on wall-bounded turbulent flows". In: *Physics of Fluids* 26.10 (2014).

[89] O Reynolds. "On the Dynamical Theory of Incompressible Viscous Fluids and the Determination of the Criterion (Reprinted from Papers on Mechanical and Physical Subjects, Vol 2, Pg 535-577, 1901)". In: *Proceedings of the Royal Society-Mathematical and Physical Sciences*. Vol. 451. 1941. ROYAL SOC 6-9 CARLTON HOUSE TERRACE, LONDON SW1Y 5AG, ENGLAND. 1995, pp. 5–47.

[90] Stephen B Pope. "Turbulent flows". In: *Measurement Science and Technology* 12.11 (2001), pp. 2020–2021.

[91] FT Nieuwstadt, Jerry Westerweel, and B Boersma. *Introduction to Theory and Applications of Turbulent Flows*. Springer, 2016.

[92] Philippe Spalart and Steven Allmaras. "A one-equation turbulence model for aerodynamic flows". In: *30th aerospace sciences meeting and exhibit*. 1992, p. 439.

[93] P Yo Chou. "On velocity correlations and the solutions of the equations of turbulent fluctuation". In: *Quarterly of applied mathematics* 3.1 (1945), pp. 38–54.

[94] JC Rotta. "Statistische theorie nichthomogener turbulenz". In: *Zeitschrift für Physik* 129 (1951), pp. 547–572.

[95] Blade Flutter. "An Internet Book on Fluid Dynamics". In: 2015.

[96] Peter S. Bernard and Robert A. Handler. "Reynolds stress and the physics of turbulent momentum transport". In: *Journal of Fluid Mechanics* 220 (1990), pp. 99–124. DOI: 10.1017/S0022112090003202.

<div align="right">

A

</div>
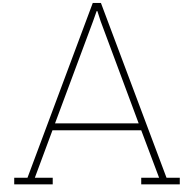
Reynolds Averaged Navier-Stokes

This chapter is dedicated to the derivation of the Reynolds Averaged Navier-Stokes (RANS) equations starting from the Navier-Stokes equations [89].

Following this, a brief overview of the different turbulence closure models available will be given. Moreover, the Reynolds stresses will be described.

A.1. RANS Equations Derivation

The partial differential equations that describe the motion of a viscous fluid are the Navier-Stokes equations. Eq. A.1 & A.2 represent the conservation of continuity and momentum, respectively, within a small control volume for an incompressible fluid.

$$\frac{\partial u_i}{\partial x_i} = 0 \tag{A.1}$$

$$\frac{\partial u_i}{\partial t} + u_j \frac{\partial u_i}{\partial x_j} = f_i - \frac{1}{\rho}\frac{\partial p}{\partial x_i} + \nu \frac{\partial^2 u_i}{\partial x_j^2} \tag{A.2}$$

In order to derive the RANS equations, a basic assumption has to be made. This is that the velocity field can be split into a mean (time-averaged) component $\overline{u}$, and a fluctuating component u' [90] [91]. Therefore, u can be expressed as $u(\mathbf{x}, t) = \overline{u}(\mathbf{x}) + u'(\mathbf{x}, t)$, where $\mathbf{x}$ represents the position vector. This is known as the Reynolds decomposition which follows some specific rules [91]:

$$\overline{\overline{f}} = \overline{f}$$
$$\overline{f + g} = \overline{f} + \overline{g}$$
$$\overline{\overline{f}g} = \overline{f}\,\overline{g}$$
$$\overline{fg} \neq \overline{f}\,\overline{g}$$
$$\overline{\frac{\partial f}{\partial s}} = \frac{\partial \overline{f}}{\partial s}$$

By substituting the decomposition for u_i, u_j, p and f_i this yields:

$$\frac{\partial \overline{u}_i}{\partial x_i} = 0$$

$$\frac{\partial \overline{u}_i}{\partial t} + \overline{u}_j \frac{\partial \overline{u}_i}{\partial x_j} + \overline{u'_j \frac{\partial u'_i}{\partial x_j}} = \overline{f}_i - \frac{1}{\rho}\frac{\partial \overline{p}}{\partial x_i} + \nu \frac{\partial^2 \overline{u}_i}{\partial x_j^2}$$

By doing some algebra, the momentum equation can be expressed as:

$$\frac{\partial \overline{u}_i}{\partial t} + \frac{\partial \overline{u}_j \overline{u}_i}{\partial x_j} = \overline{f}_i - \frac{1}{\rho}\frac{\partial \overline{p}}{\partial x_i} + \nu \frac{\partial^2 \overline{u}_i}{\partial x_j^2} - \frac{\partial \overline{u'_i u'_j}}{\partial x_j}$$

In this last equation the partial derivative of a new non-linear term appears, the Reynolds Stress Tensor, $\tau'_{ij} = \overline{u'_i u'_j}$. This term introduces 6 new unknowns, but no new equations to close the system. For this reason, it has to be modeled in some way, to close the system of equations. One way to do this is by using the so called Eddie Viscosity, ν_t, together with the Boussinesq closure hypothesis [91]. This results in a linear one equation model, Eq. A.3 , where k is the turbulent kinetic energy, $k = \frac{1}{2}\overline{u'_i u'_j}$. Another example of a one equation closure model is the Spallart-Allmaras model (SA) [92]. Many other models exist, however in the CFD study used here the Reynolds Stress Model [93] [94] was used. This model adds six extra equations, each one corresponding to a component of the Reynolds Stress Tensor.

$$-\overline{u'_i u'_j} = \nu_t \left(\frac{\partial \overline{u}_i}{\partial x_j} + \frac{\partial \overline{u}_j}{\partial x_i} \right) - \frac{2}{3}k\delta_{ij} \tag{A.3}$$

The Reynolds stresses can be divided into two categories, the normal stresses, that consist of $u'u'$, $v'v'$ & $w'w'$, and the shear stresses that group $u'v'$, $u'w'$ & $v'w'$. In Fig. A.1 the magnitude of each term is presented, it is clear that the normal terms are very small when compared to the mean flow velocity. However, the shear terms must be compared to other viscous shear terms and in this case their magnitude might not be so small [95].
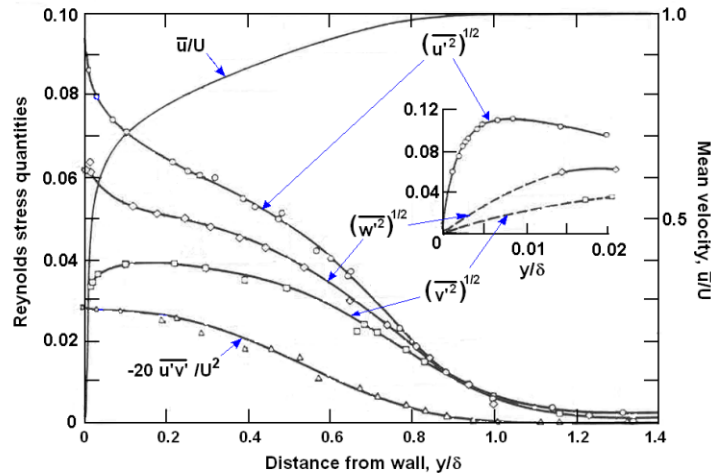

Figure A.1: Measurements of the Reynolds stresses in a turbulent boundary layer [95]

.

The Reynolds stresses originate from fundamental processes that involve the displacement and acceleration of particles and represent the net transport of momentum. They play a fundamental role in the creation and dissipation of turbulence, thus, they are essential in the development of turbulence models and when analyzing turbulent flows [96].

B

Arduino Synchronizer Code

*Arduino code used for the laser-camera synchronization.*

```
1    /*
2    Camera-Laser Synchronization
3
4    This code is used to synchronize the laser and camera. The Arduino code
         will make the camera start recording. Make sure, using the Chronos
5    webpage, that the camera I/O settings are correct. The Arduino will then
           read the output signal from the camera and send a trigger signal to
         each of the
6    laser heads.
7
8    Very important to check that the pins are connected correctly.
9
10   Created 19 February 2024
11   by Ambrosio
12
13   */
14
15
16   #include <digitalWriteFast.h>        // This is the library that uses
         PORT manipulation directly to make the digitalWrite function much
         faster. Used for the laser trigger signal.
17
18   volatile bool laserFlagT = false;    //
19   volatile bool laserFlagQ = false;    //
20   volatile bool startFlag = true;    //
21
22   int cameraPin = 5;            // Pin to which the camera exposure is
         connected.
23   int cameraPinOn = 4;          // pin to which the camera on/off trigger is
         connected.
24
25   int laserHead1PinT = 2;     //Pin to which the laserhead 1 lamphead
         trigger is connected.
26   int laserHead1PinQ = 3;     // Pin to which the laserhead 1 q-switch is
         connected.
27
28   int loopCounter = 0;     // Counter for number of loops.
```

```arduino
29   int loopLimit =1000;    // Final number of loops, note that each loop
        corresponds to an image pair.
30   int finalLoopCounter = 0;
31
32   unsigned long previousTime = 0; // Variable to store the previous time
        for micros()
33
34   void setup() {
35     // put your setup code here, to run once:
36     pinMode(cameraPin, OUTPUT);        // sets the digital pin as input
37     pinMode(laserHead1PinT, INPUT);   // sets the digital pin as output
38     pinMode(laserHead1PinQ, INPUT);   // sets the digital pin as output
39     pinMode(cameraPinOn, OUTPUT);
40
41     Serial.begin(9600); // open the serial port at 9600 bps:
42
43     delay(10);
44     digitalWriteFast(cameraPinOn,HIGH);
45   }
46
47   void loop() {
48     attachInterrupt(digitalPinToInterrupt(laserHead1PinT),triggerLaser,
          RISING);
49     attachInterrupt(digitalPinToInterrupt(laserHead1PinQ),QswitchLaser,
          RISING);
50
51     if (startFlag) {
52       // Here I send a false signal to the camera so that it records a few
            false black frames.
53       digitalWriteFast(cameraPin, HIGH);
54       delayMicroseconds(125);
55
56       digitalWriteFast(cameraPin,LOW);
57       delayMicroseconds(2);
58       digitalWriteFast(cameraPin, HIGH);
59       delay(10);
60
61       digitalWriteFast(cameraPin,LOW);
62     }
63
64     if (laserFlagT) {
65       // Sending the signal to open the camera shutter once the Lamp
            trigger signal is detected.
66       digitalWriteFast(cameraPin, HIGH);
67       laserFlagT = false;
68     }
69
70     if (laserFlagQ) {
71       // Sending the signal to close the camera shutter once the Q-switch
            trigger signal is detected.
72       digitalWriteFast(cameraPin,LOW);
73       delayMicroseconds(2); // Do not change this value
74
75       // Opening and closing the camera shutter for the second image frame
            .
76       digitalWriteFast(cameraPin, HIGH);
```

```
77        delay(10);
78        digitalWriteFast(cameraPin,LOW);
79        laserFlagQ = false;
80
81        loopCounter++;
82      }
83
84      // Detecting if the total number of desired frames have been captured
85      if (loopCounter == loopLimit) {
86        while (finalLoopCounter < 5) {
87          // Here I send a signal to the camera so that it records a few
                 black frames at the end.
88          digitalWriteFast(cameraPin, HIGH);
89          delayMicroseconds(125);
90          digitalWriteFast(cameraPin,LOW);
91          delayMicroseconds(2);
92          digitalWriteFast(cameraPin, HIGH);
93          delay(10);
94          digitalWriteFast(cameraPin,LOW)
95
96          finalLoopCounter++;
97        }
98
99        digitalWriteFast(cameraPinOn,LOW);
100       Serial.println("Finish");
101       while(true);
102     }
103   }
104
105
106   void triggerLaser() {
107     // Interrupt function that the Lamp trigger signal has been detected.
108     laserFlagT = true;
109     startFlag = false;
110   }
111
112   void QswitchLaser() {
113     // Interrupt function that the Q-switch trigger signal has been
            detected.
114     laserFlagQ = true;
115   }
```

C
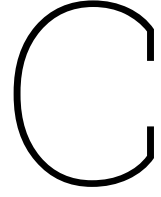
Gamma & Normal Distribution

In this chapter the probability distribution functions used for the sphere generation method discussed in Sec. 3.2.3 are described.

C.1. Gamma Distribution

The gamma distribution is a continuous probability distribution function that is defined by two parameters. There are two parameterizations that are commonly used. The first involves a shape parameter k and a scale parameter θ, while the second one uses the shape parameter $\alpha = k$ together with the inverse scale parameter $\beta = \frac{1}{\theta}$. All these parameters must be positive real numbers. In this project, the first parameterization was used for the sphere diameter generation, the corresponding function is that shown in Eq. C.1.

$$f(x; k, \theta) = \frac{x^{k-1} e^{-\frac{x}{\theta}}}{\theta^k \Gamma(k)} \tag{C.1}$$

The gamma function Γ is defined as:

$$\Gamma(k) = \int_0^\infty t^{k-1} e^{-t} dt$$

The mean μ and variance σ^2 of this distribution can be obtained from it's shape and scale parameters as:

$$\mu = k\theta$$
$$\sigma^2 = k\theta^2$$

Trying to match the diameter distribution measured by P. Lehmann in [71] did not yield appropiate results. Consequently, a relationship was established between the distribution parameters and the roughness parameters by W. Kaibin in [65]. This was done by trial and error, rather than finding a theoretically based connection between parameters. The resulting relationship established in his study is that:

$$\mu = 3.5 R_a$$
$$\sigma = R_q$$

C.2. Normal Distribution

The normal distribution, also called Gaussian distribution, is another continuous probability distribution function. The parameterization employed in this project is that shown in Eq. C.2. As defined for the gamma distribution, μ is the mean, while σ is the standard deviation.

$$f(x; \mu, \sigma) = \frac{1}{\sigma\sqrt{2\pi}} e^{-\frac{1}{2}\left(\frac{x-\mu}{\sigma}\right)^2} \tag{C.2}$$

This function was employed for the offset distribution in Sec. 3.2.3. However, the distribution parameters were determined by trial and error, no explicit relationship was established with the roughness parameters.

Flow Quality Assessment

In this chapter some of the issues identified with the current wind-tunnel setup are discussed. First, the asymmetry in the velocity profile will be examined. Subsequently, we will discuss whether or not the flow is fully developed at the test location.

D.1. Wind-tunnel Symmetry

As mentioned in Sec. 4.1, the initial center-channel measurements showed that the max velocity point on the stream-wise & time averaged velocity profile does not fall on the real center-channel position, see Fig. 4.3. To understand if this issue is due to human error, or intrinsic to the current set up an extensive testing campaign was performed. Measurements were made at several Re, changing the camera position and on different days. By randomizing the tests in this way we ensure that sources of systematic error are minimized. For simplicity, the results are presented by showing the value of U_0 and the non-dimensional position were it was measured, Fig. D.1 . A clear trend can be observed, at low Re numbers the center-channel position seems to be shifted to the left and moves to the right with increasing Re. Note that here the red crosses are excluded values as they differ more than 5% from the fitted line.
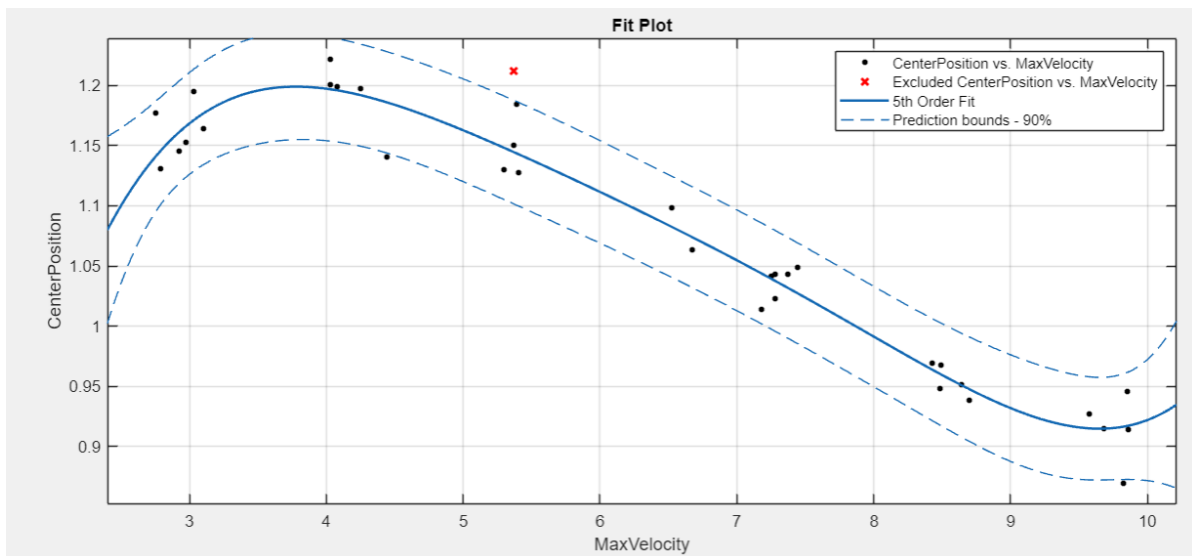

Figure D.1: Plot of measured U_0 vs U_0 position and the resulting polynomial fit.

The source of this problem is still to be identified, and in the future measures will be implemented to rectify this. However, due to time restrictions, it was decided to continue on with the testing campaign despite this issue. We consider that the effect on the flow close to the wall should be minimal and the

sphere's influence should dominate. Therefore, not much more effort has been placed on this, however, in the next analyses and future studies this should be taken into consideration.

D.2. Flow Development

In an attempt to study the entrance effect and flow development in the channel, a testing campaign was performed one plate upstream from the testing location, this corresponds to approximately $1.5 \cdot D_h$. The test were performed with the analogue rough surfaces. The resulting velocity profiles can be observed in Fig. D.2, depicted with a dashed line, note that the color legend is the same for both testing campaigns. From this image we can observe that there are slight differences in the velocity profile, however, the maximum difference is of less than 10%. Even though some of these deviations can probably be attributed to measurement errors, rig uncertainty, etc., it is clear that the flow is not yet fully developed at the measurement location. This is to be expected because the testing region is still inside what is typically regarded as entrance length in the literature, as discussed in Sec. 2.4.4. The testing location is at a distance of approx. $6 \cdot D_h$ from the start of the rough analogue surfaces, however, $10 \cdot D_h$ is the typically accepted entrance length. Nonetheless, due to time restrictions and the limited effect we consider this will have on the final conclusions, it was decided to continue forwards with the testing campaign, accepting that the results will not be as good as expected and that this is a topic that should be tackled in the future.
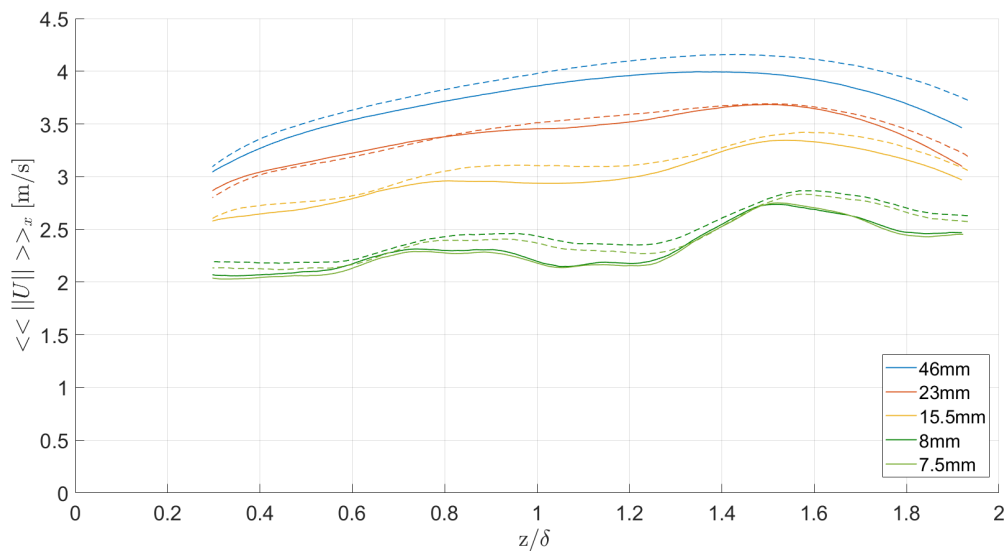

Figure D.2: Evolution of the velocity profile with distance from the rough analogue surface & downstream at a Re $\approx 2.00 \times 10^4$. Dashed lines are $1.5 \cdot D_h$ upstream.